

EDITORIAL

Neuroradiology in search of lost time:
the real world between the lived and the redefined (p.67-68)

IN-DEPTH REVIEW

Artificial intelligence in oncologic imaging: enhancing diagnostic precision towards
facilitating clinical decision-making (p.69-83)

FULL RESEARCH ARTICLES

Diagnostic performance of lung POCUS in neonatal respiratory disorders in
the neonatal intensive care unit: a new shortened protocol (p.84-93)

Prevalence of dolichoarteriopathies of the extracranial internal
carotid artery by neck CTA in Mexican patients (p.94-101)

Comparison of mammography breast density assessment
by radiologists and Quantra artificial intelligence in women with and without breast
implants: intra and interobserver agreement (p.102-111)

Duplex US acquisition and analysis protocol for portal hypertension:
a technical note (p.112-124)

BRIEF RESEARCH ARTICLE

Normal T2 relaxometry values of peripheral nerves on 3.0T MRI
in healthy Mexican subjects: an exploratory study (p.125-130)

CASE REPORT

Multimodality imaging with US, CT and MRCP for diagnosing
atypical Lemmel syndrome: a case report (p.131-136)

IMAGES IN RADIOLOGY

CTA and MRA findings of a persistent hypoglossal artery (p.137-138)



PERMANER
www.permayer.com

Official Journal of the



FEDERACIÓN MEXICANA DE RADIOLOGÍA E IMAGEN, A.C



Journal of the Mexican Federation of Radiology and Imaging

J Mex Fed Radiol Imaging

Volume 4. Number 2, April-June 2025

ISSN: 2938-1215

eISSN: 2696-8444

The *Journal of the Mexican Federation of Radiology and Imaging* (JMEXFRI) is the official journal of the Federación Mexicana de Radiología e Imagen. The aim of the journal is to disseminate scientific knowledge and technological developments for innovation in diagnostic and therapeutic radiology with original articles on basic and clinical aspects of modern radiology in an international context with global impact. JMEXFRI is published in American English with 4 issues per year (print and online) and the first issue was published in the first quarter of 2022. Articles undergo a rigorous, double-blind peer-review process. Publication of articles in JMEXFRI is free of charge and all published articles are open access.

The journal publishes the following types of manuscripts: *Full Research Article, Pictorial Essay, Brief Research Article, Technical Note, In-Depth Review, Case Report, Images in Radiology, and Editorial.*

EDITORIAL BOARD

EDITOR-IN-CHIEF

Mauricio Figueroa-Sanchez, M.D.

Department of Radiology, Antiguo Hospital Civil de Guadalajara "Fray Antonio Alcalde", Guadalajara, Jal., Mexico

ASSOCIATE EDITORS

Gerardo E. Ornelas-Cortinas, M.D.

*Centro Universitario de Imagen Diagnostica, Hospital Universitario
"Dr. Jose E. Gonzalez", Monterrey, N.L., Mexico*

Araceli Cue-Castro, M.D.

*Department of Computed Tomography, Hospital General
"Dr. Enrique Cabrera" SEDESA, Mexico City, Mexico*

Oscar A. Chavez-Barba, M.D.

*Department of Radiology,
Antiguo Hospital Civil de Guadalajara "Fray Antonio Alcalde",
Guadalajara, Jal., Mexico*

Ana M. Contreras-Navarro, M.D., M.Sc., Ph.D.

*Scientific Writing Workshop, JMEXFRI,
Zapopan, Jal., Mexico*

David Garza-Cruz, M.D.

*Department of Radiology, Hospital Angeles,
Torreon, Coah., Mexico*

J. Mario Bernal-Ramirez, M.D.

*Department of Medical Clinics, Centro Universitario de
Ciencias de la Salud, Universidad de Guadalajara,
Guadalajara, Jal., Mexico*

SCIENTIFIC TRANSLATOR EDITOR

Sergio Lozano-Rodriguez, M.D.

Research Office of the Vice Dean, Hospital Universitario "Dr. Jose E. Gonzalez", Monterrey, N.L., Mexico

BIostatistics ADVISER

Cesar N. Cristancho-Rojas, M.D., M.Sc.

School of Public Health, Oregon Health & Science University, Portland, OR., USA

DESIGN ADVISER

Jorge Mendez-Palacios, B.Sc.

Design Area, JMEXFRI. Zapopan, Jal., Mexico

NATIONAL EDITORIAL BOARD

HEAD AND NECK RADIOLOGY

Mario A. Campos-Coy, M.D.

Centro Universitario de Imagen Diagnostica,
Hospital Universitario "Dr. Jose E. Gonzalez",
Monterrey, N.L., Mexico

Eduardo D. Sarda-Inman, M.D.

Diagnostico Especializado por Imagen,
Zapopan, Jal., Mexico

GASTROINTESTINAL RADIOLOGY

Araceli Cue-Castro, M.D.

Department of Computed Tomography,
Hospital General "Dr. Enrique Cabrera" SEDESA,
Mexico City, Mexico

Adrian Negreros-Osuna, M.D., Ph.D.

Departamento de Radiología,
Hospital Regional ISSSTE Monterrey,
Monterrey, N.L., Mexico

Oscar A. Chavez-Barba, M.D.

Department of Radiology,
Antiguo Hospital Civil de Guadalajara
"Fray Antonio Alcalde",
Guadalajara, Jal., Mexico

OBSTETRIC AND GYNECOLOGICAL RADIOLOGY

Dante R. Casale-Menier, M.D.

Department of Radiology and Imaging,
Hospital Angeles,
Ciudad Juarez, Chih., Mexico

Roberto J. Carrales-Cuellar, M.D.

Department of Ecographic Diagnosis,
Radiología Especializada,
Guadalajara, Jal., Mexico

BREAST RADIOLOGY

David F. Perez-Montemayor, M.D.

General Direction,
Centro de Imagenología Integral IMAX,
Tampico, Tamps., Mexico

Beatriz Gonzalez-Ulloa, M.D.

Department of Breast Imaging,
Diagnostico Especializado por Imagen,
Guadalajara, Jal., Mexico

Margarita L. Garza-Montemayor, M.D.

Departamento de Imagen Diagnostica,
Centro de Cancer de Mama,
Hospital Zambrano Hellion, Tec Salud,
Monterrey, N.L., Mexico

Karla M. Nuñez-Barragan, M.D.

Women's Imaging Department,
Doctors Hospital East Auna
Monterrey, N. L., Mexico

Yazmin A. Ramirez-Galvan, M.D., Ph.D.

Breast Imaging Section
Department of Radiology and Imaging,
University Hospital "Dr. Jose Eleuterio Gonzalez"
Monterrey, N.L. Mexico

NUCLEAR AND MOLECULAR MEDICINE

Hugo E. Solis-Lara, M.D.

Centro de Imagen Molecular,
Hospital Christus Muguerza Alta Especialidad,
Monterrey, N.L., Mexico

NEURORADIOLOGY

Jorge Paz-Gutierrez, M.D.

Department of Magnetic Resonance,
Centro Medico Puerta de Hierro,
Zapopan, Jal., Mexico

Azalea Garza-Baez, M.D.

Department of Radiology and Imaging,
Hospital Zambrano Hellion,
Tecnologico de Monterrey,
Monterrey, N.L., Mexico

Perla M. Salgado-Lujambio, M.D.

Direccion de Enseñanza,
Instituto Nacional de Neurología y
Neurocirugía "Manuel Velasco Suarez"
Mexico City, Mexico

Rebeca de J. Ramos-Sanchez, M.D.

Department of Neuroimaging, Instituto Nacional
de Neurología y Neurocirugía "Manuel Velasco Suarez"
Mexico City, Mexico

PEDIATRIC RADIOLOGY

Aida Perez-Lara, M.D.

Department of Radiology, Hospital Español,
Mexico City, Mexico

MUSCULOSKELETAL RADIOLOGY

Oscar A. Chavez-Barba, M.D.

Department of Radiology, Antiguo Hospital Civil
de Guadalajara "Fray Antonio Alcalde",
Guadalajara, Jal., Mexico

J. Francisco Diaz-Fernandez, M.D.

Department of Radiology,
Hospital General "Agustin O'Horan",
Merida, Yuc., Mexico

CHEST AND CARDIOVASCULAR RADIOLOGY

Sergio A. Criales-Vera, M.D.

Department of Radiology and Imaging,
Instituto Nacional de Cardiología "Ignacio Chavez",
Mexico City, Mexico

Harold Goerne, M.D.

Department of Radiology, Hospital de Pediatría,
Instituto Mexicano del Seguro Social,
Guadalajara, Jal., Mexico

Luis F. Alva-Lopez, M.D.

Department of Radiology, Hospital Medica Sur,
Mexico City, Mexico

GENITOURINARY RADIOLOGY

Sergio B. Peregrina-Gonzalez, M.D.

Consultorio de Imagen,
Guadalajara, Jal., Mexico

Araceli Cue-Castro, M.D.

Department of Computed Tomography,
Hospital General "Dr. Enrique Cabrera" SEDESA,
Mexico City, Mexico

Adrian Negreros-Osuna, M.D.

Departamento de Radiología,
Hospital Regional ISSSTE Monterrey,
Monterrey, N.L., Mexico

Benjamin Conde-Castro, M.D.

Faculty of Medicine,
Universidad Nacional Autónoma de Mexico,
Mexico City, Mexico

ULTRASOUND

Rosa M. Alanis-Salazar, M.D.

Departamento de Radiología, UMF Guadalupe, ISSSTE,
Monterrey, NL., Mexico

Victor M. Rodriguez-Peralta, M.D.

Department of Radiology,
Fundacion de Cancer de Mama (FUCAM),
Oaxaca, Oax., Mexico

David Garza-Cruz, M.D.

Department of Radiology, Hospital Angeles,
Torreon, Coah., Mexico

Manuel Hernandez-Cruz, M.D.

Area de Ultrasonido,
Unidad de Ultrasonido Diagnostico,
Puebla, Pue. Mexico

VASCULAR AND INTERVENTIONAL RADIOLOGY

Guillermo Elizondo-Riojas, M.D., Ph.D.

Centro Universitario de Imagen Diagnostica,
Hospital Universitario "Dr. Jose E. Gonzalez",
Monterrey, N.L., Mexico

Raul A. De Luna-Vega, M.D.

Centro Universitario de Imagen Diagnostica,
Hospital Universitario "Dr. Jose E. Gonzalez",
Monterrey, N.L., Mexico

ARTIFICIAL INTELLIGENCE

Guillermo Elizondo-Riojas, M.D., Ph.D.

Centro Universitario de Imagen Diagnostica,
Hospital Universitario "Dr. Jose E. Gonzalez",
Monterrey, N.L., Mexico

Adrian Negreros-Osuna, M.D.

Departamento de Radiología,
Hospital Regional ISSSTE Monterrey,
Monterrey, N.L., Mexico

J. Mario Bernal-Ramirez, M.D.

Department of Medical Clinics,
Centro Universitario de Ciencias de la Salud,
Universidad de Guadalajara,
Guadalajara, Jal., Mexico

Benjamin Conde-Castro, M.D.

Faculty of Medicine,
Universidad Nacional Autónoma de México,
Mexico City, Mexico

JUNIOR EDITORIAL BOARD

J. Mario Bernal-Ramirez, M.D.

Department of Medical Clinics,
Centro Universitario de Ciencias de la Salud,
Universidad de Guadalajara,
Guadalajara, Jal., Mexico

Ana K. Luna-Marroquin, M.D.

Centro Universitario de Imagen Diagnostica,
Hospital Universitario "Dr. Jose E. Gonzalez",
Monterrey, N.L., Mexico

M. Lourdes Garcia-Colmenero, M.D.

Departamento de Radiología,
CID Centro de Imagen y Diagnostico
Guadalajara, Jal., Mexico

Xavier A. Gonzalez-Ballesteros, M.D.

Departamento de Radiología,
Hospital San Angel Inn Universidad,
Ciudad de Mexico, Mexico

Adriana Parada-Gallardo, M.D.

Department of Radiology,
Hospital General de Zapopan,
Zapopan, Jal., Mexico

A. Sofia Sanchez-Gomez, M.D.

Department of Radiology,
Grupo RIO Centro Integral de Diagnostico Medico
Guadalajara, Jal., Mexico

INTERNATIONAL EDITORIAL BOARD

HEAD AND NECK RADIOLOGY

Richard H. Wiggins, M.D.

Department of Radiology and Imaging Sciences,
School of Medicine, University of Utah,
Salt Lake City, UT., USA

Amy Juliano, M.D.

Department of Radiology,
Massachusetts Eye and Ear,
Harvard Medical School,
Boston, MA., USA

GASTROINTESTINAL RADIOLOGY

Luis Martí-Bonmatí, M.D., Ph.D.

Grupo de Investigación Biomédica en Imagen (GIBI230)
Instituto de Investigación
Sanitaria La Fe Área Clínica de Imagen Médica,
Hospital Universitario y Politécnico La Fe,
Valencia, Spain

Jorge A. Soto, M.D.

Department of Radiology, Boston Medical Center,
Boston, MA., USA

Jorge Elias Jr. Ph.D.

Departamento de Imagenes Medicas,
Oncologia e Hematologia,
Faculdade de Medicina Ribeirao Preto,
Universidade Sao Paulo Ribeirao Preto,
Sao Paulo, Brazil

Valdair F. Muglia, M.D.

Faculdade de Medicina de Ribeirão Preto,
Universidade de São Paulo, Ribeirão Preto,
Sao Paulo, Brazil

Carlo Catalano, M.D.

Department of Diagnostic Radiology
La Sapienza University of Rome
Rome, Italy

OBSTETRIC AND GYNECOLOGIC RADIOLOGY

Luciana Pardini Chamie, M.D., Ph.D.

Centro de Diagnostico Ultrasonografico
Especializado en Imagen de la Mujer,
Sao Paulo, Brazil

BREAST RADIOLOGY

Javier Romero-Enciso, M.D.

Department of Radiology,
Fundacion Santa Fe,
Bogota, Colombia

NUCLEAR AND MOLECULAR MEDICINE

Begoña Martinez-Sanchis, M.D.

Department of Nuclear Medicine,
Hospital Universitario y Politecnico La Fe,
Valencia, Spain

Cesar N. Cristancho-Rojas, M.D., M.Sc.

School of Public Health,
Oregon Health & Science University,
Portland, OR., USA

NEURORADIOLOGY

Roy F. Riascos-Castaneda, M.D.

Department of Radiology and Neurosurgery,
Memorial Hermann Hospital System,
Houston, TX., USA

Rafael Rojas-Jasso, M.D.

Department of Radiology, Beth Israel,
Deaconess Medical Center,
Boston, MA., USA

Henrique Carrete Jr., M.D., Ph.D.

Department of Diagnostic Imaging,
Universidade de Sao Paulo,
Sao Paulo, Brazil

Carlos Torres, M.D.

Department of Diagnostic Imaging,
The Ottawa Hospital,
Ottawa, Canada

MUSCULOSKELETAL RADIOLOGY

Javier Fernandez-Jara, M.D.

Department of Radiology,
Hospital Universitario Sanitas La Zarzuela,
Madrid, Spain

Jose Luis del Cura, M.D.

Radiodiagnosis Service,
Hospital Universitario Donostia,
San Sebastian-Donostia, Spain

Diego F. Lemos, M.D.

Department of Radiology,
University of Vermont Medical Center,
Burlington, VT, USA

PEDIATRIC RADIOLOGY

George Bisset, M.D.

Department of Radiology, Children's Hospital
Pennsylvania, PA., USA

Sara Reis Teixeira, M.D., Ph.D.

Department of Radiology, Children's Hospital
Pennsylvania, PA. USA

CHEST AND CARDIOVASCULAR RADIOLOGY

Fernando R. Gutierrez, M.D.

Department of Radiology and Cardiothoracic Imaging,
The Mallikrodt Institute of Radiology,
St. Louis, MO., USA

Jorge Carrillo-Bayona, M.D.

Department of Radiology,
Hospital Universitario Mayor,
Bogota, Colombia

Carlos S. Restrepo, M.D.

Department of Cardiothoracic Radiology,
Texas University,
San Antonio, TX., USA

Sebastian Rossini, M.D.

Department of Radiology,
Instituto Radiologico Mater Dei,
Buenos Aires, Argentina

Santiago Martinez-Jimenez, M.D.

Department of Radiology,
Saint Luke's Hospital of Kansas City,
Kansas City, KS., USA

L. Antonio Sosa-Lozano, M.D.

Department of Cardiothoracic Radiology,
Medical College of Wisconsin,
Milwaukee, WI., USA

GENITOURINARY RADIOLOGY

Daniela Stoisa, M.D.

Department of Radiology, Diagnostico Medico Oroño,
Rosario, Santa Fe, Argentina

Valdair F. Muglia, M.D.

Faculdade de Medicina de Ribeirao Preto,
Universidade de Sao Paulo Ribeirao Preto,
Sao Paulo, Brazil

ULTRASOUND

Edward G. Grant, M.D.

Department of Radiology, USC Norris Cancer Center,
Los Angeles, CA., USA

Juan P. Niedmann-Espinosa, M.D.

Department of Ecotomography,
Clinica Alemana de Santiago,
Santiago de Chile, Chile

VASCULAR AND INTERVENTIONAL RADIOLOGY

Manuel Cifrian-Perez, M.D., Ph.D.

Imaging Clinic Department,
Hospital Universitario y Politecnico La Fe,
Valencia, Spain

ARTIFICIAL INTELLIGENCE

Luis Martí-Bonmati, M.D., Ph.D.

Grupo de Investigación Biomédica en Imagen (GIBI230)
Instituto de Investigación Sanitaria La Fe
Área Clínica de Imagen Médica,
Hospital Universitario y Politécnico La Fe
Valencia, Spain

Leonor Cerda-Alberich, Ph.D.

Imaging Clinic Department,
Hospital Universitario y Politecnico La Fe,
Valencia, Spain

Felipe Campos Kitamura, M.D., Ph.D.

Dasalnova, Dasa,
Sao Paulo, Brazil

WEBSITE ADMINISTRATION COMMITTEE

David Garza-Cruz, M.D.

Coordinator, Department of Radiology, Hospital Angeles,
Torreon, Coah., Mexico

Ana Karen Luna-Marroquin, M.D.

Head and Neck Radiology Section
Centro Universitario de Imagen Diagnostica,
Hospital Universitario "Dr. Jose E. Gonzalez",
Monterrey, N.L., Mexico

Hugo E. Solis-Lara, M.D.

Gastrointestinal Radiology Section and Nuclear
And Molecular Medicine Section
Centro de Imagen Molecular,
Hospital Christus Muguerza Alta Especialidad,
Monterrey, N.L., Mexico

Dante R. Casale-Menier, M.D.

Gynecology and Obstetrics Radiology Section
Genitourinary Radiology Section
Department of Radiology and Imaging,
Hospital Angeles,
Ciudad Juarez, Chih., Mexico

Beatriz Gonzalez-Ulloa, M.D.

Breast Radiology Section
Department of Breast Imaging,
Diagnostico Especializado por Imagen,
Guadalajara, Jal., Mexico

Yazmin A. Ramirez-Galvan, M.D., Ph.D.

Breast Radiology Section
Breast Imaging Section
Department of Radiology and Imaging,
University Hospital "Dr. Jose Eleuterio Gonzalez"
Monterrey, N.L. Mexico

Rebeca de J. Ramos-Sanchez, M.D.

Neuroradiology Section
Department of Neuroimaging, Instituto Nacional
de Neurologia y Neurocirugia
"Manuel Velasco Suarez"
Mexico City, Mexico

Aida Perez-Lara, M.D.

Pediatric Radiology Section
Department of Radiology,
Hospital Español, Mexico City, Mexico

Gerardo E. Ornelas-Cortinas, M.D.

Musculoskeletal Radiology Section
Centro Universitario de Imagen Diagnostica,
Hospital Universitario "Dr. Jose E. Gonzalez",
Monterrey, N.L., Mexico

Cesar N. Cristancho-Rojas, M.D., M.Sc.

Chest and Cardiovascular Radiology Section
School of Public Health,
Oregon Health & Science University,
Portland, OR., USA

J.M. Ignacio Lopez-Mendez, M.D.

Ultrasound Section
Department of Radiology and Imaging,
Hospital de Especialidades, CMNO
Instituto Mexicano del Seguro Social,
Guadalajara, Jal., Mexico.

Mauricio Figueroa-Sanchez, M.D.

Vascular and Interventional Radiology Section
Department of Radiology,
Antiguo Hospital Civil de Guadalajara
"Fray Antonio Alcalde",
Guadalajara, Jal., Mexico

J. Mario Bernal-Ramirez, M.D.

Artificial Intelligence Radiology Section
Department of Medical Clinics,
Centro Universitario de Ciencias de la Salud,
Universidad de Guadalajara,
Guadalajara, Jal., Mexico

Diana Camorlinga-Ornelas, M.D.

General Radiology Section, Imaging Department
Hospital General Regional Num. 2
Mexican Social Security Institute
Ciudad Juarez, Chih., Mexico.

GRAPHICAL ABSTRACTS COMMITTEE

Oscar A. Chavez-Barba, M.D.

Department of Radiology,
Antiguo Hospital Civil de Guadalajara
"Fray Antonio Alcalde",
Guadalajara, Jal., Mexico

Adriana Parada-Gallardo, M.D.

*Department of Radiology,
Hospital General de Zapopan,
Zapopan, Jal., Mexico*

J.M. Ignacio Lopez-Mendez, M.D.

*Department of Radiology and Imaging,
Hospital de Especialidades, CMNO
Instituto Mexicano del Seguro Social,
Guadalajara, Jal., Mexico.*

Juan Pablo Lopez-Gutierrez, M.D.

*Department of Radiology and Imaging,
Hospital General de Zona 3,
Instituto Mexicano del Seguro Social
Aguascalientes, Ags., Mexico*

Gerardo Llamas-Linares, M.D.

*Centro Universitario de Imagen Diagnostica,
Hospital Universitario "Dr. Jose E. Gonzalez",
Monterrey, N.L., Mexico*

Alejandra I. Castillo-Cervantes, M.D.

*Centro Universitario de Imagen Diagnostica,
Hospital Universitario "Dr. Jose E. Gonzalez",
Monterrey, N.L., Mexico*

A. Sofia Sanchez-Gomez, M.D.

*Department of Radiology,
Grupo RIO Centro Integral de Diagnostico Medico,
Guadalajara, Jal., Mexico*

SOCIAL MEDIA COMMITTEE

Guillermo Elizondo-Riojas, M.D., Ph.D.

*Centro Universitario de Imagen Diagnostica,
Hospital Universitario "Dr. Jose E. Gonzalez",
Monterrey, N.L., Mexico*

Oscar A. Chavez-Barba, M.D.

*Department of Radiology,
Antiguo Hospital Civil de Guadalajara
"Fray Antonio Alcalde",
Guadalajara, Jal., Mexico*

J. Mario Bernal-Ramirez, M.D.

*Department of Medical Clinics,
Centro Universitario de Ciencias de la Salud,
Universidad de Guadalajara,
Guadalajara, Jal., Mexico*

Adriana Parada-Gallardo, M.D.

*Department of Radiology,
Hospital General de Zapopan,
Zapopan, Jal., Mexico*

A. Sofia Sanchez-Gomez, M.D.

*Department of Radiology,
Grupo RIO Centro Integral de Diagnostico Medico.
Guadalajara, Jal., Mexico*

RADIOLOGICAL AND CLINICAL CORRELATION BOARD

GASTROENTEROLOGY

Linda E. Muñoz-Espinosa, M.D., Ph.D.

*Liver Unit, Hospital Universitario
"Dr. Jose E. Gonzalez",
Monterrey, N.L., Mexico*

David Marti-Aguado, M.D., Ph.D.

*Servicio Medicina Digestiva,
Hospital Clínico Universitario,
Valencia, Spain*

GASTROINTESTINAL AND GENERAL SURGERY

Carlos Nuño-Guzman, M.D., M.Sc.

*Department of Surgery,
Antiguo Hospital Civil de Guadalajara
"Fray Antonio Alcalde",
Guadalajara, Jal., Mexico*

OBSTETRICS AND GINECOLOGY

Sergio Fajardo-Dueñas, M.D., M.Sc.

*Division of Obstetrics and Gynecology,
Nuevo Hospital Civil de Guadalajara,
Guadalajara, Jal., Mexico*

NEUROLOGY

Jose L. Ruiz-Sandoval, M.D., M.Sc.

*Department of Neurology, Antiguo Hospital Civil
de Guadalajara "Fray Antonio Alcalde",
Guadalajara, Jal., Mexico*

RHEUMATOLOGY

Monica Vazquez del Mercado-Espinosa,
M.D., Ph.D.

*Division of Medicine,
Nuevo Hospital Civil de Guadalajara,
Guadalajara, Jal., Mexico.*

CARDIOLOGY-PNEUMOLOGY

Jose M. Hernandez, M.D.

*Department of Ecocardiography,
Doctors Hospital,
Monterrey, N.L., Mexico*

PATHOLOGICAL ANATOMY

Marco A. Ponce-Camacho, M.D., Ph.D.

*Department of Cytopathology, Doctors Hospital,
Monterrey, N.L., Mexico*

ENDOCRINOLOGY

Jesus Zacarias Villarreal-Perez, M.D.

*Department of Endocrinology,
Hospital Universitario "Dr. Jose E. Gonzalez",
Monterrey, N.L., Mexico*

HEMATOLOGY

Carlos R. Best-Aguilera, M.D.

*Department of Hematology,
Hospital General de Occidente. Secretaria de Salud
Zapopan, Jal., Mexico*

GYNECOLOGICAL UROLOGY

Patricia I. Velazquez-Castellanos, M.D., M.Sc.

*Department of Gynecology and Obstetrics,
Antiguo Hospital Civil de Guadalajara
"Fray Antonio Alcalde",
Guadalajara, Jal., Mexico*

PEDIATRIC NEUROLOGY

Daniel Perez-Rulfo Ibarra, M.D., Ph.D.

*Departamento de Pediatria,
Antiguo Hospital Civil de Guadalajara
"Fray Antonio Alcalde",
Guadalajara, Jal., Mexico*

Follow us



<https://linkedin.com/company/jmexfri>



<https://instagram.com/jmexfri>



<https://facebook.com/jmexfri>



<https://youtube.com/@jmexfri>



<https://x.com/jmexfri>



Original papers should be deposited in their electronic version through the following URL:

<https://publisher.jmexfri.permanyer.com>



PERMANYER
www.permanyer.com

Permanyer Mexico

Temistocles, 315
Col. Polanco, Del. Miguel Hidalgo
11560 Ciudad de Mexico
mexico@permnyer.com

Permanyer

Mallorca, 310 – Barcelona (Cataluña), España
permnyer@permnyer.com

ISSN: 2696-8444

Ref.: 10990AMEX252



www.permanyer.com

Reproductions for commercial purposes:

Without the prior written consent of the publisher, no part of this publication may be reproduced, stored in a retrievable medium or transmitted, in any form or by any means, electronic, mechanical, photocopying, recording or otherwise, for commercial purposes.

Journal of the Mexican Federation of Radiology and Imaging is an open access publication with the Creative Commons license CC BY-NC-ND (<http://creativecommons.org/licenses/by-nc-nd/4.0/>).

The opinions, findings, and conclusions are those of the authors. The editors and publisher are not responsible and shall not be liable for the contents published in the journal.

© 2025 Federacion Mexicana de Radiologia e Imagen, AC. Published by Permanyer.

Neuroradiology in search of lost time: the real world between the lived and the redefined

Antonio Rocha 

School of Medical Sciences, Santa Casa de Sao Paulo, Sao Paulo, Brazil

It is not uncommon for those who have been working for more than two decades in any field to feel old, sometimes nostalgic, and criticizing young people and their new ways. It is not uncommon for us to condemn that “medicine with this generation that is here has no future”. However, let us not forget that this also happened to us when we were young and that there were other old people who also condemned us. Certainly, before them, others have gone through in a similar scenario, possibly, it has always been like this...

In an individual analysis, the time we lost in our professional lives is the time we felt like heroes of our own existence and focused on accumulating knowledge so that we are better today than we once were. However, as we mature, we look at the movie of our professional life, which was always shot in black and white and with outdated, obsolete technology. Then we realize that much has changed, that the pace has changed, that the generations have run their course and that today, bound by strong bonds of memory and self-knowledge, we must set out in search of a new (rediscovered) time.

By extending our gaze to the horizon of any medical specialty, we can transcend the same permanent search for a new time. Neuroradiology and neuroradiologists, in particular, deserve careful reflection, with a view to defining nuances that appreciate their limits and scope. We have been taught that “clinical practice is sovereign”. I don't know who said that, but it certainly wasn't a 21st century neuroradiologist.

Who among us hasn't heard a clinician, more concerned with to semiological rigor, say that our hypotheses, sometimes based on an elaborate imaging study, don't fit that specific scenario? How many of us, interlocutors rooted in the rigor of a detailed interpretation of our studies, have not yet responded that the imaging diagnosis may precede the classic clinical presentation of a florid syndrome? In this regard, the “clinical and imaging times” cannot be seen as antagonistic nor as immiscible compounds. The origin of clinical knowledge cannot be ignored, but it is essential to understand and decipher it in the light of current science. Let us always remember that classical neurological syndromes began to flourish as a way of consolidating knowledge and passing it on, around 150 years ago. The old is not necessarily obsolete, but the way of seeing it can no longer be done with the same eyes as before.

Over the years, we have seen major revolutions in neurological diagnosis, first with computed tomography (CT), which has replaced pneumoencephalography, and then with magnetic resonance imaging (MRI). We have already seen how MRI has demystified topographic, syndromal and even etiologic diagnosis in medical practice. Now we are witnessing how the highest magnetic fields of our machines, currently over 10.0 Tesla, promise to unlock unexplored frontiers of microneuroanatomy, physiology and even pathophysiology. Over the past decade, we have witnessed the invasion of imaging into the molecular, biochemical and functional environment of the

Corresponding author:

Antonio Rocha
E-mail: antonio-rocha@spr.org.br

Received for publication: 24-02-2025

Accepted for publication: 28-02-2025

DOI: 10.24875/JMEXFRI.M25000100

Available online: 15-07-2025

J Mex Fed Radiol Imaging. 2025;4(2):67-68

www.JMeXFRI.com

2696-8444 / © 2025 Federación Mexicana de Radiología e Imagen, A.C. Published by Permanyer. This is an open access article under the CC BY-NC-ND (<https://creativecommons.org/licenses/by-nc-nd/4.0/>).

central nervous system and we eagerly await the unveiling of other intricacies, the development of specific tissue markers and other microstructural incursions into nervous tissue.

Today, neuroradiology is one of the medical specialties whose full practice entails the greatest complexity. Not “only” because of the inherent difficulty of diagnosing each individual case, but certainly also because of the continuous technological development of our instruments and, in a broader scope, of neuroscience as a whole. Diagnoses have gained in molecular details implicated in the composition of genes. They address genetic interactions with the environment and unveil complex immunological mechanisms, revealing biological markers that rename diseases.

We are seeing genetics and molecular studies give code names to old neurological syndromes. Almost twenty years ago, I could see that these classical names had their place in a more noble past of medical semiology, when most neurological syndromes and signs were described in the late 19th or early 20th century. At that time, the neurological practice of attending patients, gradually recording the clinical evolution of each case step by step and describing a series of signs and symptoms, allowed astute observers to describe in detail each nuance of the diseases, seeing in this the opportunity to perpetuate their names. This is the plot of most syndromes that are now part of a lost time.

Today, genetics, immunology, biochemistry and infectious disease, particularly of viruses and even prions, replace those terrifying foreign names that composed complex syndromes and their subtypes or variants. In this way, our rediscovered time defines biomarkers, risk markers and typifies chromosomes and their loci. It is to these distant lands that our terrifying memories will migrate, where anonymous scientists will develop means for ever earlier and more precise diagnosis and redefine diseases with cold labels of numbers and letters. Who remembers the ill-fated name “Hallervorden-Spatz syndrome”, now renamed pantothenate kinase-associated neurodegeneration, or simply PKAN? It could be the well-known Devic’s disease, now redefined and called neuromyelitis optical spectrum disorder (NMOSD).

Scientific information is imperative for the evolution and practice of any medical activity. However, what we sometimes see with astonishment, is a whirlwind of scientific productions, copies, reproductions, original articles, compendia, sophisms and ephemeral truths or those influenced by an increasingly profit-hungry industry. The conscious exercise of the specialty, however, entails the

responsibility that we have to interpret, in the midst of this whirlwind, what applies to the environment in which we work. It is not wise to reproduce the excesses of a purely commercial medical practice, but at the same time it is unworthy to judge the technology required for the best diagnosis as expensive.

I have long envisioned neuroradiology because I know that in the reality of our profession there will always be room for the principles that have guided us up to now: methodical observation and critical interpretation of results aimed at producing creative discussions and consistent results. No matter how nostalgic or non-conformist we may be, the present and the future will always meet again and always in eternal return, so that our practice, no matter how notorious it is (or was), will become obsolete.

Although ephemeral or even fleeting, technologies and their glimpses cannot be separated from human medical practice, nor can they dispense with universal ethical precepts. Fortunately, as doctors, we will continue the tireless search for a rediscovered time, but without, being able to give up our precious lived time, which was never lost, it was just an indispensable stage for us to be here today, as we are, with everything we have accumulated on our journey of discoveries and redefinitions.

In conclusion, the most reasonable view is that the diseases are the same and most of them have existed since time immemorial. It is the contours of their bases and their etiopathogenesis that are being redefined, with the grace of rediscovered times to change their names, aiming to adapt the new to the most modern. It is a fact that we have already entered a new frontier that promises to be as permanent or definitive as there are eternal and ephemeral truths of science. We are living in the days of technological evolution, the same that creates machines that become obsolete in a short time. This is how science works, particularly neuroradiology, which combines art and knowledge by offering us the opportunity to make a diagnosis based on detailed training supported by accumulated scientific information that does not make up for lost time, integrating with new equipment and modern techniques with a view to unattainable precision.

Funding

Not applicable.

Conflicts of interest

The author discloses no potential conflicts of interest.

Artificial intelligence in oncologic imaging: enhancing diagnostic precision towards facilitating clinical decision-making

Mariusz J. Kujawa^{1*}, Leonor Cerda-Alberich², and Luis Marti-Bonmati^{2,3}

¹Second Department of Radiology, Medical University of Gdansk, Poland; ²Grupo de Investigacion Biomedica en Imagen (GIBI230), Instituto de Investigacion Sanitaria La Fe, Valencia, Spain; ³Area Clinica de Imagen Medica, Hospital Universitario y Politecnico La Fe, Valencia, Spain

ABSTRACT

The integration of artificial intelligence (AI) into medical imaging is transforming cancer diagnosis, prognosis, and treatment planning. AI-based tools have shown high accuracy in analyzing images to detect and classify tumors and assess treatment response. Further developments combine image data with other metrics and biomarkers, including clinical, molecular and genetic data, enabling the development of more effective AI-based clinical decision support systems, that allow oncologists to select optimal personalized management and therapy for each patient in real time. Despite these advances, there are still some challenges that hinder the implementation of new AI solutions. Key barriers include the problem of availability of large, open and harmonized medical datasets, the lack of reproducibility between AI studies in different real-world scenarios, and ethical and regulatory issues. Addressing these challenges requires interdisciplinary collaboration between clinicians, data scientists and regulators. Initiatives such as FUTURE-AI and data sharing projects such as the European Federation for Cancer Images (EUCAIM) are important steps towards developing trustworthy and effective AI systems. New advances in this field will undoubtedly improve personalization approaches and ultimately patient outcomes.

Keywords: Diagnostic imaging. Artificial intelligence. Oncology.

INTRODUCTION

Cancer continues to pose a significant global health burden, accounting for substantial rates of morbidity and mortality across diverse populations. This requires continuous progress in early detection, precise diagnosis and personalized treatment strategies¹. Among the most important tools in oncologic care, medical imaging plays a pivotal role as it provides essential information for tumor characterization, disease staging, treatment response monitoring, and long-term surveillance. However,

the increasing complexity of oncologic imaging, and the demand for more accurate and reproducible assessments have underscored the need for computational approaches to improve diagnostic accuracy and daily clinical workflows.

Artificial intelligence (AI) has emerged as a transformative force in oncologic imaging, leveraging machine learning and deep learning techniques to improve image analysis, automate labor-intensive tasks and facilitate data-driven decisions². Radiology is at the forefront of AI adoption due to its reliance on large-scale digital

*Corresponding author:

Mariusz J. Kujawa

E-mail: mariusz.kujawa@gumed.edu.pl

2696-8444 / © 2025 Federación Mexicana de Radiología e Imagen, A.C. Published by Permanyer. This is an open access article under the CC BY-NC-ND (<https://creativecommons.org/licenses/by-nc-nd/4.0/>).

Received for publication: 25-02-2025

Accepted for publication: 28-02-2025

DOI: 10.24875/JMEXFRI.M25000101

Available online: 15-07-2025

J Mex Fed Radiol Imaging. 2025;4(2):69-83

www.JMeXFRI.com

repositories of image data, which provide the foundation for training robust AI models^{3,4}. The increasing availability of high-throughput computational resources and advances in deep learning architectures, particularly convolutional neural networks (CNNs), have enabled AI systems to perform image reconstruction, lesion detection, tumor segmentation, and quantitative feature extraction with growing accuracy and efficiency^{5,6}.

AI applications in oncological imaging span multiple stages of the diagnosis and treatment pipeline. In image acquisition and post-processing, AI improves image quality, reduces radiation exposure, optimizes scan protocols and minimizes contrast doses, ultimately increasing patient safety³. AI-driven algorithms for lesion detection and segmentation have shown enhanced efficacy in comparison to traditional manual methods, which are time-consuming and prone to inter-observer variability^{6,7}. Furthermore, the application of AI in radiomics has facilitated the extraction of high-dimensional quantitative imaging features as biomarkers that capture tumor heterogeneity and correlate with clinically relevant endpoints such as tumor aggressiveness, response to treatment and prognosis^{8,9}. Clinical decision support systems (CDSS) using AI and integrating imaging data with genomic, molecular and clinical information are also being developed, enabling a more comprehensive and personalized approach to cancer care^{10,11}.

In addition to radiomics, habitat imaging is an emerging AI-powered approach that seeks to map different tumor subregions based on the spatial distribution of imaging biomarkers. By segmenting tumors into different biologically and physiologically distinct habitats, this technique provides deeper insights into the tumor microenvironment, aiding in patient stratification and optimizing therapeutic strategies^{5,12}. These advances align with the growing emphasis of precision oncology, where AI-driven insights can lead to treatment decisions tailored to individual tumor characteristics.

Despite its potential, the widespread clinical implementation of AI in oncologic imaging is hindered by several challenges. One of the most critical issues is the interpretability of AI models, often referred to as a “black box” problem, limiting transparency and clinician confidence^{11,13}. In addition, there are concerns regarding the generalizability of AI models, as algorithms trained on limited or homogeneous datasets may underperform when applied to varied patient populations. This highlights the need for large-scale validation studies in different settings and demographic groups¹⁴. Ethical and

legal considerations, including data privacy, accountability in AI-based decision-making and regulatory approval, also pose significant barriers to clinical application^{14,15}.

This review provides a comprehensive analysis of the evolving role of AI in oncologic imaging, focusing on key areas such as image data harmonization, biomarker extraction, predictive modeling, and CDSS. While AI has the potential to revolutionize cancer diagnosis and treatment, its successful integration into clinical practice requires overcoming technical, ethical and regulatory challenges. Overcoming these limitations through rigorous validation, explainable AI frameworks and interdisciplinary collaboration will be essential to ensure the long-term impact of AI on oncologic care and improve patient outcomes. For clarity and consistency, the key concepts relevant to AI in oncologic imaging are summarized in table 1.

PREPARATION OF IMAGING DATA FOR ANALYSIS

Imaging data repositories

The successful application of AI in oncologic imaging relies on access to large-scale, high-quality imaging datasets enriched with clinically relevant metadata. AI models require extensive training, testing and validation datasets to ensure robust performance across different patient populations and imaging conditions¹⁶. These datasets are often sourced from structured repositories, either through direct integration with hospital information systems and medical image viewers or as independent web-based platforms designed for AI research and development¹⁷.

Several large-scale imaging repositories exist to facilitate AI research in oncology. Notably, The Cancer Imaging Archive (TCIA) and the UK Biobank provide extensive collections of radiological images linked to clinical and genomic data^{18,19}. In Europe, the European Federation for Cancer Images (EUCAIM) project is leading efforts to create a federated platform for oncology imaging that integrates data from multiple institutions while enabling the seamless development of AI applications²⁰. These initiatives follow the FAIR (Findable, Accessible, Interoperable, Reusable) principles and ensure that imaging datasets are openly accessible and optimally structured for AI-driven oncology research²¹.

However, despite the increasing availability of imaging repositories, some challenges remain. Many of the existing datasets are not representative of the global

Table 1. Key AI terminology in oncologic imaging

Term	Definition
Algorithm	A set of mathematical rules used to process training data and develop AI models
Artificial intelligence (AI)	A branch of computer science that enables systems to perform tasks typically require human intelligence, such as reasoning, learning, pattern recognition and decision-making
AI model	A trained computer system that applies learned patterns to solve a specific problem in medical imaging, e.g. tumor detection or segmentation
Deep learning	A branch of machine learning that uses multilayer neural networks (e.g. CNNs) to extract and learn complex patterns from raw imaging data
Machine learning	A branch of AI that enables computers to learn patterns from data without explicit programming. In oncologic imaging, machine learning is used to classify tumors, detect lesions and create prognostic models
Foundation models	Large-scale deep learning models that can interpret and generate both text and image data. They have been trained with extensive unlabeled data and have shown high performance on various tasks
Habitat imaging	A technique that uses imaging features to identify different tumor microenvironments to support personalized treatment planning
Imaging biomarkers	Measurable features derived from medical images that indicate normal or pathological processes and responses to treatment
Radiomics	A method of extracting a large number of quantitative features from medical images to derive imaging biomarkers for diagnosis, prognosis, and treatment response assessment

AI: artificial intelligence; CNNs: convolutional neural networks.

population, often being biased toward specific demographics or imaging protocols²². Furthermore, interoperability between different image archives is limited as differences in data structures and metadata formats hinder seamless data integration²³. To address this, emerging platforms emphasize interoperability by standardizing metadata descriptions, harmonizing data formats, and integrating federated learning frameworks that allow AI training without requiring direct data exchange²⁴. In addition, the development of AI models on the platform is becoming more and more prevalent. Some repositories include embedded analytical engines for preliminary image interpretation and feature extraction, thereby reducing redundancy and accelerating the deployment of AI²⁵.

Harmonization of imaging data

A key challenge in AI-driven oncologic imaging is the heterogeneity of imaging datasets, as medical images vary significantly due to differences in acquisition protocols, scanner manufacturers and institutional practices²⁶. Retrospective imaging data often lack standardized acquisition settings, making direct comparisons between datasets difficult. While this variability presents

a challenge for AI training, it also provides an opportunity to develop generalized models that perform well in different clinical settings²⁷.

To address this variability, harmonization techniques have been developed to standardize image features while preserving clinically relevant information. Data harmonization can be categorized into four primary approaches:

- Distribution-based methods: these techniques adjust the intensity distributions between datasets to align them with a reference standard. Methods such as ComBat, Mutual Nearest Neighbors (MNN) and Domain Adaptation are commonly used to remove batch effects and improve the comparability of datasets^{28,29}.
- Image processing techniques: resampling, noise reduction, intensity normalization and histogram matching reduce scanner-induced variations, particularly in radiomics applications where pixel intensity variations can significantly affect model performance³⁰.
- Data synthesis approaches: generative models such as CycleGAN and Conditional Variational Autoencoders (VAE) have been used to create synthetic images that match the statistical properties of real-world datasets, aiding in data augmentation and domain adaptation³¹.

- Invariant feature learning: this approach focuses on extracting imaging features that are robust to variations in acquisition settings to ensure that AI models remain unaffected by inter-cohort variability³².

A notable example of harmonization efforts is the CHAIMELEON project, which is developing a repository of harmonized imaging data for four major cancer types: lung, prostate, breast, and colorectal. This initiative integrates harmonization techniques at both the image and metadata levels to ensure consistency of data and enable training of AI models across multiple institutions^{33,34}. However, an important question in harmonization is whether these changes alter clinically relevant image features. Evaluation of harmonization strategies requires systematic validation to ensure that AI models trained on harmonized data maintain their diagnostic and predictive performance in real-world applications³⁵.

Segmentation: the foundation for AI model development

Accurate tumor segmentation is one of the most critical steps in AI-driven oncology imaging, as it defines the specific voxels belonging to a tumor and directly impacts downstream tasks such as classification, radiomics feature extraction and response prediction. Manual segmentation, typically performed by radiologists, is time-consuming, prone to inter-observer variability, and difficult to scale across large datasets³⁶. Therefore, automated segmentation methods based on deep learning have become popular, significantly reducing the workload of radiologists while ensuring high accuracy and consistency³⁷.

Convolutional Neural Networks (CNNs) are the most widely used architectures for tumor segmentation, with the U-Net and its variants serving as the gold standard for different cancer types³⁸. Recent studies have demonstrated the effectiveness of deep learning-based segmentation models, which achieved Dice similarity coefficients of 0.93 for brain tumors and 0.99 for neuroblastoma, highlighting their robustness and reliability^{10,39}.

Advances in AI-driven segmentation increasingly incorporate multimodal imaging, e.g. magnetic resonance imaging (MRI), positron emission tomography (PET) and computed tomography (CT) fusion to improve segmentation accuracy and capture complementary information from different imaging modalities⁴⁰. Furthermore, attention mechanisms and transformer-based architectures are being explored to refine segmentation maps and improve boundary delineation in complex cases⁴¹.

Despite these advances, challenges remain in terms of the generalizability and robustness of models. AI segmentation models trained on small, homogeneous datasets may fail to generalize to unknown cases, particularly when imaging protocols are different⁴². Addressing this problem requires access to large, diverse and harmonized datasets, as well as federated learning strategies that enable cross-institutional model training while preserving patient privacy²⁴. The integration of AI-driven segmentation into clinical workflows must also be carefully considered to ensure that it enhances, rather than disrupts, standard radiology practices.

IMAGE-BIOMARKER EXTRACTION

Radiomics features

The increasing demand for precision oncology has driven the development of novel biomarkers that go beyond conventional radiologic assessment. Traditional imaging-based tumor classification systems rely on subjective interpretation and standardized scales that often fail to capture the full spectrum of tumor heterogeneity, microstructural changes, and aggressiveness. Radiomics is an advanced computational approach that extracts high-dimensional quantitative features from medical images and enables the identification of imaging biomarkers that correlate with clinically significant tumor characteristics^{36,43}. By analyzing large datasets and integrating radiomics features with clinical, genomic, and histopathological data, AI-driven radiomics models have shown promise in improving tumor characterization, treatment response prediction, and prognostic assessment^{44,45}.

Radiomics features can be categorized into different groups depending on the type of information they provide. First-order statistical features describe the distribution of voxel intensities within a defined region of interest (ROI) without considering spatial relationships. These include mean, median, standard deviation, skewness and kurtosis, which quantify the general intensity distribution of the lesion⁴⁶. Shape-based features characterize the geometric properties of the lesion, including volume, surface area, sphericity, compactness, and elongation, and provide information about the morphology of the tumor.

In addition to these basic descriptors, texture-based features evaluate the spatial organization and complexity of voxel intensities. These include models such as the Gray Level Co-occurrence Matrix (GLCM), the Gray Level Run Length Matrix (GLRLM), the Gray Level Size

Zone Matrix (GLSZM), and the Gray Level Dependence Matrix (GLDM), which capture tumor heterogeneity and microstructural complexity⁴⁷. The use of convolutional filters expands the number of extractable features into the thousands and thus enables for a comprehensive analysis of tumor features. However, due to the high dimensionality of radiomics data, feature selection techniques are used to eliminate redundant or non-informative features. Machine learning algorithms, including logistic regression, random forests, and Support Vector Machines (SVMs), are commonly used for feature selection and predictive modeling⁸.

Deep learning and convolutional neural networks

While traditional radiomics relies on explicit feature engineering, deep learning (DL) techniques, particularly CNNs, have introduced a paradigm shift in medical image analysis by automatically learning hierarchical feature representations from imaging data^{48,49}. CNNs eliminate the need for manual feature extraction by autonomously identifying meaningful imaging biomarkers, thus improving the objectivity, reproducibility, and generalizability of AI-driven radiomics models⁵⁰.

The use of CNNs in oncologic imaging has enabled the detection of subtle textural and morphologic changes that are often imperceptible to the human eye. Studies have shown that deep learning-based radiomics models outperform conventional machine learning approaches in predicting tumor recurrence, response to therapy and patient survival outcomes⁵¹. Additionally, CNNs have been integrated into multimodal imaging pipelines that combine radiomics with histopathologic, genomic, and clinical data to further improve prediction accuracy. However, a key challenge in deep learning-based radiomics is the need for large, high-quality annotated datasets to train robust models, highlighting the importance of data harmonization and federated learning approaches^{52–54}.

Habitat imaging

A promising extension of radiomics is habitat imaging, an approach that segments tumors into biologically distinct subregions (habitats) based on differences in vascularity, hypoxia and cellular composition. Tumors are inherently heterogeneous. Different regions have diverse microenvironmental conditions that can influence response to treatment and disease progression¹². By identifying these intra-tumoral subregions, habitat

imaging provides a more detailed characterization of tumor biology and enables refined risk stratification and personalized treatment selection.

Automated habitat imaging methods use unsupervised learning techniques such as histogram-based clustering, Gaussian mixture models and the Fit-Cluster-Fit approach to differentiate tumor subregions⁵. Recent studies have shown that integrating habitat imaging with multiparametric MRI and PET improves the prediction of tumor response to radiotherapy and systemic therapy⁵⁵. However, standardization of habitat imaging methods remains a challenge, as variations in imaging acquisition parameters can affect habitat definitions and model reproducibility.

Standardization and reproducibility in radiomics

One of the major limitations in radiomics research is the lack of reproducibility between studies. This is due to the variability in imaging acquisition protocols, feature extraction methodologies and data pre-processing pipelines⁴⁶. To address this issue, the Image Biomarker Standardization Initiative (IBSI) was established to develop standardized recommendations for radiomics feature definitions, nomenclature and computational workflows⁴⁶. The adoption of IBSI-compliant radiomics pipelines has been shown to significantly improve the reproducibility of radiomics-based biomarkers and facilitate their translation into clinical practice⁵⁶.

Further advances in the standardization of radiomics have led to the development of the CLEAR checklist, a comprehensive framework consisting of 58 key items designed to guide researchers in study design, methodology reporting, and statistical validation⁵⁷. The CLEAR checklist emphasizes rigorous feature selection, external validation, and transparent reporting of radiomics findings, to ensure that AI-driven biomarkers meet the necessary criteria for clinical application.

PREDICTIVE MODELS IN ONCOLOGIC IMAGING

The integration of radiomics-based predictive models into oncologic imaging has significantly improved the ability to extract clinically relevant insights from medical images. By leveraging quantitative imaging biomarkers, these models contribute to various aspects of precision oncology, including risk assessment, diagnosis, prognosis, prediction of response to treatment and toxicity evaluation^{36,43}. Radiomics has been

increasingly recognized for its role in identifying phenotypic tumor features that are not readily visible through conventional radiological assessment, thereby refining clinical decision-making and facilitates personalized treatment strategies^{53,58}.

Predictive models can be categorized based on their clinical objectives. Susceptibility models assess an individual's predisposition to develop cancer, and thus help with early risk stratification. Diagnostic models differentiate between disease subtypes or confirm the presence of a tumor with higher specificity than traditional imaging criteria. Prognostic models estimate the likelihood of disease progression, recurrence and overall survival, guiding long-term clinical management. Predictive models evaluate an individual's expected response to a particular therapy, helping to optimize treatment selection. In addition, toxicity models predict treatment-related adverse effects, allowing clinicians to modify therapeutic regimens accordingly^{54,59}.

Development and validation of predictive models

The construction of a robust predictive model follows a structured workflow that encompasses data acquisition, feature selection, model training validation and performance assessment. The predictive capability of a model is directly influenced by the quality, diversity and representativeness of the input data. Large, multi-institutional datasets are preferred to ensure generalizability. In many cases, however, data availability is limited to cohorts from a single center, necessitating internal validation strategies.

Model validation is essential for assessing performance, generalizability and clinical reliability. The hold-out method is the most commonly used approach for data partitioning, in which the dataset is split into a training set for model development and a validation set for estimating future performance on unknown data. To mitigate overfitting, the validation data must remain completely unknown during training. Ideally, external validation is performed with data from independent institutions to ensure robustness. However, if such datasets are not available, internal validation approaches are used⁶⁰.

In single-center studies, the split between training and validation splits may be random, temporal, or stratified to ensure a balanced class distribution (e.g. benign vs. malignant tumors). Statistical tests including the Mann-Whitney U test, the Kolmogorov-Smirnov test or the Shapiro-Wilk test are often used to verify that the

distributions of selected features remain comparable between the training and validation datasets. This ensure that the model learns clinically meaningful patterns rather than dataset-specific biases⁶¹.

When limited sample sizes pose a challenge for model training, K-fold cross-validation is used as a robust alternative. In this technique, the dataset is split into K subsets (typically 5 or 10), with K-1 folds used for training and the remaining fold reserved for validation. This process is repeated K times, ensuring that each subset is used once for testing, and the final model performance is given as the average of all iterations. Cross-validation reduces the variance introduced by the random split of training and testing, leading to more reliable performance estimates⁶².

Optimization and performance evaluation of models

Predictive models often incorporate hyperparameters that cannot be learned directly from the training data and need to be tuned to optimize performance. Tuning hyperparameters is crucial to prevent overfitting and underfitting, which are among the major limitations of machine learning models⁴⁶. Overfitting occurs when a model learns incorrect patterns that are specific to the training data, resulting in poor generalization to external datasets. In contrast, underfitting occurs when the model is too simplistic and fails to capture meaningful relationships within the data, resulting in suboptimal performance in both the training and validation sets⁶³.

To mitigate these issues, regularization techniques such as LASSO (Least Absolute Shrinkage and Selection Operator) regression and dropout layers are often used in deep learning architectures⁶⁴. Ensemble learning approaches that combine multiple models (e.g. random forests, gradient boosting or stacked models) have been shown to improve the robustness of the prediction⁶⁵. The performance evaluation of prediction models is based on standard metrics, including:

- Accuracy: measures the overall correctness of the predictions.
- Sensitivity (recall): captures the ability of the model to detect true positive cases (e.g. identifying malignant tumors).
- Specificity: indicates the ability of the model to correctly classify negative cases.
- Area under the Receiver Operating Characteristic Curve (AUC-ROC): evaluates the ability of the model to discriminate between different classes.

- Dice Similarity Coefficient (for segmentation models): evaluates the overlap between predicted and ground-truth tumor regions.

Multivariate models and feature selection

Single-feature models are rarely sufficient for accurate predictions, as radiomics-based biomarkers are often highly correlated with one another. Multivariate predictive models that include multiple imaging and clinical variables are the standard approach in radiomics research. However, increasing the number of input features leads to the curse of dimensionality, so feature selection and dimensionality reduction techniques are required⁶⁶.

Common methods for feature selection include:

- Principal Component Analysis (PCA): reduces the dimensionality of features while retaining the most informative components.
- Recursive Feature Elimination (RFE): iteratively removes the least important features based on model performance.
- Mutual Information and Correlation Analysis: identifies non-redundant, informative features.

Using these methods improves the interpretability, reproducibility, and clinical applicability of predictive models and ensures that the selected biomarkers remain relevant and generalizable across different patient cohorts.

Tumor detection and classification

There are now many AI models that have proven their effectiveness in detecting and classifying tumors in various organs such as breast, prostate, lung, or brain. In particular, AI models have shown remarkable accuracy in detecting breast cancer. A recent study, MASAI (Mammography Screening with Artificial Intelligence), has shown that the use of AI in mammography screening increased breast cancer detection by 29%, reduced physician workload by 44.2%, and did not increase the number of false positives⁶⁷. The AI-based approach using the FCBFormer model achieves very high accuracy in classifying lesions according to the BI-RADS scale (ACC 0.95, F1 0.92 and AUROC 0.99), which is a great improvement over the previous model⁶⁸. For prostate cancer detection, automated AI models achieve a sensitivity of 0.67, specificity of 0.73 and accuracy of 0.72 compared to radiologists who achieve a sensitivity of 0.81, specificity of 0.62 and accuracy of 0.66, using histopathology as a reference⁶⁹. The use of CNNs in the detection and classification of lung cancer shows very good performance in all standard imaging

modalities and reduces false positives and negatives. AI models even detect small lung nodules that can easily be overlooked by radiologists⁷⁰. In the study by Pandit et al.⁷¹ the application of the Multispace Image Reconstruction (MIR) technique achieved an ACC of 0.99 in the classification of lung cancer and reduced processing time, outperforming previous models. Chattopadhyay et al.⁵⁵ achieved similarly good results with CNN in the classification and segmentation of brain tumors (ACC 0.99).

Prediction of histologic and molecular type (virtual biopsy)

Information on the histological type, molecular, and immunological profile of the tumor is essential for treatment planning and patient stratification. However, these assessments require a biopsy, which is associated with the risk of side effects and does not always provide a complete picture of the tumor, as its composition is often heterogeneous. Thanks to radiomic biomarkers and developed AI models, it is increasingly possible to predict these features with increasing accuracy from the analysis of imaging studies.

Considering its non-invasiveness, completeness, accessibility and speed, virtual biopsy (VB) will certainly increasingly replace classical biopsy and limit its application to doubtful cases. Both the development of more efficient AI algorithms and improvements in imaging techniques will certainly contribute to this. A notable example is the work of Shah et al. who developed a machine learning model for radiomics that uses Random Forest and other classifiers to distinguish small cell lung cancer (SCLC) from other lung lesions on computed tomography scans. Their model achieved an AUC of up to 0.88, demonstrating the potential of radiomics for the early detection of SCLC⁷². Baldwin et al.⁷³ validated a Lung Cancer Prediction Convolutional Neural Network (LCP-CNN) for the prediction of malignancy of lung nodules and achieved an AUC of 0.90, sensitivity of 99.6%, the model analyzed 1397 nodules and showed the potential for improved risk stratification and reduction of unnecessary follow-up. Wang et al.⁷⁴ developed a deep learning model to predict EGFR mutation status in lung cancer patients based on contrast-enhanced CT images and achieved an AUC of 0.81 in the validation cohort. In breast cancer research using contrast-enhanced mammography, Petrillo et al.⁷⁵ applied radiomics and artificial intelligence to classify malignant and benign lesions (ACC 0.96), predict tumor grading (ACC 0.84), and identify HER2+ (ACC 0.89)

hormone receptor and HR+ (ACC 0.95). For gastrointestinal stromal tumors (GIST), a CT-based radiomics model in an external validation cohort achieved an AUC of 0.94 for discriminating low-risk from high-risk malignancies. Interestingly, similar AUCs were found for models using non-contrast and contrast-enhanced CT data⁷⁶. In another study, a CT-based radiomics model for predicting the Ki67 index in patients with GIST achieved an AUC of 0.78 in an external validation⁷⁷.

Predicting survival and response to treatment

Predicting survival and response to treatment is a key component of personalized medicine, and the development of methods based on artificial intelligence and radiomic analysis is significantly improving the accuracy of prediction. In recent years, numerous studies have shown that machine learning and deep learning models can predict treatment outcomes and stratify patients based on radiomics features, opening up new possibilities in precision oncology. A radiomics-based prediction model for pediatric neuroblastoma that analyzed MRI data from 513 patients in the PRIMAGE project significantly improved mortality risk stratification compared to the conventional INRGSS system, achieving a C-index of 0.79 and AUC 0.78 in the discovery cohort and significantly improving in the external validation set (C-index 0.93, AUC 0.95)⁷⁸.

Analyzing a collection of nearly 1,200 patients with non-small cell lung cancer (NSCLC), Hosny et al.⁷⁹ developed a 3D convolutional neural network (CNN) to predict 2-year overall survival using CT data and achieved an AUC of 0.70 ($p < 0.001$) for patients treated with radiotherapy and an AUC of 0.71 ($p < 0.001$) for patients treated with surgery. The CNN outperformed models based only on clinical parameters and engineered radiomic features alone, demonstrating its robustness in stratifying high- and low mortality risk groups. Sun et al.⁸⁰ developed a radiomics-based model using contrast-enhanced CT to assess tumor-infiltrating CD8 cells and predict response to anti-PD-1/PD-L1 immunotherapy in patients with advanced solid tumors. The model was trained on 135 patients and validated in independent datasets. The biomarker effectively discriminated between inflamed and immunodeficient tumors (AUC 0.76, $p < 0.0001$) and stratified immunotherapy-treated patients into high- and low-risk groups. A high radiomics score was associated with prolonged overall survival (HR 0.58, $p = 0.0081$) and better disease control at 6 months ($p = 0.013$).

Integration of multimodal biomedical data and development of a CDSS

Advances in oncology technology are paving the way for the development of a sophisticated Clinical Decision Support System (CDSS) that integrates multiple data sources and assists in real-time diagnostic and therapeutic decisions. Such a system could support every phase of patient care, from the initial consultation with an oncologist to long term follow-up care. In oncology, there is no single predictive marker that can fully capture the biological complexity of malignancies. Therefore, integrated predictive models that combine radiomics with other biomarkers allow for better classification of tumors, assessment of their aggressiveness and prediction of response to treatment. The implementation of such models based on systemic tumor biology enables:

- Identification of tumor development mechanisms.
- More precise classification of tumors based on their unique characteristics.
- Integration of genetic and tumor protein expression data, imaging parameters, and phenotypic data.
- A comprehensive understanding of cancer biology to support more accurate diagnosis, prognosis and tailored therapeutic strategies for patients^{10,81}.

As expected, models that incorporate not only radiomics but also clinical, molecular and laboratory data outperform models based on imaging alone. This has been the focus of numerous studies. In the study by Hao et al.⁸² a machine learning-based classification model for predicting anaplastic lymphoma kinase (ALK) rearrangement status in non-small cell lung cancer (NSCLC) was developed using non-enhanced CT images and clinical features. The study included 193 patients (154 training, 39 validation), from which 157 radiomic features and 8 clinical parameters were extracted. The best performing Support Vector Machine (SVM) model achieved an AUC of 0.91 in the validation cohort, outperforming models based only on clinical (AUC 0.73) and radiomics data alone (AUC 0.890). The radiomics model using the habitat method in combination with clinical data showed high performance (AUC 0.83 in the validation cohort, AUC 0.81 in the external test sets) in predicting EGFR mutation status in I stage of NSCLC. The radiomics-only model achieved an AUC of 0.81 and 0.79, respectively⁸³. In a study by Koyama et al.⁸⁴ an AI model that used patient characteristics, oncologic treatment history, and radiomic features from contrast-enhanced CT predicted overall survival in patients with NSCLC with a C-index of 0.84, outperforming the Cox proportional hazards model (C-index 0.775).

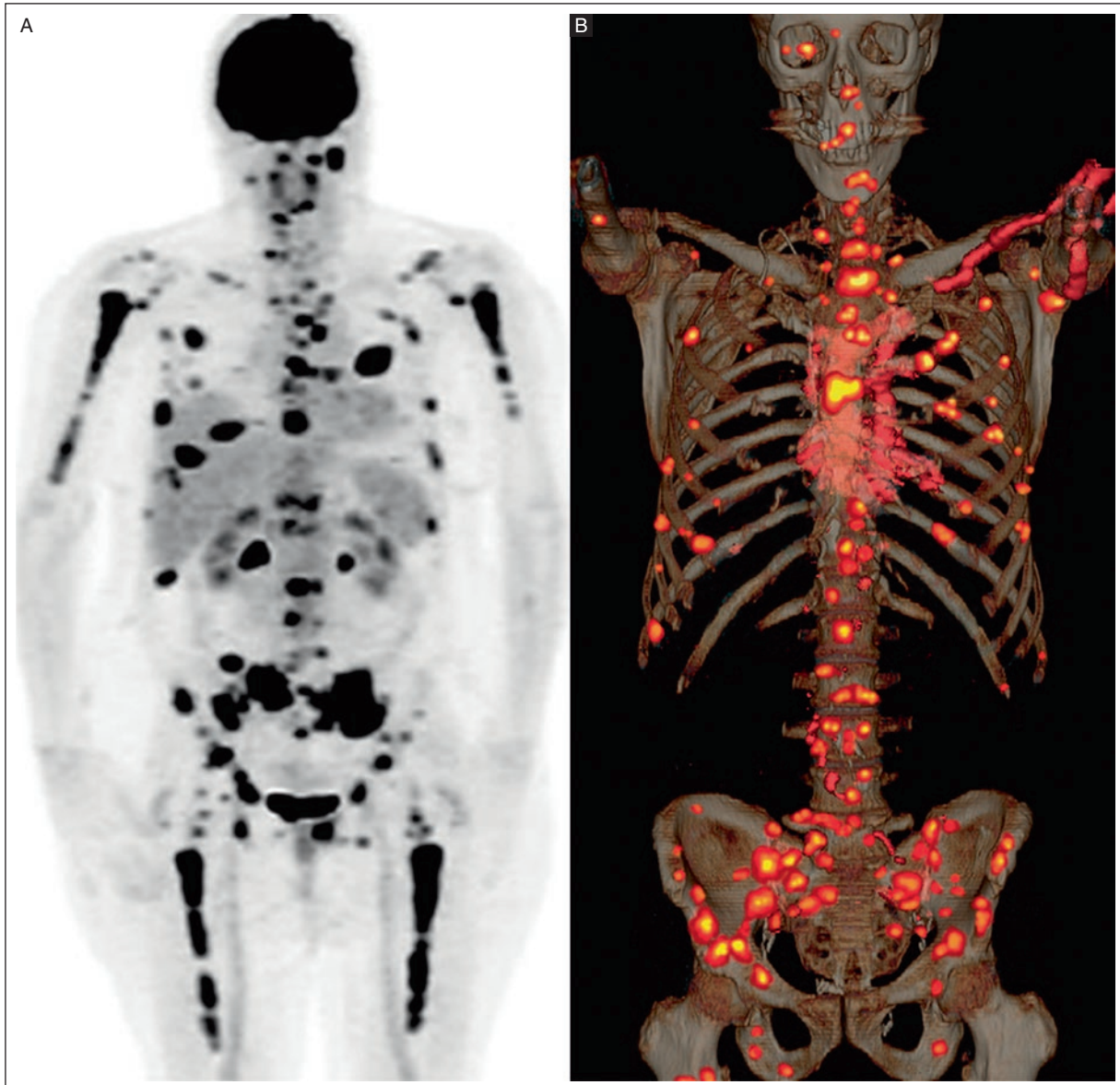


Figure 1. A: [^{18}F] FDG-PET scan of a patient with multiple myeloma, highlighting metabolic activity. **B:** 3D-rendered bone CT with PET-based tumor segmentation to quantify radiomic features.

CT: computed tomography; [^{18}F] FDG: $^{18}\text{Fluorine-fluorodeoxyglucose}$; PET: positron emission tomography.

The model successfully identified patients at high risk of poor prognosis, e.g., those who responded poorly to pembrolizumab despite high PD-L1 expression. Zhang et al.⁸⁵ explored radiomics and AI in the prognosis of pancreatic ductal adenocarcinoma, integrating imaging biomarkers with genomic and clinical data.

A transfer learning-based CNN model significantly improved the prediction of overall survival (AUC 0.81), outperforming traditional radiomics models (AUC 0.54) with a hazard ratio of 1.86 (95% CI 1.15-3.53, $p = 0.04$). Othman et al.⁸⁶ presented a deep learning model for

breast cancer survival prediction combining clinical, gene expression, and copy number alteration data. Feature extraction was performed using CNNs, followed by classification using LSTM and GRU networks. Decision-level fusion using a voting classifier improved prediction accuracy and achieved an AUC of 0.982, outperforming the individual models (GRU: AUC 0.96, LSTM: AUC 0.95). Park et al.⁸⁷ developed a radiomics-based model using preoperative MRI to estimate disease-free survival (DFS) in invasive breast cancer. A combined radiomics-based nomogram integrating MRI findings and clinicopathologic

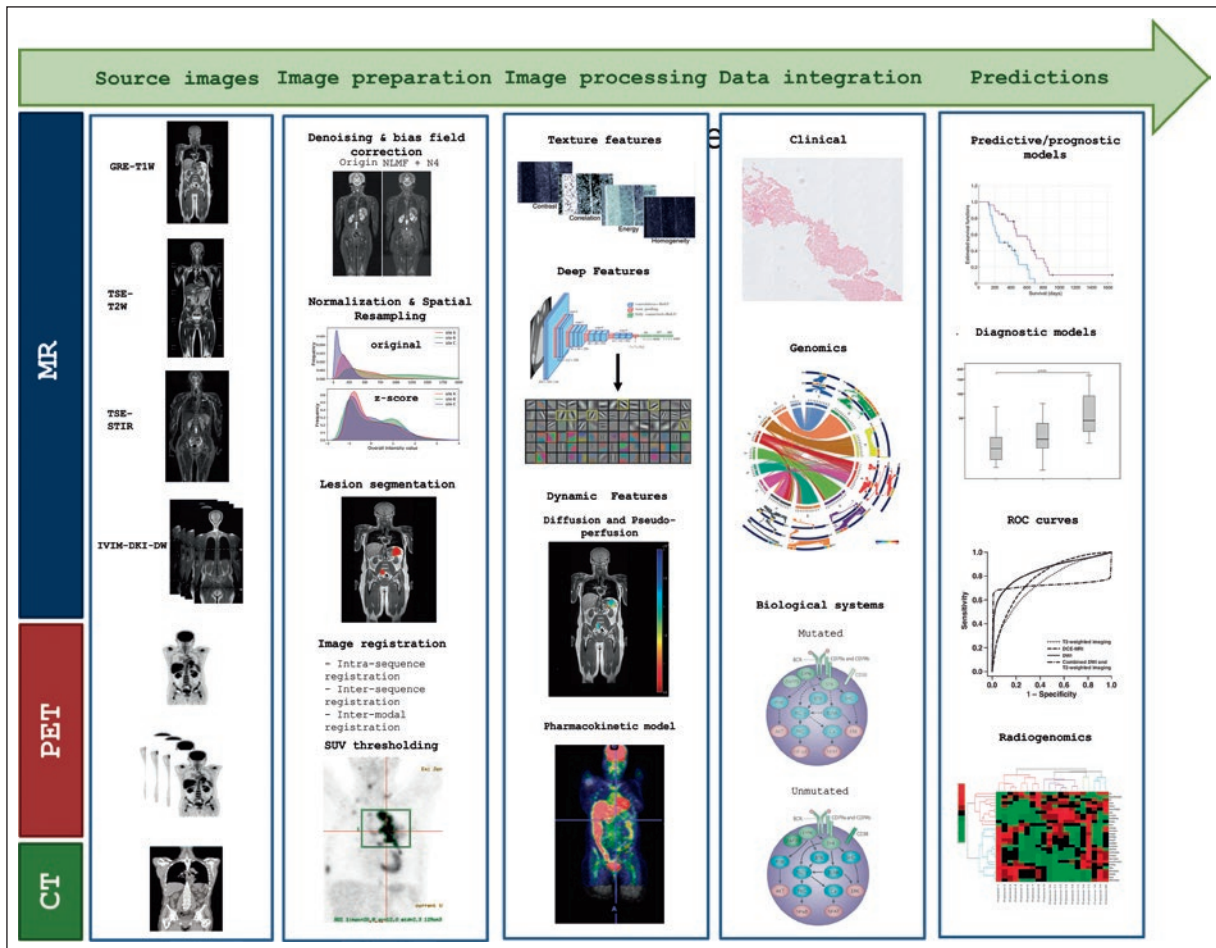


Figure 2. Image processing pipeline for multiple myeloma, integrating CT, MRI, and PET images as source data. The pipeline includes image preparation (image harmonization, registration and lesion detection), processing (quantitative extraction of imaging features) and data integration to develop predictive models for improved disease characterization.

CT: computed tomography; MRI: magnetic resonance imaging; PET: positron emission tomography.

data outperformed traditional models, achieving a C-index of 0.76 compared with 0.72 for clinicopathologic features alone and 0.67 for the Rad-score alone. Chitalia et al.⁸⁸ analyzed preoperative DCE-MRI scans of breast cancer patients and extracted 60 radiomics texture and morphology features to classify tumor heterogeneity. The high heterogeneity phenotype correlated with aggressive tumor features and significantly worse 10-year survival without recurrence ($p < 0.05$). The inclusion of radiomics phenotypes in a Cox model improved the accuracy of recurrence prediction (C-index 0.73) compared to models using only histopathologic markers (C-index 0.55).

The implementation of a CDSS capable of dynamically analyzing multimodal information integrating clinical, imaging, molecular, and laboratory data requires automation of data collection, extraction and predictive analysis processes. These can be modules embedded

in hospital systems or stand-alone digital platforms to which patient-specific diagnostic data are uploaded. The development of an efficient and automated CDSS marks a significant step towards next-generation personalized medicine that increases diagnostic accuracy, reduces errors and improves workflow efficiency. Ultimately, this approach will lead to better patient outcomes and a higher quality of life by enabling therapeutic decisions based on a comprehensive analysis of multimodal data.

CHALLENGES OF APPLYING AI IN ONCOLOGY IMAGING

AI offers a great opportunity in oncology, but clinical applications of AI remain limited due to lack of trust, ethical concerns, and regulatory challenges. Without the

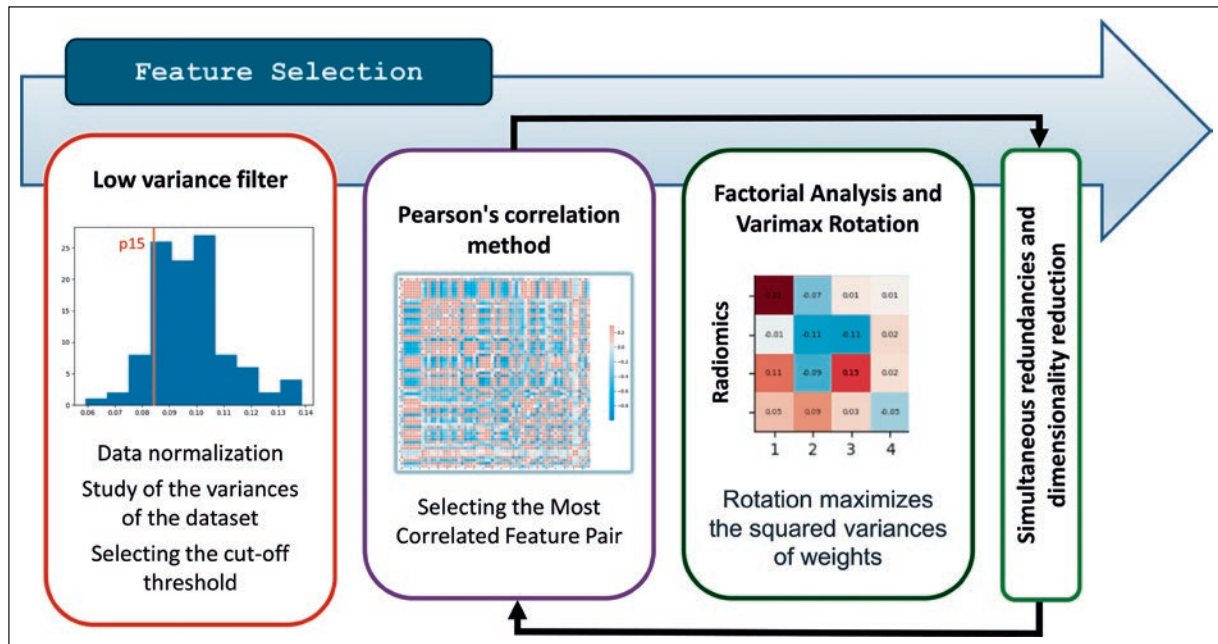


Figure 3. Feature selection is a two-step process: first, a low variance filter is applied to remove non-informative features. In the second step, an iterative approach is used to reduce dimensionality and redundancy. Pearson's correlation to identify the most highly correlated pairs of features is combined with factorial analysis and Varimax rotation to maximize the squared variance of the weights to improve the interpretability of the features.

transparency and interpretability of AI tools (the black box problem), clinicians may be reluctant to rely on AI to make critical decisions. Key aspects of any project must ensure GDPR compliance. These include conducting Data Protection Impact Assessments (DPIAs), defining roles for users and data controllers, and implementing safeguards such as encryption and access restrictions to protect patients from being identified. When developing AI, it is important to find a balance between data protection and data accessibility. Data must be anonymized or pseudonymized in accordance with the requirements of the General Data Protection Regulation (GDPR). Pseudonymization makes it possible to link the data to the patient, if necessary, while full anonymization is more difficult to reverse, but complies better with the regulations. In addition, the development of AI is often limited by insufficient access to an adequate quantity and quality of medical data, its harmonization and problems with the integration and standardization of data from different modalities¹⁷.

AI models in healthcare require large amounts of data to effectively train and validate models. However, access to large, publicly available datasets remains limited, and accessible data often lacks consistency or does not reflect the full diversity of clinical cases. To overcome these challenges, it is essential to develop

open repositories that are accessible to researchers. A major problem is the cost of maintaining these large-scale data infrastructures. In addition, hospitals and health systems are often unwilling to share data for fear of data breaches and liability claims¹. To overcome these challenges, better collaboration between research projects is urgently needed, especially with regard to data standardization and interoperability. A key issue is maintaining access to databases after individual projects have been completed - datasets become inaccessible, which affects the long-term impact of research.

One promising solution is federated data sharing projects, which ensure that valuable datasets from completed projects remain available. One example of this approach is EUCAIM (European Federation for Cancer Images), which integrates and preserves cancer imaging data across multiple initiatives^{20,89}. In addition, harmonizing AI and data infrastructures between institutions and research projects will help reduce redundancy, improve efficiency, and accelerate progress in medical AI. By promoting a standardized, secure and collaborative data ecosystem, researchers will be able to fully exploit the potential of AI and improve patient care and medical innovation²⁰. Effective AI-driven healthcare research requires the integration and standardization of data from different domains. For example, it must be

ensured that imaging repositories are compatible with databases containing clinical, histopathology, and genetic data. This is crucial for the development of a comprehensive AI-based CDSS.

A potential solution is the development of an integration profile to create a standardized database structure that combines medical data in a uniform system. The first approach to integrating the DICOM standard (for images) with MIABIS (for biobanks) was the PRIMAGE project⁹⁰. The new version of the MIABIS 3.0 standardization addresses the issue of integrating data from biobanks with omics and image data⁹¹. By harmonizing multimodal medical data infrastructures, researchers can reduce fragmentation, improve data usability, and promote more efficient collaboration in the development of medical AI. Establishing a universal standard for the integration of different medical datasets will be critical to allow to full potential of AI in precision medicine.

Particularly important for the successful development of AI in medicine is the establishment of the FUTURE-AI initiative in 2021, an international consortium of 117 experts, including AI specialists, clinicians, bioethicists, and social scientists from 50 countries. FUTURE-AI is a detailed set of principles and recommendations aimed at improving the safety, transparency and effectiveness of AI in healthcare. The framework is based on six key principles that form the acronym FUTURE:

- Fairness – tools should ensure equal performance for all patients.
- Universality – tools should be applicable in different clinical settings.
- Traceability – tools should include mechanisms for documentation and monitoring.
- Usability – tools should be intuitive and effective in clinical applications.
- Robustness – tools should remain reliable despite variations in input data.
- Explainability – tools should provide transparent and understandable decision-making processes.

These guidelines are designed to accelerate the implementation of trustworthy AI in clinical practice and cover the entire lifecycle of AI, including design, development, validation, deployment, and monitoring¹⁵.

CONCLUSION

The role of AI in oncology is rapidly evolving, particularly in image analysis. AI models based on deep learning are improving image preprocessing, segmentation and data analysis, improving the accuracy of

cancer diagnosis, prediction of response to treatment and patient prognosis. Studies consistently demonstrate the superiority of AI applications over traditional classification methods. The development of accurate AI tools relies on access to standardized, multimodal databases that facilitate better model training and validation. The next step is the implementation of AI-based CDSS that integrates image-derived features with other biomarkers and clinical data. However, before AI can be fully integrated into daily practice, several challenges still need to be overcome. These include standardizing research methods, ensuring access to high-quality medical data, complying with regulatory requirements and increasing the transparency of algorithms to boost clinicians' confidence. The development of international initiatives to regulate and standardize AI research and implementation is critical to the safe and effective adoption of these technologies in medicine, ultimately enabling personalized patient care and improved outcomes.

Funding

Not applicable

Conflicts of interest

The authors have no conflicts of interest to disclose.

Ethical considerations

Protection of humans and animals. The authors declare that no experiments involving humans or animals were conducted for this research.

Confidentiality, informed consent, and ethical approval. The study does not involve patient personal data nor requires ethical approval. The SAGER guidelines do not apply.

Declaration on the use of artificial intelligence. The authors declare that no generative artificial intelligence was used in the writing of this manuscript.

REFERENCES






1. Thrall JH, Li X, Li Q, Cruz C, Do S, Dreyer K, et al. Artificial Intelligence and Machine Learning in Radiology: Opportunities, Challenges, Pitfalls, and Criteria for Success. *J Am Coll Radiol*. 2018;15(3 Pt B):504-508; doi: 10.1016/j.jacr.2017.12.026.
2. Martí-Bonmatí L, Veiga-Canuto D, Cerdá Alberich L. Predictive model of the biological aggressiveness of neuroblastic tumors in children incorporating radiomics (Spanish). *An RANM* 2024;141(03):209-220; doi: 10.32440/ar.2024.141.03.rev02.
3. van Leeuwen KG, Schalekamp S, Rutten MJCM, van Ginneken B, de Rooij M. Artificial intelligence in radiology: 100 commercially available products and their scientific evidence. *Eur Radiol*. 2021;31(6):3797-3804; doi: 10.1007/s00330-021-07892-z.

4. Mello-Thoms C, Mello CAB. Clinical applications of artificial intelligence in radiology. *Br J Radiol.* 2023;96(1150):20221031; doi: 10.1259/bjr.20221031.
5. Alberich LC, Nebot CS, Alberich-Bayarri A, Carot Sierra JM, Martínez de Las Heras B, Veiga Canuto D, et al. A confidence habitats methodology in MR quantitative diffusion for the classification of neuroblastic tumors. *Cancers (Basel).* 2020;12(12):3858; doi: 10.3390/cancers12123858.
6. Li P, Li Z, Wang Z, Li C, Wang M. mResU-Net: multi-scale residual U-Net-based brain tumor segmentation from multimodal MRI. *Med Biol Eng Comput* 2024;62(3):641-651; doi: 10.1007/s11517-023-02965-1.
7. Martí-Bonmati L, Cerdá-Alberich L, Pérez-Girbés A, Díaz Beveridge R, Montalvá Orón E, Pérez Rojas J, et al. Pancreatic cancer, radiomics and artificial intelligence. *Br J Radiol.* 2022;95(1137): 20220072 doi: 10.1259/bjr.20220072.
8. Shur JD, Doran SJ, Kumar S, Ap Dafydd D, Downey K, O'Connor JPB, et al. Radiomics in oncology: A practical guide. *Radiographics.* 2021;41(6): 1717-1732. doi: 10.1148/rg.20211210037.
9. Alberich-Bayarri A, Hernández-Navarro R, Ruiz-Martínez E, García-Castro F, García-Juan D, Martí-Bonmati L. Development of imaging biomarkers and generation of big data. *Radiol Med.* 2017;122(6):444-448. doi: 10.1007/s11547-017-0742-x.
10. Veiga-Canuto D, Cerdá-Alberich L, Fernández-Patón M, Jiménez Pastor A, Lozano-Montoya J, Miguel Blanco A, et al. Imaging biomarkers and radiomics in pediatric oncology: a view from the PRIMAGE (PRedictive In silico Multiscale Analytics to support cancer personalized diagnosis and prognosis, Empowered by imaging biomarkers) project. *Pediatr Radiol.* 2024;54(4):562-570. doi: 10.1007/s00247-023-05770-y.
11. FUTURE-AI: international consensus guideline for trustworthy and deployable artificial intelligence in healthcare. *BMJ.* 2025;388:r340. doi: 10.1136/bmj.r340. Erratum for: *BMJ.* 2025;388:e081554. doi: 10.1136/bmj-2024-081554.
12. Cherezov D, Goldof D, Hall L, Gillies R, Schabath M, Müller H, et al. Revealing Tumor Habitats from Texture Heterogeneity Analysis for Classification of Lung Cancer Malignancy and Aggressiveness. *Sci Rep.* 2019;9(1):4500. doi:10.1038/s41598-019-38831-0.
13. Cui S, Traverso A, Niraula D, Zou J, Luo Y, Owen D, et al. Interpretable artificial intelligence in radiology and radiation oncology. *Br J Radiol.* 2023;96(1150): 20230142. doi: 10.1259/bjr.20230142.
14. Martí-Bonmati L, Koh DM, Riklund K, Bobowicz M, Roussakis Y, Vilanova JC, et al. Considerations for artificial intelligence clinical impact in oncologic imaging: an AI4HI position paper. *Insights Imaging.* 2022;13(1):89. doi:10.1186/s13244-022-01220-9.
15. Lekadir K, Frangi AF, Porras AR, Glocker B, Cintas C, Langlotz CP, et al. FUTURE-AI: International consensus guideline for trustworthy and deployable artificial intelligence in healthcare. *BMJ.* 2025; 388:e081554. doi: 10.1136/bmj-2024-081554. Erratum in: *BMJ.* 2025;388:r340. doi: 10.1136/bmj.r340.
16. Luchini C, Pea A, Scarpa A. Artificial intelligence in oncology: current applications and future perspectives. *Br J Cancer.* 2022;126(1):4-9; doi: 10.1038/s41416-021-01633-1.
17. Kondylakis H, Kalokyri V, Sfakianakis S, Marias K, Tsiknakis M, Jimenez-Pastor A, et al. Data infrastructures for AI in medical imaging: a report on the experiences of five EU projects. *Eur Radiol Exp.* 2023;7(1):20. doi: 10.1186/s41747-023-00336-x.
18. Clark K, Vendt B, Smith K, Freymann J, Kirby J, Koppel P, et al. The cancer imaging archive (TCIA): Maintaining and operating a public information repository. *J Digit Imaging.* 2013;26(6):1045-1057; doi: 10.1007/s10278-013-9622-7.
19. Sudlow C, Gallacher J, Allen N, Beral V, Burton P, Danesh J, et al. UK Biobank: An Open Access Resource for Identifying the Causes of a Wide Range of Complex Diseases of Middle and Old Age. *PLoS Med.* 2015;12(3):e1001779; doi: 10.1371/journal.pmed.1001779.
20. Martí-Bonmati L, Blanquer I, Tsiknakis M, Tsakou G, Martínez R, Capella-Gutiérrez S, et al. EUCAIM Consortium; European Society of Radiology. Empowering cancer research in Europe: the EUCAIM cancer imaging infrastructure. *Insights Imaging.* 2025;16(1):47. doi: 10.1186/s13244-025-01913-x.
21. Wilkinson MD, Dumontier M, Aalbersberg IJ, Appleton G, Axton M, Baak A, et al. The FAIR Guiding Principles for scientific data management and stewardship. *Sci Data.* 2016;3:160018. doi: 10.1038/sdata.2016.18. Erratum in: *Sci Data.* 2019;6(1):6. doi: 10.1038/s41597-019-0009-6.
22. Abbasi-Sureshjani S, Raumanns R, Michels BEJ, Shouten G, Cheplygina V. Risk of Training Diagnostic Algorithms on Data with Demographic Bias. In *Interpretable and Annotation-Efficient Learning for Medical Image Computing: Third International Workshop, iMIMIC 2020, Second International Workshop, ML3ID 2020, and 5th International Workshop, LABELS 2020, Held in Conjunction with MICCAI 2020, Lima, Peru, October 4-8, 2020, Proceedings 3.* Springer International Publishing, 2020:183-192. doi: 10.1007/978-3-030-61166-8_20.
23. Kalavathi P, Prasath VBS. Methods on Skull Stripping of MRI Head Scan Images-a Review. *J Digit Imaging.* 2016;29(3):365-379; doi: 10.1007/s10278-015-9847-8.
24. Sheller MJ, Edwards B, Reina GA, Martin J, Pati S, Kotrotsou A, et al. Federated learning in medicine: facilitating multi-institutional collaborations without sharing patient data. *Sci Rep.* 2020;10(1):12598. doi: 10.1038/s41598-020-69250-1.
25. Mugesan GK, McCrumb D, Aboian M, Verma T, Soni R, Memon F, et al. AI-Generated Annotations Dataset for Diverse Cancer Radiology Collections in NCI Image Data Commons. *Scientific Data.* 2024;11(1): 1165. doi: 10.1038/s41597-024-03977-8.
26. Koh DM, Papanikolaou N, Bick U, Illing R, Kahn CE Jr. Kalpathi-Cramer J, et al. Artificial intelligence and machine learning in cancer imaging. *Communications Medicine.* 2022;2(1):133. doi: 10.1038/s43856-022-00199-0.
27. Paudyal R, Shah AD, Akin O, Do RKG, Konar AS, Hatzoglou V, et al. Artificial Intelligence in CT and MR Imaging for Oncological Applications. *Cancers.* 2023;15(9):2573. doi: 10.3390/cancers15092573.
28. Orhac F, Eertink JJ, Cottreau AS, Zijlstra JM, Thieblemont C, Meignan M, et al. A Guide to ComBat Harmonization of Imaging Biomarkers in Multicenter Studies. *J Nucl Med* 2022;63(2):172-179. doi: 10.2967/jnumed.121.262464.
29. Fortin JP, Parker D, Tunç B, Watanabe T, Elliott MA, Ruparel K, et al. Harmonization of multi-site diffusion tensor imaging data. *Neuroimage.* 2017;161:149-170. doi:10.1016/j.neuroimage.2017.08.047.
30. Fernández Patón M, Cerdá Alberich L, Sangüesa Nebot C, Martínez de Las Heras B, Veiga Canuto D, Cañete Nieto A, et al. MR Denoising Increases Radiomic Biomarker Precision and Reproducibility in Oncologic Imaging. *J Digit Imaging.* 2021;34(5):1134-1145; doi: 10.1007/s10278-021-00512-8.
31. Abbasi S, Lan H, Choupan J, Sheikh-Bahaei N, Pandey G, Varghese B. Deep learning for the harmonization of structural MRI scans: a survey. *Biomed Eng Online.* 2024;23(1):90. doi: 10.1186/s12938-024-01280-6.
32. Tobari S, Tomoshige S, Muraki H, Oishi K, Iyatomi H. Domain-invariant feature learning in brain MR imaging for content-based image retrieval. *arXiv.* 2025:2501.01326.
33. Bonmati LM, Miguel A, Suárez A, Aznar M, Beregi JP, Fournier L, et al. CHAIMELEON Project: Creation of a Pan-European Repository of Health Imaging Data for the Development of AI-Powered Cancer Management Tools. *Front Oncol.* 2022;12:742701. doi: 10.3389/fonc.2022.742701.
34. Nan Y, Del Ser J, Walsh S, Schönlieb C, Roberts M, Selby I, et al. Data harmonisation for information fusion in digital healthcare: A state-of-the-art systematic review, meta-analysis and future research directions. *Inf Fusion.* 2022;82:99-122. doi: 10.1016/j.inffus.2022.01.001.
35. Orhac F, Boughdad S, Philippe C, Stalla-Bourdillon H, Nioche C, Champion L, et al. A Postreconstruction Harmonization Method for Multicenter Radiomic Studies in PET. *J Nucl Med.* 2018;59(8):1321-1328. doi: 10.2967/jnumed.117.199935.
36. Lambin P, Leijenaar RTH, Deist TM, Peerlings J, de Jong EEC, van Timmeren J, et al. Radiomics: the bridge between medical imaging and personalized medicine. *Nat Rev Clin Oncol.* 2017;14(12):749-762. doi: 10.1038/nrclinonc.2017.141.
37. Isaksson LJ, Summers P, Mastroleo F, Marvaso G, Corrao G, Vinci MG, et al. Automatic Segmentation with Deep Learning in Radiotherapy. *Cancers (Basel).* 2023;15(17):4389; doi: 10.3390/cancers15174389.
38. Ronneberger O, Fischer P, Brox T. U-Net: Convolutional Networks for Biomedical Image Segmentation. In *Medical image computing and computer-assisted intervention-MICCAI 2015: 18th international conference, Munich, Germany, October 5-9, 2015, proceedings, part III 18 (pp. 234-241).* Springer international publishing. doi: 10.1007/978-3-319-24574-4_28.
39. Isensee F, Jaeger PF, Kohl SAA, Maier-Hein KH. nnU-Net: a self-configuring method for deep learning-based biomedical image segmentation. *Nat Methods.* 2021;18(2):203-211; doi: 10.1038/s41592-020-01008-z.
40. Menze BH, Jakab A, Bauer S, Kalpathy-Cramer J, Farahani K, Kirby J, et al. The Multimodal Brain Tumor Image Segmentation Benchmark (BRATS). *IEEE Trans Med Imaging.* 2015;34(10):1993-2024. doi: 10.1109/TMI.2014.2377694.
41. Dosovitskiy A, Beyer L, Kolesnikov A, Weissenborn D, Zhai X, Unterthiner T, et al. An Image is Worth 16x16 Words: Transformers for Image Recognition at Scale. 2020. arXiv preprint arXiv:2010.11929.
42. Ghafoorian M, Karssemeijer N, Heskes T, van Uden IWM, Sanchez CI, Litjens G, et al. Location Sensitive Deep Convolutional Neural Networks for Segmentation of White Matter Hyperintensities. *Sci Rep.* 2017;7(1): 5110. doi: 10.1038/s41598-017-05300-5.
43. Gillies RJ, Kinahan PE, Hricak H. Radiomics: Images Are More than Pictures, They Are Data. *Radiology.* 2016;278(2):563-577. doi: 10.1148/radiol.2015151169.
44. Yip SSF, Aerts HJWL. Applications and limitations of radiomics. *Phys Med Biol.* 2016;61(13):R150-166; doi: 10.1088/0031-9155/61/13/R150.
45. Avanzo M, Stancanello J, Pirrone G, Sartor G. Radiomics and deep learning in lung cancer. *Strahlenther Onkol.* 2020;196(10):879-887. doi: 10.1007/s00066-020-01625-9.

46. Zwanenburg A, Vallières M, Abdalah MA, Aerts HJWL, Andrearczyk V, Apte A, et al. The image biomarker standardization initiative: Standardized quantitative radiomics for high-throughput image-based phenotyping. *Radiology*. 2020;295(2):328-338. doi: 10.1148/radiol.2020191145.
47. Mayerhoefer ME, Materka A, Langs G, Häggström I, Szczypiński P, Gibbs P, et al. Introduction to Radiomics. *J Nucl Med*. 2020;61(4):488-495; doi: 10.2967/jnumed.118.222893.
48. Lecun Y, Bengio Y, Hinton G. Deep learning. *Nature*. 2015;521(7553):436-444; doi: 10.1038/nature14539.
49. Mobadersany P, Yousefi S, Amgad M, Gutman DA, Barnholtz-Sloan JS, Velázquez Vega JE, et al. Predicting cancer outcomes from histology and genomics using convolutional neural networks. *Proc Natl Acad Sci. USA*. 2018;115(13):E2970-E2979. doi: 10.1073/pnas.1717139115.
50. Ardila D, Kiraly AP, Bharadwaj S, Choi B, Reicher JJ, Peng L, et al. End-to-end lung cancer screening with three-dimensional deep learning on low-dose chest computed tomography. *Nat Med*. 2019;25(6):954-961. doi: 10.1038/s41591-019-0447-x. Erratum in: *Nat Med*. 2019;25(8):1319. doi: 10.1038/s41591-019-0536-x.
51. Hosny A, Parmar C, Quackenbush J, Schwartz LH, Aerts HJ. Artificial intelligence in radiology. *Nat Rev Cancer*. 2018;18(8): 500-510. doi: 10.1038/s41568-018-0016-5.
52. Fuentes AM, Narayan A, Milligan K, Lum JJ, Brolo AG, Andrews JL, et al. Raman spectroscopy and convolutional neural networks for monitoring biochemical radiation response in breast tumour xenografts. *Sci Rep*. 2023;13(1):1530. doi: 10.1038/s41598-023-28479-2.
53. van Timmeren JE, Cester D, Tanadini-Lang S, Alkadhi H, Baessler B. Radiomics in medical imaging—"how-to" guide and critical reflection. *Insights Imaging* 2020;11(1):91. doi: 10.1186/s13244-020-00887-2.
54. Paschali M, Chen Z, Blankemeier L, Varma M, Yousef A, Bluetghen C, et al. Foundation Models in Radiology: What, How, Why, and Why Not. *Radiology*. 2025;314(2):e240597. doi:10.1148/radiol.240597.
55. Chattopadhyay A, Maitra M. MRI-based brain tumour image detection using CNN based deep learning method. *Neurosci Inform*. 2022;2(4):100060. doi: 10.1016/j.neuri.2022.100060.
56. Santinha J, Pinto dos Santos D, Laqua F, Visser JJ, Groot Lipman KBW, Dietzel M, et al. ESR Essentials: radiomics—practice recommendations by the European Society of Medical Imaging Informatics. *Eur Radiol*. 2025;35(3):1122-1132. doi: 10.1007/s00330-024-11093-9.
57. Kocak B, Baessler B, Bakas S, Cuocolo R, Fedorov A, Maier-Hein L, et al. CheckList for Evaluation of Radiomics research (CLEAR): a step-by-step reporting guideline for authors and reviewers endorsed by ESR and EuSoMI. *Insights Imaging*. 2023;14(1):75. doi: 10.1186/s13244-023-01415-8.
58. Aerts HJWL, Velazquez ER, Leijenaar RTH, Parmar C, Grossmann P, Carvalho S, et al. Decoding tumour phenotype by noninvasive imaging using a quantitative radiomics approach. *Nat Commun*. 2014;5:4006. doi: 10.1038/ncomms5006.
59. Kumar S, Virarkar M, Vulasala SSR, Daoud T, Ozdemir S, Wieseler C, et al. Magnetic Resonance Imaging Virtual Biopsy of Common Solid Renal Masses-A Pictorial Review. *J Comput Assist Tomogr*. 2023;47(2):186-198; doi: 10.1097/RCT.0000000000001424.
60. Bzdok D, Engemann D, Thirion B. Inference and Prediction Diverge in Biomedicine. *Patterns (NY)* 2020;1(8):100119. doi:10.1016/j.patter.2020.100119.
61. Vallières M, Kay-Rivest E, Perrin LJ, Liem X, Furstoss C, Aerts HJWL, et al. Radiomics strategies for risk assessment of tumour failure in head-and-neck cancer. *Sci Rep*. 2017;7(1): 10117 doi: 10.1038/s41598-017-10371-5.
62. Esteve A, Feng J, van der Wal D, Huang SC, Simko JP, DeVries S, et al. Prostate cancer therapy personalization via multi-modal deep learning on randomized phase III clinical trials. *NPJ Digit Med*. 2022;5(1):71 doi: 10.1038/s41746-022-00613-w. Erratum in: *NPJ Digit Med*. 2023;6(1):27. doi: 10.1038/s41746-023-00769-z.
63. Aliferis C, Simon G. Overfitting, Underfitting and General Model Overconfidence and Under-Performance Pitfalls and Best Practices in Machine Learning and AI. In: Simon GJ, Aliferis C, editors. *Artificial Intelligence and Machine Learning in Health Care and Medical Sciences: Best Practices and Pitfalls [Internet]*. Cham (CH): Springer; 2024.
64. Farhadi Z, Bevrani H, Feizi-Derakhshi MR. Combining regularization and dropout techniques for deep convolutional neural network. *IEEE Global Energy Conference, GEC 2022* 2022;335-339. doi: 10.1109/gec55014.2022.9986657.
65. Dang T, Nguyen TT, McCall J, Elyan E, Moreno-Garcia CF. Two-layer ensemble of deep learning models for medical image segmentation. *Cognit Comput*. 2024;16(3):1141-1160; doi: 10.1007/s12559-024-10257-5.
66. Jia W, Sun M, Lian J, Hou S. Feature dimensionality reduction: a review. *Complex & Intelligent Systems*. 2022; 8(3):2663-2693; doi: 10.1007/s40747-021-00637-x.
67. Hernström V, Josefsson V, Sartor H, Schmidt D, Larsson AM, Hofvind S, et al. Screening performance and characteristics of breast cancer detected in the Mammography Screening with Artificial Intelligence trial (MASAI): a randomised, controlled, parallel-group, non-inferiority, single-blinded, screening accuracy study. *Lancet Digit Health*. 2025;7(3): e175-e183. doi: 10.1016/S2589-7500(24)00267-X.
68. Bobowicz M, Badocha M, Gwozdziwicz K, Rygusik M, Kainowska P, Szurowska E, et al. Segmentation-based BI-RADS ensemble classification of breast tumours in ultrasound images. *Int J Med Inform*. 2024;189:105522. doi: 10.1016/j.ijmedinf.2024.105522.
69. Simon BD, Merriman KM, Harmon SA, Tetreault J, Yilmaz EC, Blake Z, et al. Automated Detection and Grading of Extraprostatic Extension of Prostate Cancer at MRI via Cascaded Deep Learning and Random Forest Classification. *Acad Radiol*. 2024;31(10):4096-4106. doi: 10.1016/j.acra.2024.04.011.
70. Javed R, Abbas T, Khan AH, Daud A, Bukhari A, Alharbey R. Deep learning for lung cancer detection: a review. *Artif Intell Rev*. 2024;57(8)197. doi: 10.1007/s10462-024-10807-1.
71. Pandit BR, Alsadoon A, Prasad PWC, Al Aloussi S, Rashid TA, Alsadoon OH, et al. Deep learning neural network for lung cancer classification: enhanced optimization function. *Multimed Tools Appl*. 2023;82(5):6605-6624. doi: 10.1007/s11042-022-13566-9.
72. Shah RP, Selby HM, Mukherjee P, Verma S, Xie P, Xu Q, et al. Machine Learning Radiomics Model for Early Identification of Small-Cell Lung Cancer on Computed Tomography Scans. *JCO Clin Cancer Inform*. 2021;5:746-757. doi: 10.1200/CCI.21.00021.
73. Baldwin DR, Gustafson J, Pickup L, Arteta C, Novotny P, Declerck J, et al. External validation of a convolutional neural network artificial intelligence tool to predict malignancy in pulmonary nodules. *Thorax*. 2020;75(4):306-312. doi:10.1136/thoraxjnl-2019-214104.
74. Wang S, Shi J, Ye Z, Dong D, Yu D, Zhou M, et al. Predicting EGFR mutation status in lung adenocarcinoma on computed tomography image using deep learning. *Eur Respir J*. 2019;53(3):1800986; doi: 10.1183/13993003.00986-2018.
75. Petrillo A, Fusco R, Di Bernardo E, Petrosino T, Barretta ML, Porto A, et al. Prediction of Breast Cancer Histological Outcome by Radiomics and Artificial Intelligence Analysis in Contrast-Enhanced Mammography. *Cancers (Basels)*. 2022;14(9): 2132. doi:10.3390/cancers14092132.
76. Zhang QW, Zhou XX, Zhang RY, Chen SL, Liu Q, Wang J, et al. Comparison of malignancy-prediction efficiency between contrast and non-contrast CT-based radiomics features in gastrointestinal stromal tumors: A multicenter study. *Clin Transl Med*. 2020;10(3):e291. doi: 10.1002/ctm2.91.
77. Zhao Y, Feng M, Wang M, Zhang L, Li M, Huang C. CT Radiomics for the Preoperative Prediction of Ki67 Index in Gastrointestinal Stromal Tumors: A Multi-Center Study. *Front Oncol*. 2021;11:689136. doi: 10.3389/fonc.2021.689136.
78. Lozano-Montoya J, Jimenez-Pastor A, Fuster-Matanzo A, Weiss GJ, Cerda-Alberich L, Veiga-Canuto D, et al. Risk stratification in neuroblastoma patients through machine learning in the multicenter PRIMAGE cohort. *Front Oncol*. 2025;15:1528836. doi:10.3389/fonc.2025.1528836.
79. Hosny A, Parmar C, Coroller TP, Grossmann P, Zeleznik R, Kumar A, et al. Deep learning for lung cancer prognostication: A retrospective multi-cohort radiomics study. *PLoS Med*. 2018;15(11):e1002711. doi: 10.1371/journal.pmed.1002711.
80. Sun R, Limkin EJ, Vakalopoulou M, Dercle L, Champiat S, Han SR, et al. A radiomics approach to assess tumour-infiltrating CD8 cells and response to anti-PD-1 or anti-PD-L1 immunotherapy: an imaging biomarker, retrospective multicohort study. *Lancet Oncol*. 2018;19(9):1180-1191. doi: 10.1016/S1470-2045(18)30413-3.
81. Russo L, Charles-Davies D, Bottazzi S, Sala E, Boldrini L. Radiomics for clinical decision support in radiation oncology. *Clin Oncol (R Coll Radiol)* 2024;36(8):e269-e281. doi: 10.1016/j.clon.2024.03.003.
82. Hao P, Deng BY, Huang CT, Xu J, Zhou F, Liu ZX, et al. Predicting anaplastic lymphoma kinase rearrangement status in patients with non-small cell lung cancer using a machine learning algorithm that combines clinical features and CT images. *Front Oncol*. 2022;12:994285; doi: 10.3389/fonc.2022.994285.
83. Wu J, Meng H, Zhou L, Wang M, Jin S, Ji H, et al. Habitat radiomics and deep learning fusion nomogram to predict EGFR mutation status in stage I non-small cell lung cancer: a multicenter study. *Sci Rep*. 2024;14(1):15877. doi: 10.1038/s41598-024-66751-1.
84. Koyama J, Morise M, Furukawa T, Oyama S, Matsuzawa R, Tanaka I, et al. Artificial intelligence-based personalized survival prediction using clinical and radiomics features in patients with advanced non-small cell lung cancer. *BMC Cancer*. 2024;24(1):1417. doi: 10.1186/s12885-024-13190-w.
85. Zhang Y, Lobo-Mueller EM, Karanicolas P, Gallinger S, Haider MA, Khalvati F. Prognostic Value of Transfer Learning Based Features in Resectable Pancreatic Ductal Adenocarcinoma. *Front Artif Intell*. 2020;3:550890. doi: 10.3389/frai.2020.550890.

86. Othman NA, Abdel-Fattah MA, Ali AT. A Hybrid Deep Learning Framework with Decision-Level Fusion for Breast Cancer Survival Prediction. *Big Data Cogn Comput.* 2023;7(1):50. doi: 10.3390/bdcc7010050.
87. Park H, Lim Y, Ko ES, Cho HH, Lee JE, Han BK, et al. Radiomics signature on magnetic resonance imaging: Association with disease-free survival in patients with invasive breast cancer. *Clin Cancer Res.* 2018;24(19):4705-4714; doi: 10.1158/1078-0432.CCR-17-3783.
88. Chitalia RD, Rowland J, McDonald ES, Pantalone L, Cohen EA, Gastounioti A, et al. Imaging phenotypes of breast cancer heterogeneity in preoperative breast dynamic contrast enhanced magnetic resonance imaging (DCE-MRI) scans predict 10-year recurrence. *Clin Cancer Res.* 2020; 26(4):862-869. doi: 10.1158/1078-0432.CCR-18-4067.
89. Kondylakis H, Catalan R, Alabart SM, Barelle C, Bizopoulos P, Bobowicz M, et al. Documenting the de-identification process of clinical and imaging data for AI for health imaging projects. *Insights Imaging.* 2024;15(1):130. doi: 10.1186/s13244-024-01711-x.
90. Scapicchio C, Gabelloni M, Forte SM, Alberich LC, Faggioni L, Borgheresi R, et al. DICOM-MIABIS integration model for biobanks: a use case of the EU PRIMAGE project. *Eur Radiol Exp.* 2021;5(1):20. doi:10.1186/S41747-021-00214-4.
91. Eklund N, Engels C, Neumann M, Strug A, van Enckevort E, Baber R, et al. Update of the Minimum Information About Biobank Data Sharing (MIABIS) Core Terminology to the 3rd Version. *Biopreserv Biobank.* 2024;22(4):346-362. doi: 10.1089/bio.2023.0074.

Diagnostic performance of lung POCUS in neonatal respiratory disorders in the neonatal intensive care unit: a new shortened protocol

Paul Montoya-Alarcon¹ , Samuel I. Espinoza-Tristan^{1,2*} , Mane M. Ayala-Duran¹ ,
Alexis A. De Leon-Perez³ , and Adrian A. Negreros-Osuna¹ 

¹Department of Radiology and Imaging; ²Pediatric Department, ISSSTE Hospital Regional Monterrey; ³School of Medicine, Universidad Autonoma de Nuevo Leon. Monterrey, Nuevo Leon, Mexico

ABSTRACT

Introduction: Lung point-of-care ultrasound (POCUS) has been useful in diagnosing neonatal respiratory disorders (NRDs); however, chest radiography (X-ray) is the most widely used imaging modality and the gold standard. This study aimed to determine the diagnostic performance of a new, shortened lung POCUS protocol compared with chest X-ray in NRD diagnosis. **Materials and methods:** This prospective cohort study was conducted from September 2023 to December 2024. Newborns from the neonatal intensive care unit (NICU) were consecutively included. A chest X-ray and a shortened lung POCUS protocol were performed. NRDs were recorded based on the imaging findings. The diagnostic performance of the shortened lung POCUS protocol was evaluated and compared with the gold standard, chest X-ray. **Results:** Sixty neonates were included; 14 (23.3%) had abnormal findings on chest X-ray, while 23 (38.3%) had abnormal findings on lung POCUS with the following NRD diagnoses: interstitial fluid overload ($n = 9$, 15.0%), respiratory distress syndrome ($n = 7$, 11.6%), pneumonia ($n = 6$, 10.0%), and transient tachypnea of the newborn (TTN) ($n = 1$, 1.6%). The shortened lung POCUS protocol had a sensitivity of 82.3% and a specificity of 79.1%, while chest X-ray had a sensitivity of 60.9% and a specificity of 91.9% for the diagnosis of NRDs in neonates in the NICU. **Conclusion:** This new shortened lung POCUS with an assessment of 10 lung areas had a higher sensitivity (82.3%) than chest X-ray (60.9%) for the diagnosis of NRDs in neonates in the NICU. To our knowledge, this study is the first in Mexico that focuses on comparing the performance of these two imaging modalities for diagnosing NRDs.

Keywords: Lung point-of-care ultrasound. Neonatal respiratory disorders. Neonatal intensive care unit. Diagnostic performance.

INTRODUCTION

Neonatal respiratory disorders (NRDs) are a leading cause of morbidity and mortality in neonates (0-7 days of life), with an incidence between 40 and 45% in neonatal intensive care units (NICUs)¹⁻³. NRDs include pneumonia (42.8%), respiratory distress syndrome (20.8%), transient tachypnea of the newborn (TTN) (13.6%),

meconium aspiration syndrome (7.9%), atelectasis (7.7%), and pneumothorax (2.8%)⁴⁻⁹. Chest radiography (X-ray) is the most widely used imaging method and the gold standard for diagnosing NRDs. However, it has some disadvantages, such as ionizing radiation exposure¹⁰, which due to the small size of the neonate and the proximity to radiosensitive tissues and organs, increases their susceptibility to radiation effects compared to other

*Corresponding author:

Samuel I. Espinoza-Tristan
E-mail: samuel.espinozat@udem.edu

Received for publication: 13-01-2025

Accepted for publication: 17-03-2025

DOI: 10.24875/JMEXFRI.M25000106

Available online: 15-07-2025

J Mex Fed Radiol Imaging. 2025;4(2):84-93

www.JMeXFRI.com

2696-8444 / © 2025 Federación Mexicana de Radiología e Imagen, A.C. Published by Permanyer. This is an open access article under the CC BY-NC-ND (<https://creativecommons.org/licenses/by-nc-nd/4.0/>).

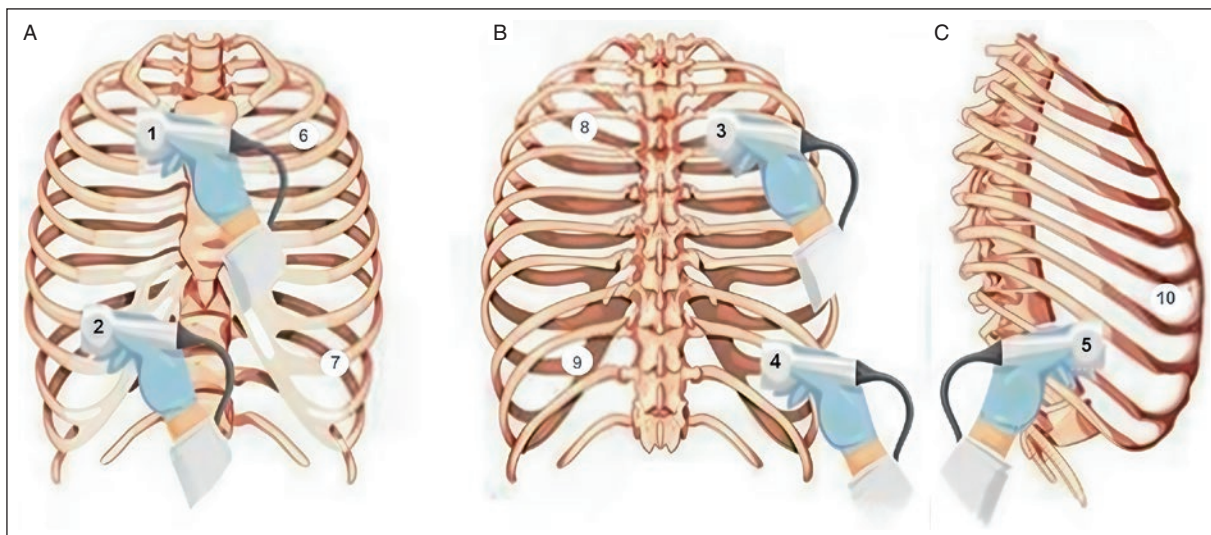


Figure 1. Shortened lung POCUS protocol. **A:** examination starts on the right side in the anterior apical region with the transducer oriented longitudinally in front of the anterior axillary line of the thorax (number 1). It continues with the anterior basal region. The transducer is oriented longitudinally at the level of the nipple at the base of the lung (number 2). **B:** the right posterior apical region is examined with the transducer oriented longitudinally in the paravertebral region in the interscapulovertebral space towards the apical zone of the chest (number 3). The right posterior basal region is examined with the transducer oriented longitudinally at the level of the inferior scapular angle (number 4). **C:** the right lateral basal region is examined with the transducer oriented longitudinally at the level of the mid-axillary line at the base of the lung (number 5). This shortened lung POCUS protocol is performed in the same order (number 6, 7, 8, 9 and 10) on the left side.

POCUS: point-of-care ultrasound.

age groups. There may also be false-positives, and limitations in interpretation due to anatomical and technical characteristics¹¹.

Neonatal point-of-care ultrasound (POCUS), first described in 1960, has been increasingly used over the last decade². Lung POCUS allows real-time imaging without radiation exposure with high sensitivity in detecting lung abnormalities, such as B-lines, consolidations, and the absence of A-lines¹⁰⁻¹⁴. Lung POCUS diagnostic accuracy varies from 82.7% to 100%^{2,4,7}. The conventional lung POCUS protocol evaluates 12 lung areas¹⁵, but its clinical implementation is complex because it requires scanning multiple anatomic regions of the thorax in different positions (supine, prone, and lateral)¹⁶⁻¹⁸. This protocol may be impractical due to neonatal movement caused by crying, the presence of catheters, cannulas, tracheal tubes, and other medical devices that restrict mobility and access to some thoracic regions. Because of these limitations, we propose a new, shortened lung POCUS protocol for detecting NRDs that reduces neonatal manipulation. This study aimed to determine the diagnostic performance of this new, shortened lung POCUS protocol compared to chest X-ray in NRDs diagnosis.

MATERIAL AND METHODS

This prospective cohort study was conducted from September 2023 to December 2024 in the Department of Radiology and Imaging of the tertiary-care ISSSTE Hospital Regional Monterrey in Monterrey, Nuevo Leon, Mexico. Neonates aged 24 hours to 28 days admitted to the neonatal intensive care unit (NICU) were included. Neonates with thoracic surgery or skin conditions that prevented safe use of the ultrasound transducer were excluded. Informed consent was obtained from parents or guardians. The institutional research and research ethics committee approved the study.

Study development and variables

Neonates routinely admitted to the NICU were observed and assessed for at least 24 hours. Chest X-ray were routinely performed. The NRD diagnoses were based on chest X-ray findings and lung POCUS examination. Lung POCUS examination included variables such as the pleural line, A-line, B-line, white lung, consolidation, and the double lung point sign.

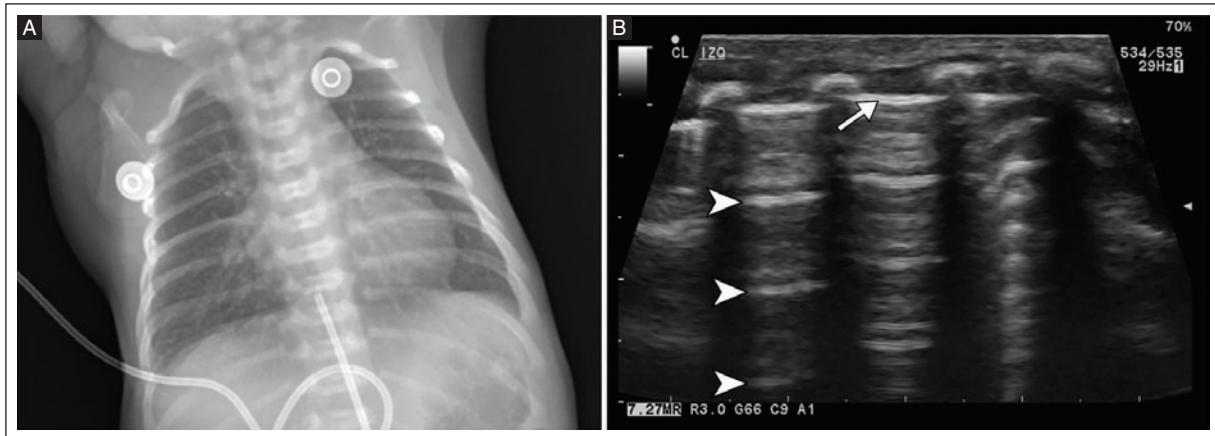


Figure 2. A healthy full-term neonate born by cesarean section at 39.5 weeks gestation with 24 hours of extrauterine life. **A:** a normal AP chest X-ray shows adequately expanded lungs with no abnormal findings. Umbilical catheter and electrodes are also visible. **B:** a normal lung POCUS shows a pleural line of normal thickness (white arrow) along with multiple A-lines (white arrowheads), which are typical findings in a normal lung. AP: anteroposterior; POCUS: point-of-care ultrasound; X-ray: radiography.

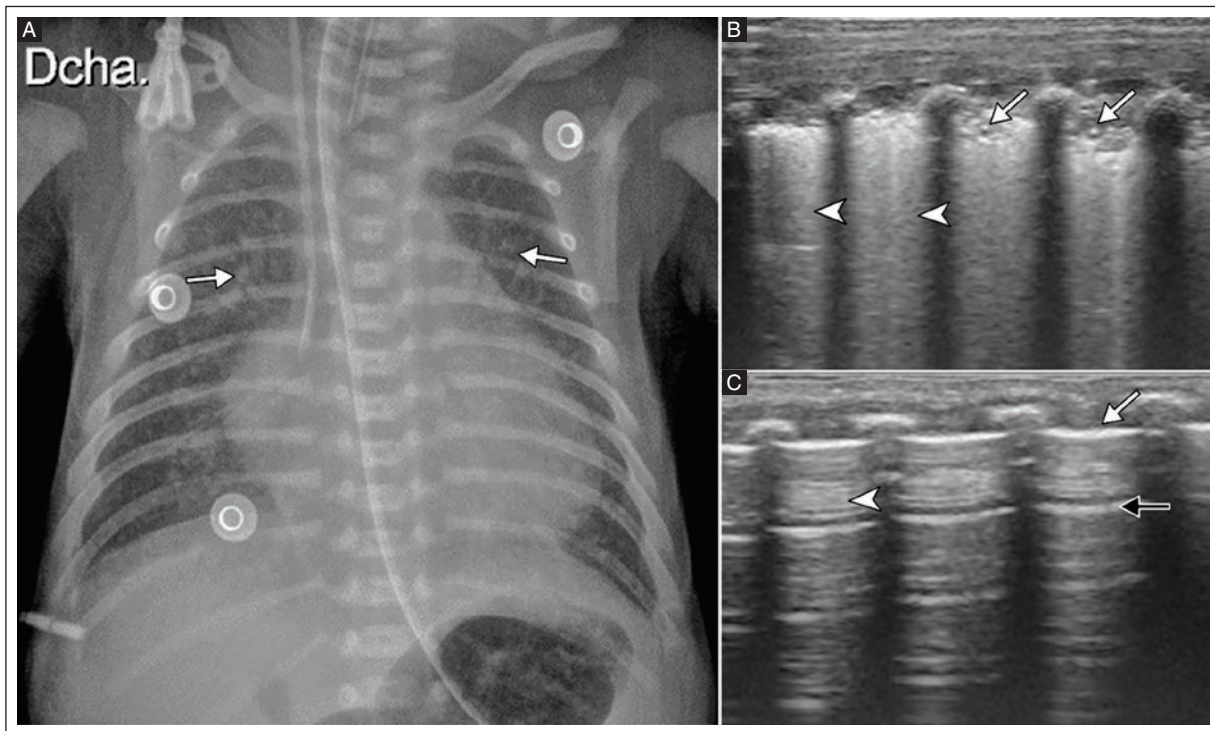


Figure 3. Male preterm neonate born by cesarean section at 30 weeks gestation with 24 hours of extrauterine life with an NRD requiring endotracheal ventilation. **A:** AP chest x-ray shows diffuse bilateral alveolar opacities (white arrows). An endotracheal tube, feeding tube, and central venous catheter are seen with the catheter tip projecting at the cavoatrial junction. **B:** lung POCUS of the left posterior-inferior quadrant shows loss of normal pleural line morphology and echogenicity due to subpleural focal atelectasis (white arrows) and an increased number of B-lines forming a “white lung pattern” (white arrowheads). **C:** lung POCUS of the right posterior-inferior quadrant shows a pleural line with normal echogenicity and thickness (white arrow), the presence of B-lines (white arrowhead), and preserved A-lines with a normal appearance (black arrow). The diagnosis was subpleural atelectasis on chest X-ray and shortened lung POCUS.

AP: anteroposterior; NRD: neonatal respiratory disorder; POCUS: point-of-care ultrasound; X-ray: radiography.

Table 1. Chest X-ray and shortened lung POCUS findings in 23 neonates diagnosed with NRDs in the NICU

Case	Chest X-ray findings	Radiological diagnosis	Lung POCUS findings							Lung POCUS diagnosis
			Pleural line	A line	B line	Consolidation	White lung	Double lung point		
1	Normal	Normal	Normal	Present	Present	Present	Present	Absent	Absent	Respiratory distress syndrome
2	Apex consolidation	Pneumonia	Normal	Present	Present	Present	Present	Absent	Absent	Respiratory distress syndrome
3	Reticular pattern	Interstitial fluid overload	Thickened	Absent	Present	Present	Present	Present	Absent	Pneumonia
4	Consolidation with air bronchogram	Pneumonia	Thickened	Absent	Present	Present	Present	Absent	Absent	Pneumonia
5	Reticular pattern	Interstitial fluid overload	Normal	Absent	Present	Present	Absent	Present	Absent	Interstitial fluid overload
6	Normal	Normal	Normal	Present	Absent	Present	Present	Absent	Absent	Respiratory distress syndrome
7	Reticular pattern	Interstitial fluid overload	Normal	Absent	Present	Present	Absent	Present	Absent	Respiratory distress syndrome
8	Reticular pattern	Interstitial fluid overload	Normal	Absent	Present	Present	Absent	Present	Absent	Respiratory distress syndrome
9	Reticular pattern	Interstitial fluid overload	Normal	Absent	Present	Present	Absent	Present	Absent	Respiratory distress syndrome
10	Normal	Normal	Normal	Present	Present	Present	Absent	Absent	Present	TTN
11	Consolidation	Pneumonia	Normal	Present	Present	Present	Present	Absent	Absent	Pneumonia
12	Normal	Normal	Normal	Present	Present	Present	Present	Absent	Absent	Respiratory distress syndrome
13	Reticular pattern	Interstitial fluid overload	Normal	Absent	Present	Present	Absent	Present	Absent	Interstitial fluid overload
14	Reticular pattern	Interstitial fluid overload	Normal	Absent	Present	Present	Absent	Present	Absent	Interstitial fluid overload
15	Normal	Normal	Normal	Absent	Present	Present	Absent	Present	Absent	Interstitial fluid overload
16	Consolidation with air bronchogram	Pneumonia	Thickened	Absent	Present	Present	Present	Absent	Absent	Pneumonia
17	Normal	Normal	Normal	Absent	Present	Present	Absent	Present	Absent	Interstitial fluid overload
18	Consolidation with air bronchogram	Pneumonia	Thickened	Absent	Present	Present	Present	Absent	Absent	Pneumonia
19	Normal	Normal	Normal	Absent	Present	Present	Absent	Present	Absent	Interstitial fluid overload
20	Consolidation with air bronchogram	Pneumonia	Thickened	Absent	Present	Present	Present	Absent	Absent	Pneumonia
21	Normal	Normal	Normal	Absent	Present	Present	Absent	Present	Absent	Interstitial fluid overload
22	Normal	Normal	Normal	Absent	Present	Present	Absent	Present	Absent	Interstitial fluid overload
23	Reticular pattern	Interstitial fluid overload	Normal	Absent	Present	Present	Absent	Present	Absent	Interstitial fluid overload

POCUS: point-of-care ultrasound; NRDs: neonatal respiratory disorders; NICU: neonatal intensive care unit; TTN: transient tachypnea of the newborn.

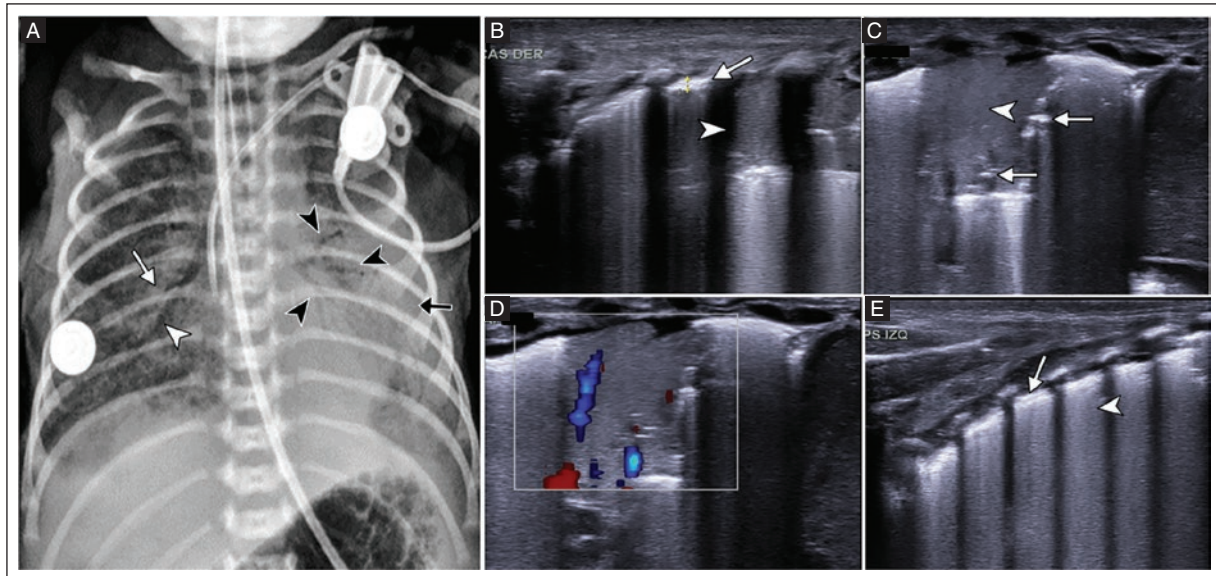


Figure 4. Full-term neonate at 37 weeks gestation with 5 days of extrauterine life with an NRD and fever. **A:** AP chest X-ray shows an area of consolidation in the right middle lobe (white arrow) with air bronchograms (white arrowhead). There are more areas of consolidation in the lingula and the posterior segment of the left lower lobe (black arrowheads) with air bronchograms (black arrowhead). A central venous catheter with a tip at the cavoatrial junction and an orogastric tube and electrodes can be seen. **B:** lung POCUS of the right anterior upper quadrant with pleural line thickening (white arrow) next to the consolidation area (white arrowhead). **C:** lung POCUS of the left hemithorax in the lateral quadrant with a focal subpleural parenchymal consolidation (white arrowhead) with air bronchograms (white arrows). Hepatization of the lung parenchyma was noted. **D:** lung POCUS, with color Doppler showing vascular flow in the same area of consolidation. **E:** lung POCUS of the left posterior upper quadrant showing pleural line thickening (white arrow) and increased B-lines corresponding to a "white lung pattern" (white arrowhead). The diagnosis was pneumonia on the chest X-ray and shortened lung POCUS.

AP: anteroposterior; NRD: neonatal respiratory disorder; POCUS: point-of-care ultrasound; X-ray: radiography.

New shortened lung POCUS protocol

Acuson NX3 equipment (Siemens Healthineers, Erlangen, Germany) with a linear transducer of 5-13 MHz was used. The technical parameters, previously described by Liu et al.⁹, were (a) 4-5 cm depth, (b) 1-2 focal zones close to the pleural line, (c) fundamental frequency imaging, (d) 2-3 speckle reduction imaging (SRI), (e) spatial compounding function (SCF), (f) and a time-gain compensation (TGC) setting. A pediatric radiologist (SET) with 11 years of experience assessed the chest X-ray and the shortened lung POCUS protocol.

The new, shortened lung POCUS protocol proposed by the author (SET) consists of assessing 10 areas in the thorax bilaterally at the anterosuperior, anteroinferior, lateral, posterosuperior, and posteroinferior levels, as described below.

Examination starts on the right side in the anterior apical region with the transducer oriented longitudinally in front of the anterior axillary line in the apical region of the thorax (Figure 1A) (number 1). It continues with the anterior basal region, with the transducer oriented

longitudinally at the level of the nipple at the base of the lung (number 2). The right posterior apical region is examined with the transducer oriented longitudinally in the paravertebral region in the interscapulovertebral space towards the apical region of the chest (Figure 1B) (number 3). The right posterior basal region is examined with the transducer oriented longitudinally at the level of the inferior scapular angle (number 4). The right lateral basal region is examined with the transducer oriented longitudinally at the level of the mid-axillary line at the base of the lung (Figure 1C) (number 5). This protocol is performed on the left side in the same order (numbers 6, 7, 8, 9, and 10).

Statistical analysis

Numerical variables are described with measures of central tendency and dispersion. Categorical variables as absolute numbers and percentages. A receiver operating characteristic (ROC) curve assessed the discriminatory ability of a dichotomous diagnosis. Sensitivity, specificity, positive predictive value (PPV), negative

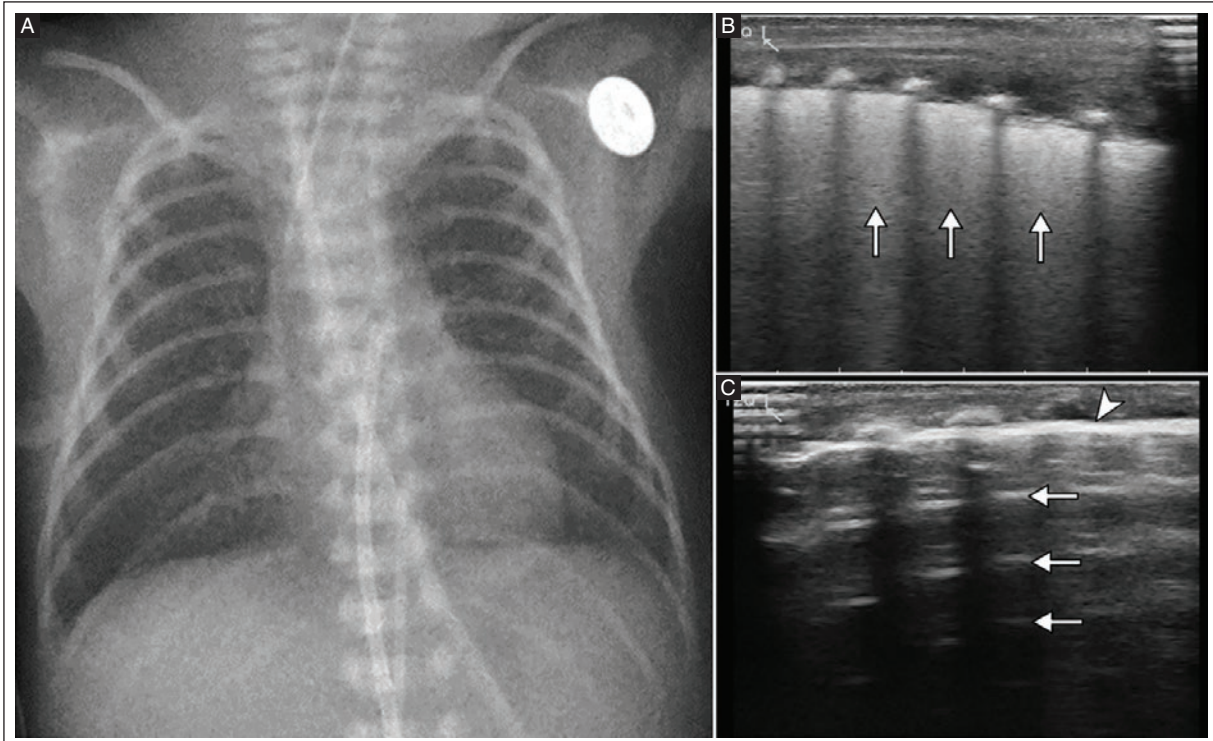


Figure 5. Full-term male neonate born by cesarean section at 38 weeks gestation with 24 hours of extrauterine life with an NRD and clinical suspicion of TTN. **A:** AP chest X-ray showing adequately expanded lung fields with no pathologic abnormalities. An endotracheal tube, an umbilical catheter and a gastric tube are visible. **B:** lung POCUS of the left posterior-inferior quadrant shows an increased number of B-lines resulting in a "white lung" appearance (wet lung pattern) (white arrows), along with obliteration of the A-lines, a finding consistent with interstitial fluid overload. **C:** lung POCUS of the left anterior-inferior quadrant with preserved A-lines (white arrows) and normal appearance of the pleural line (white arrowhead), consistent with a normal ultrasound pattern. The chest X-ray was normal. Shortened lung POCUS diagnosis was interstitial fluid overload.

AP: anteroposterior; NRD: neonatal respiratory disorder; POCUS: point-of-care ultrasound; TTN: transient tachypnea of the newborn; X-ray: radiography.

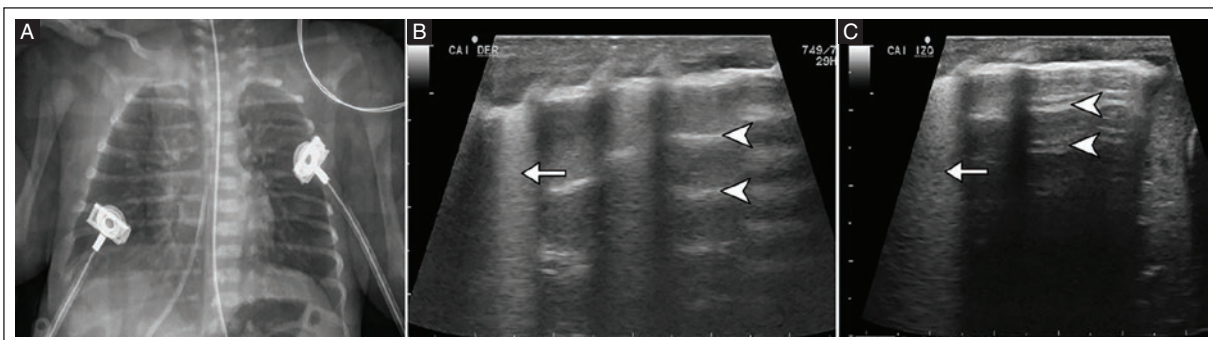


Figure 6. Preterm male neonate born at 32 weeks gestation with 24 hours of extrauterine life. **A:** AP chest X-ray showing normal lung fields. An umbilical catheter, electrodes and a feeding tube are seen. **B:** lung POCUS of the anterior and lower right quadrant shows a focal increase in B-lines (white arrow) with preservation of A-lines (white arrowheads), which together form the double lung point sign. **C:** lung POCUS of the anterior and lower left quadrant shows a focal increase of the B-lines (white arrow) with preservation of A-lines (white arrowheads) which together form the double lung point sign. The chest X-ray was normal. Shortened lung POCUS diagnosis was TTN.

AP: anteroposterior; POCUS: point-of-care ultrasound; TTN: transient tachypnea of the newborn; X-ray: radiography.

predictive value (NPV), and accuracy were calculated to determine the diagnostic performance of the shortened lung POCUS protocol compared to chest X-ray as the gold standard, and chest X-ray with the shortened lung POCUS protocol as the gold standard. Agreement between lung POCUS findings and chest X-ray findings was assessed with Cohen’s kappa coefficient. The 95% confidence interval (CI) was calculated and a value of $p < 0.05$ was significant. Data analysis was performed with SPSS v.25.0 (IBM Corp., Armonk NY, USA).

RESULTS

Sixty neonates were included, 27 (45.0%) females and 33 (55.0%) males. The mean gestational week was 35.4 ± 2.5 . Forty-four (73.3%) were preterm neonates with a mean gestational week of 34.5 ± 2.0 ; 16 (26.7%) neonates were term with a mean gestational week of 38.4 ± 0.8 . The mean chronological age of the neonates at which the shortened lung POCUS protocol was performed was 36.8 ± 48.9 hours. In neonates without an NRD diagnosis, the examination was performed on average at 24 hours of life. In contrast, neonates with an NRD, lung POCUS was performed with a mean at 57.3 ± 75.4 hours.

Chest X-ray and lung POCUS findings in 23 neonates with NRDs

Abnormal chest X-ray findings were found in 14 (23.3%) of 60 neonates, while 23 (38.3%) had abnormal lung POCUS findings (Table 1). Of the 23 neonates with lung POCUS abnormalities, 18 (78.3%) were preterm and 5 (21.7%) were term.

The chest X-ray and lung POCUS were normal in 34 (56.7%) of the 60 neonates. Figure 2 shows a normal chest X-ray and lung POCUS of a healthy full-term neonate at 39.5 gestational weeks and 24 hours of extrauterine life. The AP chest X-ray shows adequately expanded lungs. The lung POCUS shows a pleural line of normal thickness along with several A-lines, typical findings of a normal lung.

Nine (15.0%) neonates with an abnormal lung POCUS had a normal chest X and only 3 (5.0%) with an abnormal chest X ray had a normal lung POCUS. In 14 (23.3%) neonates, the chest X ray and the lung POCUS were abnormal. The agreement between chest X-ray and lung POCUS was $k = 0.555$ (95% CI 0.330-0.780) ($p < 0.001$). Diagnostic NRDs were interstitial fluid overload ($n = 9$, 15.0%), respiratory distress syndrome ($n = 7$, 11.6%), pneumonia ($n = 6$, 10.0%), and TTN ($n = 1$, 1.6%).

Table 2. Abnormal shortened lung POCUS findings in 23 neonates with NRDs in the NICU

Description	n (%)
Thickened pleural line	5 (21.7)
Absence of A line	17 (73.9)
Presence of B line	20 (86.9)
Consolidation	10 (43.4)
White lung	13 (56.5)
Double lung point	1 (4.3)

^aSome neonates had two or more findings. POCUS: point of care ultrasound; NRDs: neonatal respiratory disorders; NICU: neonatal intensive care unit.

Table 3. Diagnostic performance of shortened lung POCUS compared to chest X-ray as the gold standard for diagnosing NRDs in the NICU

Description	Parameter
Sensitivity, % (95% CI)	82.3 (56.6-96.2)
Specificity, % (95% CI)	79.1 (64.0-90.0)
PPV, % (95%CI)	70.7 (56.4-.81.8)
NPV, % (95% CI)	88.0 (72.1-95.4)
Accuracy, % (95% CI)	80.3 (68.0-89.5)

POCUS: point-of-care ultrasound; NRDs: neonatal respiratory disorders; NICU: neonatal intensive care unit; CI: confidence interval; PPV: positive predictive value; NPV: negative predictive value.

Abnormal lung POCUS findings in 23 neonates with NRDs

The lung POCUS findings highlight ultrasound patterns indicating respiratory impairment in more than one third of neonates, with a predominance of signs consistent with interstitial fluid overload and pneumonia, such as white lung disease ($n = 13$, 56.5%) and consolidation ($n = 10$, 43.4%). In 55 (91.7%) of 60 neonates, the lung POCUS showed a normal pleural line, and in 5 (8.3%), it was thickened (Table 2).

Figure 3 shows a male preterm neonate born at 30 weeks gestation with 24 hours of extrauterine life with NRD requiring endotracheal ventilation. The chest X-ray shows bilateral alveolar opacities. Lung POCUS of the left posterior-inferior quadrant shows a loss of normal morphology and echogenicity of the pleural line due to subpleural focal atelectasis and an increased

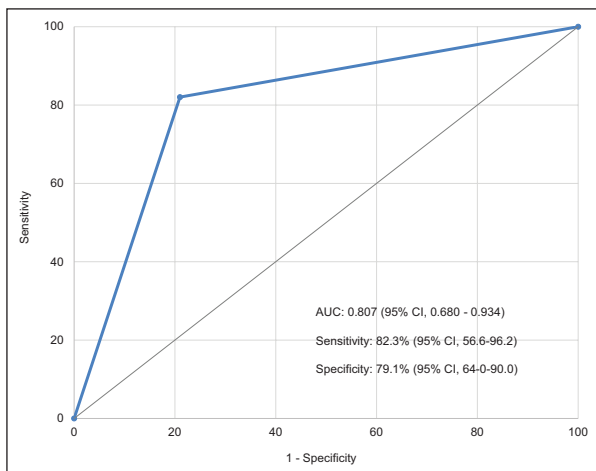


Figure 7. ROC curve showing the diagnostic performance of the shortened lung POCUS protocol in 60 neonates with NRDs. The shortened lung POCUS protocol discriminates cases with and without NRDs with a high AUC value (0.807, 95% CI 0.680-0.934).

AUC: area under the curve; NRDs: neonatal respiratory disorders; POCUS: point-of-care ultrasound; ROC: receiver operating characteristic.

Table 4. Diagnostic performance of chest X-ray compared to shortened lung POCUS as the gold standard for diagnosing NRDs in neonates in the NICU

Description	Parameter
Sensitivity, % (95% CI)	60.9 (38.5-80.3)
Specificity, % (95% CI)	91.8 (78.0-98.3)
PPV, % (95%CI)	82.1 (59.7-93.5)
NPV, % (95% CI)	79.3 (69.5-86.5)
Accuracy, % (95% CI)	80.1 (67.8-89.3)

POCUS: point-of-care ultrasound; NRDs: neonatal respiratory disorders; NICU: neonatal intensive care unit; CI: confidence interval; PPV: positive predictive value; NPV: negative predictive value.

number of B-lines forming a “white lung pattern”. The diagnosis was subpleural atelectasis on chest X-ray and lung POCUS.

Figure 4 shows a full-term neonate at 37 weeks gestation with 5 days of extrauterine life presenting an NRD and fever. The chest X-ray shows bilateral consolidation with air bronchograms, lung POCUS of the right quadrant with consolidation and a thickened pleural line. The lateral quadrant in the left hemithorax shows

focal subpleural parenchymal consolidation with air bronchogram and vascular flow in the consolidation area. Hepatization of the lung parenchyma was noted. The left posterior upper quadrant shows thickening of the pleural line and increased B-lines corresponding to a “white lung pattern”. The diagnosis was pneumonia on chest X-ray and shortened lung POCUS.

Figure 5 shows a full-term male neonate born at 38 weeks gestation with 24 hours of extrauterine life with an NRD and clinical suspicion of TTN and a normal chest X-ray. Lung POCUS of the left posterior-inferior quadrant showed an increased number of B-lines resulting in a “white lung” (wet lung pattern), along with obliteration of the A-lines, a finding consistent with interstitial fluid overload.

Figure 6 shows a preterm male neonate born at 32 weeks gestation with 24 hours of extrauterine life. A normal chest X-ray is normal. Lung POCUS of the anterior and lower right quadrant shows a focal increase in B-lines with preservation of A-lines which together form the double lung point sign. The anterior and lower left quadrant show a focal increase in B-lines with preservation of A-lines which together form the double lung point sign. TTN was the diagnosis of the shortened lung POCUS.

Diagnostic performance of lung POCUS for diagnosing NRDs compared to chest X-ray as the gold standard

The shortened lung POCUS protocol showed a sensitivity of 82.3% and a specificity of 79.1% for diagnosing NRDs in neonates in the NICU (Table 3). There were 3 false-negatives, 9 false-positives, 14 true-positives, and 34 true-negative lung POCUS results. The PPV was 70.7%, while the NPV was 88.0%. The accuracy was 80.3%. The area under the curve in the ROC was 0.807 (95% CI 0.680-0.934) (Figure 7).

Diagnostic performance of chest X-ray for diagnosing NRDs compared to lung POCUS as the gold standard

The chest X-ray showed a sensitivity of 60.9% and a specificity of 91.8% for diagnosing NRDs in neonates (Table 4). There were 9 false-negatives, 3 false-positives, 14 true-positives and 34 true-negative results on chest X-ray. The PPV was 82.1%, while the NPV was 79.3%. The accuracy was 80.1%.

DISCUSSION

The new shortened lung POCUS protocol that assesses 10 lung areas showed a higher sensitivity (82.3%) than chest X-ray (60.9%) for diagnosing NRDs in neonates in the NICU. Lung POCUS examination in neonates has the advantage of providing real-time imaging, no ionizing radiation, and can be performed at the patient's bedside. To our knowledge, this study is the first in Mexico that focuses on comparing the diagnostic performance of these two imaging modalities for NRDs in neonates.

Lung POCUS has been shown to have high accuracy in the diagnosis and follow-up of NRDs^{3,19}. In this study, the new, shortened lung POCUS protocol showed a higher sensitivity (82.3%) than chest X-ray (60.9%), while specificity was 79.1% and 91.9%, respectively. Ismail et al.³ reported the diagnostic performance of a conventional lung POCUS protocol in 100 neonates in a cross-sectional study in Egypt. The sensitivity and specificity of lung POCUS in diagnosing respiratory distress syndrome was 94.7/100%, for pneumonia, 97.5/95.0%, for meconium aspiration syndrome, 92.3/100%, for pneumothorax, 90.9/98.9% and for pulmonary atelectasis, 100/97.0%. The overall agreement between lung POCUS and chest X-ray was 98.5% (95% CI 0.88 to 0.92). Gupta et al.¹⁹ conducted a cross-sectional study in India of 244 neonates in the NICU, 77 (31.5%) had NRDs. They were examined by the conventional lung POCUS and chest X-ray. For the diagnosis of respiratory distress syndrome, the sensitivity and specificity of lung POCUS were 87.7% and 89.2%, while chest X-ray was 81.6% and 96.4%, respectively. For TTN diagnosis, the sensitivity and specificity of lung POCUS were 91.6% and 90.5%, while chest X-ray was 79.1% and 98.1%, respectively. In a prospective single-center study in Italy, Corsini et al.²⁰ examined 196 neonates in the NICU, 124 (63.3%) had respiratory distress syndrome. The agreement between chest X-ray and conventional lung POCUS was almost perfect ($k = 0.88$, 95% CI 0.81-0.94). In our study, the agreement between chest X-ray and lung POCUS was moderate ($k = 0.555$, 95% CI 0.330-0.780) ($p < 0.001$). Although our new, shortened lung POCUS protocol had better sensitivity than chest X-ray for diagnosing NRDs, it was lower than in other reports using the conventional lung POCUS protocol.

In 2004, Lichtenstein¹⁵ proposed a protocol for lung evaluation that consisted of dividing the lung into 3 segments (anterior, lateral, and posterior). Each segment is divided into superior and inferior, with 6 areas per lung (anterior-superior, anterior-inferior, superior lateral, inferior lateral, posterosuperior and posteroinferior), giving a

total of 12 in both lungs. This conventional lung ultrasound is currently used for evaluation in neonates. In 2025, Dong et al.²¹ proposed another lung POCUS protocol with 14 lung areas in which the parasternal region and adjacent to the spine were added. The study included 89 Chinese neonates with respiratory distress syndrome comparing the 12-area protocol with a 14-area protocol using chest X-ray as the gold standard. The 14-area showed higher diagnostic performance (sensitivity of 94.0% and specificity of 91.0%) than the 12-area protocol (sensitivity of 91.0% and specificity of 64.0%). Chest X-ray had a sensitivity of 88.0% and a specificity of 64.0%. This study demonstrated that more extensive protocols are better for the assessment of neonates with respiratory distress syndrome. However, the practical application of these protocols can have limitations in their implementation in NICU because neonates usually have several external auxiliary devices such as venous catheters, probes, electrodes, and ventilatory support, among others. Our shortened lung POCUS protocol examines a total of 10 anatomical areas of the chest with a reduction in the manipulation of neonates which simplifies the procedure and may be less invasive for the neonate. However, its diagnostic performance is lower than the conventional lung POCUS protocol.

The strengths of this study are related to the imaging modality, which is accessible, non-invasive, and low cost. The new, shortened lung POCUS protocol reduces neonatal manipulation and is described in detail, so it is reproducible. On the other hand, the study has limitations, such as the small sample size, the lack of clinical data, and the fact that interobserver and intraobserver agreement was not assessed.

CONCLUSION

In this study, a new shortened lung POCUS protocol showed better diagnostic performance than chest X-ray for the diagnosis of NRDs in a NICU. However, diagnostic performance was lower than the conventional lung POCUS protocol in the assessment of neonates with an NRD. Studies with larger populations using the shortened lung POCUS protocol in the NICU are needed to determine its potential role as a diagnostic tool in diagnosing NRDs.

Acknowledgments

The authors thank Professor Ana M. Contreras-Navarro for her guidance in preparing and writing this scientific paper. This original research in the Radiology Specialty

field was an awarded thesis at the Tercera Convocatoria Nacional 2024-2025, “Las Mejores Tesis de Radiología para Publicar en el JMeXFRI.”

Funding

This research received no external funding.

Conflicts of interest

The authors declare no conflicts of interest.

Ethical considerations

Protection of humans and animals. The authors declare that the procedures followed complied with the ethical standards of the responsible human experimentation committee and adhered to the World Medical Association and the Declaration of Helsinki. The procedures were approved by the institutional Ethics Committee.

Confidentiality, informed consent, and ethical approval. The authors have followed their institution’s confidentiality protocols, obtained informed consent, and received approval from the Ethics Committee. The SAGER guidelines were followed according to the nature of the study.

Declaration on the use of artificial intelligence. The authors declare that no generative artificial intelligence was used in the writing of this manuscript.

REFERENCES

- Liang HY, Liang XW, Chen ZY, Tan XH, Yang HH, Liao JY, et al. Ultrasound in neonatal lung disease. *Quant Imaging Med Surg.* 2018;8(5):535-546. doi: 10.21037/qims.2018.06.01.
- Ruoss JL, Bazaclicu C, Cacho N, De Luca D. Lung Ultrasound in the Neonatal Intensive Care Unit: Does It Impact Clinical Care? *Children (Basel).* 2021;8(12):1098. doi: 10.3390/children8121098.
- Ismail R, El Raggal NM, Hegazy LA, Sakr HM, Eldafrawy OA, Farid YA. Lung Ultrasound Role in Diagnosis of Neonatal Respiratory Disorders: A Prospective Cross-Sectional Study. *Children (Basel).* 2023;10(1):173. doi: 10.3390/children10010173.
- Gao YQ, Qiu RX, Liu J, Zhang L, Ren XL, Qin SJ. Lung ultrasound completely replaced chest X-ray for diagnosing neonatal lung diseases: a 3-year clinical practice report from a neonatal intensive care unit in China. *J Matern Fetal Neonatal Med.* 2022;35(18):3565-3572. doi: 10.1080/14767058.2020.1830369.
- Raimondi F, Yousef N, Rodriguez Fanjul J, De Luca D, Corsini I, Shankar-Aguilera S, et al. A Multicenter Lung Ultrasound Study on Transient Tachypnea of the Neonate. *Neonatology.* 2019;115(3):263-268. doi: 10.1159/000495911.
- Marini TJ, Rubens DJ, Zhao YT, Weis J, O'Connor TP, Novak WH, et al. Lung Ultrasound: The Essentials. *Radiol Cardiothorac Imaging.* 2021;3(2):e200564. doi: 10.1148/ryct.2021200564.
- El-Masry H, Aladawy M, Mansor T, Abo El Magd H. Comparative Study between Chest X-Ray and Lung Ultrasound in Neonatal Respiratory Distress. *Ann Neonatal J.* 2021;3(1):125-143. doi: 10.21608/anj.2021.137638.
- Łyżniak P, Świętoń D, Serafin Z, Szurowska E. Lung ultrasound in a nutshell. Lines, signs, some applications, and misconceptions from a radiologist's point of view. *Pol J Radiol.* 2023;88:e294-e310. doi: 10.5114/pjr.2023.128866.
- Liu J, Guo G, Kurepa D, Volpicelli G, Sorantin E, Lovrenski J, et al. Specification and guideline for technical aspects and scanning parameter settings of neonatal lung ultrasound examination. *J Matern Fetal Neonatal Med.* 2022;35(5):1003-1016. doi: 10.1080/14767058.2021.1940943.
- Khattab M, Hagan J, Staib LH, Mustafa A, Goodman TR. Cumulative diagnostic imaging radiation exposure in premature neonates. *J Neonatal Perinatal Med.* 2022;15(1):95-103. doi: 10.3233/NPM-210726.
- Srinivasan S, Aggarwal N, Makhai S, Jhobta A, Kapila S, Bhoil R. Role of lung ultrasound in diagnosing and differentiating transient tachypnea of the newborn and respiratory distress syndrome in preterm neonates. *J Ultrason.* 2022;22(88):e1-e5. doi: 10.15557/JoU.2022.0001.
- Liu J, Liu F, Liu Y, Wang HW, Feng ZC. Lung ultrasonography for the diagnosis of severe neonatal pneumonia. *Chest.* 2014;146(2):383-388. doi: 10.1378/chest.13-2852.
- Raimondi F, Yousef N, Migliaro F, Capasso L, De Luca D. Point-of-care lung ultrasound in neonatology: classification into descriptive and functional applications. *Pediatr Res.* 2021;90(3):524-531. doi: 10.1038/s41390-018-0114-9.
- Wang J, Wei H, Chen H, Wan K, Mao R, Xiao P, et al. Application of ultrasonography in neonatal lung disease: An updated review. *Front Pediatr.* 2022;10:1020437. doi: 10.3389/fped.2022.1020437.
- Lichtenstein D. Lung ultrasound in the critically ill. *Clin Intensive Care.* 2005;16(2):79-87. doi: 10.1080/09563070500131027.
- Perri A, Riccardi R, Iannotta R, Di Molfetta DV, Arena R, Vento G, et al. Lung ultrasonography score versus chest X-ray score to predict surfactant administration in newborns with respiratory distress syndrome. *Pediatr Pulmonol.* 2018;53(9):1231-1236. doi: 10.1002/ppul.24076.
- Liu J, Lovrenski J, Ye Hlaing A, Kurepa D. Neonatal lung diseases: lung ultrasound or chest x-ray. *J Matern Fetal Neonatal Med.* 2021;34(7):1177-1182. doi: 10.1080/14767058.2019.1623198.
- Wang Y, Li N, Qu Y. Diagnostic accuracy of lung ultrasound for transient tachypnea: a meta-analysis. *J Pediatr.* 2022;98(4):329-337. doi: 10.1016/j.jpeds.2021.10.003.
- Gupta V, Panigraphy N, Venkateshkhmi A, Chirra DK, Pandita A. Diagnostic ability of bedside lung Ultrasound in neonates with respiratory distress. *J Pediatr Neonatal Care.* 2018;8(6):308-312. doi: 10.15406/jpnc.2018.08.00364.
- Corsini I, Parri N, Gozzini E, Coviello C, Leonardi V, Poggi C, et al. Lung Ultrasound for the Differential Diagnosis of Respiratory Distress in Neonates. *Neonatology.* 2019;115(1):77-84. doi: 10.1159/000493001.
- Dong J, Deng Y, Tong J, Du T, Liu W, Guo Y. The diagnostic value and efficacy evaluation of lung ultrasound score in neonatal respiratory distress syndrome: a prospective observational study. *Front Pediatr.* 2025;13:1500500. doi: 10.3389/fped.2025.1500500.

Prevalence of dolichoarteriopathies of the extracranial internal carotid artery by neck CTA in Mexican patients

Diana Camorlinga-Ornelas^{1,2*}, Samuel Guillen-Ortega^{1,2}, and Hilda Sarmiento-Martinez¹

¹Department of Radiology, High Specialty Medical Unit 71, Mexican Social Security Institute; ²School of Medicine, Autonomous University of Coahuila; Torreon, Coahuila, Mexico

ABSTRACT

Introduction: Dolichoarteriopathies of the extracranial internal carotid artery (EICA) are anatomical variants of the arterial course associated with alterations in the geometry and tortuosity of the vessel course. The reported prevalence varies widely, ranging from 10% to 70% in different studies. This study aimed to determine the prevalence of EICA dolichoarteriopathy types and subtypes in Mexican patients using neck computed tomography angiography (CTA). **Material and methods:** This cross-sectional study was conducted in patients who underwent neck CTA scans based on the referring physician's clinical indication. An EICA dolichoarteriopathy variant was determined by reviewing CTA images in the axial, coronal, and sagittal planes. Laterality, type of dolichoarteriopathy (tortuosity, coiling, or kinking), and the kinking subtype were defined. **Results:** Two hundred seventy-one patients, 136 (50.2%) women and 135 (49.8%) men, were included. EICA dolichoarteriopathies were found in 151 of 271 patients with a prevalence of 55.7%. Dolichoarteriopathies were more common in older patients ($p < 0.001$). More than one type or subtype of EICA dolichoarteriopathies was found. Thus, 275 variants were found in 151 patients, with a comparable distribution on the right and left sides. Tortuosity was the most common type ($n = 198$, 72.0%), followed by kinking ($n = 41$, 14.9%) and coiling ($n = 36$, 13.1%). The subtypes were kinking A, 5.1% ($n = 14$), kinking B, 7.7% ($n = 21$), and kinking C, 2.2% ($n = 6$). **Conclusion:** We found a high prevalence (55.7%) of EICA dolichoarteriopathies. These were more frequent in older Mexican patients, and tortuosity was the most common. This study is the first to investigate the prevalence of types and subtypes of EICA dolichoarteriopathies in Mexican patients using neck CT.

Keywords: Head and neck. Anatomy. Internal carotid artery. Prevalence study. Vascular diseases. Helical computed tomography.

INTRODUCTION

Dolichoarteriopathies of the extracranial internal carotid artery (EICA) are morphologic arterial course variations associated with changes in the geometry and twisting of the vessel^{1,2}. The term originates from the Greek words “*dolichos*,” meaning “abnormally long,” and “*ektasis*,” meaning “distention” or “dilatation.” They were first described by Kelly in 1925³. Despite their clinical

importance as a non-atherosclerotic factor contributing to reduced cerebral blood flow, these changes have not been fully studied¹. This importance stems from the crucial role the internal carotid arteries play in supplying oxygenated blood to the brain^{4,5}.

Although EICA dolichoarteriopathies can be asymptomatic, some are associated with reduced cerebral blood flow, particularly when accompanied by atherosclerotic plaques^{5,6}. Patients can present symptoms

*Corresponding author:

Diana Camorlinga-Ornelas
E-mail: dra.camorlinga@gmail.com

Received for publication: 08-12-2024

Accepted for publication: 17-02-2025

DOI: 10.24875/JMEXFRI.M25000102

Available online: 15-07-2025

J Mex Fed Radiol Imaging. 2025;4(2):94-101

www.JMeXFRI.com

2696-8444 / © 2025 Federación Mexicana de Radiología e Imagen, A.C. Published by Permanyer. This is an open access article under the CC BY-NC-ND (<https://creativecommons.org/licenses/by-nc-nd/4.0/>).

Table 1. Characteristics of 271 Mexican patients and prevalence of EICA dolichoarteriopathies identified by neck CTA

Characteristic	n = 271
Sex	
Women, n (%)	136 (50.2%)
Men, n (%)	135 (49.8%)
Age, years, mean ± SD	
Age groups, years	
0-16, n (%)	36 (13.3)
17-59, n (%)	159 (58.7)
60 and older, n (%)	76 (28.0)
EICA dolichoarteriopathy	
Yes, n (%)	151 (55.7)
No, n (%)	120 (44.3)

EICA: extracranial internal carotid artery; CTA: computed tomography angiography; SD: standard deviation.

Table 2. Association between age and EICA dolichoarteriopathies by neck CTA in Mexican patients

Description	Total	Dolichoarteriopathy		p
		Yes	No	
n	271	151	120	
Age group				< 0.001 ^a
0-16 years, n (%)	36 (13.3)	12 (7.9)	24 (20.0)	
17-59 years, n (%)	159 (58.7)	86 (57.0)	73 (60.8)	
60 years and older, n (%)	76 (28.0)	53 (35.1)	23 (19.2)	

^aOlder age was significantly associated with EICA dolichoarteriopathies. EICA: extracranial internal carotid artery; CTA: computed tomography angiography.

such as hypoglossal nerve compression, decreased cognitive abilities, neuropsychological developmental delays, focal or generalized seizures, transient ischemic attacks (TIAs), hemiparesis, amaurosis fugax, and ischemic vascular events^{6,7,8}. Dolichoarteriopathies are also associated with ischemic complications and vascular injury during surgical procedures¹. Metz et al.⁹ classified EICA dolichoarteriopathies into three types: tortuosity, coiling, and kinking. Tortuosity refers to the elongation and curvature of the arteries, typically in a C or S shape. Coiling refers to elongation that forms

exaggerated shapes such as a C, U, or S, or circular configurations with a 360° twist. Kinking refers to an acute angulation of the artery, typically less than 90°^{5,7,9-11}. The kinking severity correlates with cerebral blood flow reduction and is categorized according to the degree of EICA angulation: Grade I, also known as mild or Grade A (61-90°), with a minimal hemodynamic impact; Grade II, also known as moderate or Grade B (31-60°), which reduces blood flow by 40%, and Grade III, also known as severe or grade C kinking ($\leq 30^\circ$), which results in a 60% reduction and an increased risk of ischemic complications⁷.

EICA dolichoarteriopathies are identified with imaging techniques such as neck ultrasound, digital subtraction angiography, magnetic resonance imaging (MRI), and computed tomography angiography (CTA)⁷. The latter has the advantage of accessibility, allowing rapid acquisition and providing excellent anatomical images, especially with volume rendering (VR). It allows a 360° assessment, contributing to better classifying the different types, and facilitating angle measurement. Unlike ultrasound, it is not influenced by neck width or length¹². Although EICA dolichoarteriopathies are thought to be common in the general population, their prevalence varies from 10% to 70% in different studies^{5,12,13}. While kinking is often considered the most common type⁷, its occurrence is estimated at 5-25%². However, recent studies suggest that tortuosity is more common². No study has determined the prevalence and distribution of EICA dolichoarteriopathies in the Mexican population. This study determined the prevalence, types, and subtypes of EICA dolichoarteriopathies in Mexican patients using neck CTA.

MATERIAL AND METHODS

This cross-sectional study was conducted between August 2021 and August 2024 at the Department of Radiology, High Specialty Medical Unit No. 71 in Torreon, Coahuila, Mexico. Patients of both sexes, aged 0 to 99, who underwent neck CTA based on the clinical indication of their referring physician were included. Exclusion criteria were patients with carotid stents or changes due to endarterectomy, no available neck CTA reports in PACS (Picture Archiving and Communication System), and studies with incomplete data. Elimination criteria were studies that showed head rotation, flexion, or extension relative to the neck, neck CTA scans that did not fully cover the region of interest, and CTA scans with artifacts that prevented

Table 3. EICA dolichoarteriopathies laterality, types, and subtypes in 151 Mexican patients by neck CTA

Description	n = 275 ^a
EICA dolichoarteriopathy ^b	
Right, n (%)	132 (48.0%)
Left, n (%)	143 (52.0%)
Type	
Tortuosity, n (%)	198 (72.0)
Coiling, n (%)	36 (13.1)
Kinking, subtypes, n (%)	41 (14.9)
Kinking A	14 (5.1)
Kinking B	21 (7.7)
Kinking C	6 (2.2)

^aTotal number of anatomical variants found in the 151 patients with EICA dolichoarteriopathies; ^bBilateral involvement was found in 203 (73.8%) of 275 variants, as some patients had more than one type or subtype of EICA dolichoarteriopathy. EICA: extracranial internal carotid artery; CTA: computed tomography angiography.

Table 4. EICA dolichoarteriopathy laterality diagnosed by neck CTA concerning type and subtype

Description	Total n = 275	Laterality		p
		Right n = 132	Left n = 143	
Tortuosity, n (%)	198 (72.0)	98 (49.5)	100 (50.5)	0.368
Coiling, n (%)	36 (13.1)	12 (33.3)	24 (66.7)	0.062
Kinking, subtypes, n (%)	41 (14.9)	22 (46.8)	19 (53.2)	0.416
Kinking A	14 (5.1)	8 (57.1)	6 (42.9)	0.473
Kinking B	21 (7.7)	11 (52.4)	10 (47.6)	0.663
Kinking C	6 (2.2)	3 (50.0)	3 (50.0)	0.914

EICA: extracranial internal carotid artery; CTA: computed tomography angiography.

correct image interpretation. Informed consent was not required because the data were collected as part of routine medical care. The institutional research and research ethics committees approved the study.

Study description and variables

Variables included sex, age, presence of an EICA dolichoarteriopathy, laterality, type (tortuosity, coiling, and kinking), and kinking subtype according to Metz classification⁹: an angulation of 90-60° defines subtype A (mild or grade I); an angulation of 60-30° subtype B

(moderate or grade II), and an angulation less than 30° subtype C (severe or grade III). The age groups were 0-16, 17-59, and 60 years and older.

Image acquisition and analysis

Neck CTA scans were performed with a GE Revolution™ EVO CT scanner (GE HealthCare Co., Waukesha, WI, USA) with the head in a neutral position (no flexion, extension, or rotation). CTAs were evaluated by a radiologist (HSM) with 15 years of experience and two radiology trainees (DCO and SGO). The EICA dolichoarteriopathy variant was identified by reviewing arterial phase images in the axial, coronal, and sagittal planes. The degree of kinking was measured by delineating parallel lines along the long axes of the proximal and distal segments of the EICA, with the angle of intersection corresponding to the measurement. If there was uncertainty regarding the type or subtype, VR reconstructions were performed. The baseline examination was used in patients with multiple CTA examinations.

Statistical analysis

The sample size was estimated based on the assumption that the prevalence of dolichoarteriopathies in the population is 30%^{5,13}. Using the formula for estimating the expected proportion in a known population (1,644 neck CTA examinations), the sample size was 271 individuals with a confidence level of 95% and a margin of error of 5%. Results are presented using measures of central tendency and dispersion for quantitative variables and absolute frequency counts and corresponding percentages for categorical variables. Differences in proportions between categorical variables were assessed using the chi-square test. A $p < 0.05$ was considered statistically significant. SPSS version 24 (IBM Corp., Armonk, NY, USA) was used for the statistical analysis.

RESULTS

Two hundred seventy-one patients who underwent neck CTA were screened for EICA dolichoarteriopathies (Table 1); 50.2% (n = 136) were women and 49.8% (n = 135) were men with an age range of 8 months to 86 years; 13.3% (n = 36) were 0 to 16, 58.7% (n = 159) were between 17 and 59, and 28.0% (n = 76) were 60 years or older. EICA dolichoarteriopathies were found in 151 of 271 patients with a prevalence of 55.7%.

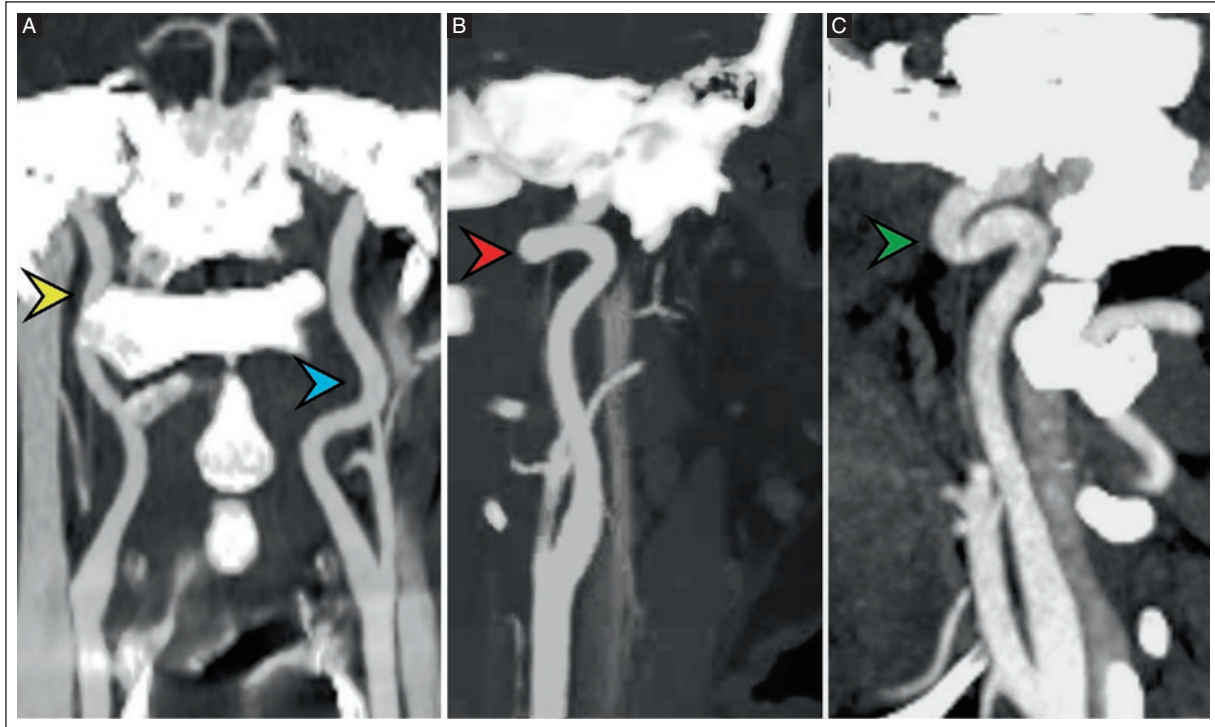


Figure 1. Neck CTA examinations showing different EICA dolichoarteriopathy types. **A:** coronal neck CTA reconstruction from a 41-year-old man showing tortuosity type in the right (yellow arrowhead) and left (blue arrowhead) EICA. **B:** coronal-oblique CTA reconstruction from a 23-year-old man with coiling type of the left EICA (red arrowhead). **C:** a sagittal CTA reconstruction from a 47-year-old woman showing kinking type of the left EICA (green arrowhead).

CTA: computed tomography angiography; EICA: extracranial internal carotid artery.

Association between age and EICA dolichoarteriopathies detected by neck CTA in Mexican patients

Significant differences were found regarding age. EICA dolichoarteriopathies were more frequent in older age groups (Table 2). In the 0-16 age group, 12 (7.9%) of 36 patients had an EICA dolichoarteriopathy, while 24 (20%) did not. In the 17-59 age group, 86 (57.0%) had an EICA dolichoarteriopathy, while 73 (60.8%) did not. In the 60 years and older group, 53 (35.1%) had an EICA dolichoarteriopathy, while 23 (19.2%) did not ($p < 0.001$).

EICA dolichoarteriopathy laterality, types, and subtypes by neck CTA

The anatomical variant distribution was analyzed (Table 3). A total of 275 variants were found in 151 patients, with a similar distribution observed on both sides. One hundred and thirty-two (48.0%) of 275 were right-sided and 143 (52.0%) were left-sided, with no significant difference in laterality. In addition, 203 (73.8%)

of 275 variants were bilateral, with more than one type or subtype of EICA found in some patients. The most common type was tortuosity with 72.0% ($n = 198$) of the 275 variants; 13.1% ($n = 36$) were coilings, and 14.9% ($n = 41$) were kinkings. The kinking subtypes were kinking A, 5.1% ($n = 14$), kinking B, 7.7% ($n = 21$), and kinking C, 2.2% ($n = 6$). Figures 1 and 2 show the neck CTA examinations of the three EICA dolichoarteriopathy types. Figures 3, 4, and 5 show the A, B, and C kinking subtypes.

EICA dolichoarteriopathy laterality according to type and subtype by neck CTA

EICA dolichoarteriopathy laterality was analyzed by type and subtype (Table 4). The prevalence of tortuosity was comparable on the right and left sides, while coiling and kinking were slightly more common on the left side ($n = 24$, 66.7% and $n = 19$, 53.2%, respectively) than on the right side ($n = 12$, 33.3% and $n = 22$, 46.8%, respectively). In contrast, the kinking subtypes A and B

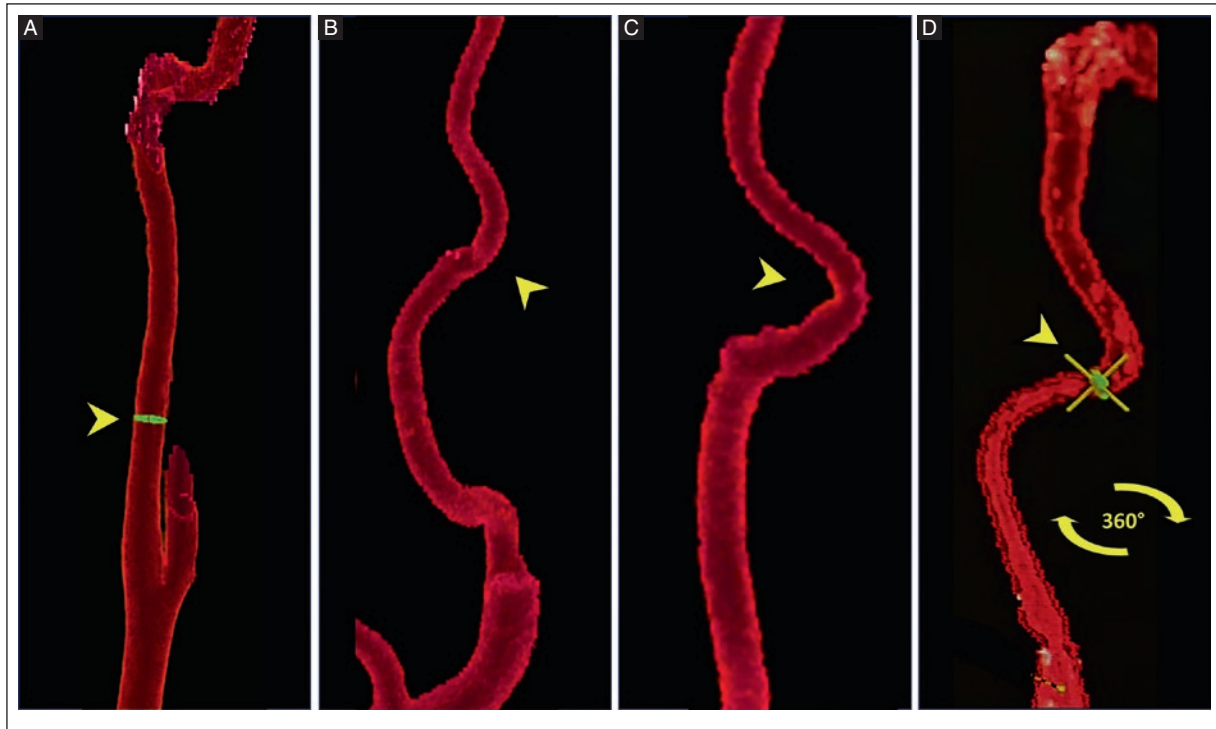


Figure 2. Frontal views of neck CTA VR reconstructions showing different EICA dolichoarteriopathy types. **A:** the right EICA of a 23-year-old man shows no dolichoarteriopathy (arrowhead). **B:** tortuosity type in the left EICA and **C:** kinking type in the right EICA of a 78-year-old woman (arrowheads). **D:** coiling type in the right EICA (arrowhead) of an 83-year-old woman with the vessel rotating 360° around its axis, characteristic of this morphology.

EICA: extracranial internal carotid artery; CTA: computed tomography angiography; VR: volume rendering.

were more common on the right side ($n = 8$, 57.1% and $n = 11$, 52.4%, respectively) than on the left ($n = 6$, 42.9% and $n = 10$, 47.6%, respectively). The differences in laterality between the different EICA dolichoarteriopathy types and subtypes were not significant. Kinking subtype C occurred equally on both sides.

DISCUSSION

This study showed a high prevalence (55.7%) of EICA dolichoarteriopathies on neck CTA examination, with older patients being more frequently affected than younger ones, and tortuosity type being more frequent. To our knowledge, this study is the first in Mexico to determine the prevalence and distribution of types and subtypes of vascular variants of EICA dolichoarteriopathies.

Previous studies have shown that EICA dolichoarteriopathies are common in the general population. However, their prevalence varies from series to series. Pellegrino et al.¹³ reported a prevalence of 25.9% in 1220 Italians aged 25 to 89 using color Doppler US. Di Pino et al.⁵ observed a variable frequency between

10% and 45% in a cohort of 2856 Italians aged 0 to 96. They also studied patients with color Doppler US. In contrast, Barfzadeh et al.¹² reported a higher prevalence of 70.3% in 106 Iranian patients examined by neck CTA. In our study, the prevalence of EICA dolichoarteriopathies in 271 Mexican patients was 55.7% ($n = 151$), exceeding the prevalence in the Italian population but lower than in the Iranian population. No significant difference was found in the frequency of dolichoarteriopathies by sex, unlike the Italian population, where most variants were found in women over 60 years of age—a finding they attributed to possible hormonal factors¹⁴. Moreover, no preference for one side was found among types and subtypes, unlike Sacco et al.¹⁴ who found more variants in the left arteries (61.5%) than in the right arteries (38.5%). The prevalence of EICA dolichoarteriopathies by neck CTA in our study was higher than in some international studies. This finding could be due to differences in imaging techniques or population characteristics.

Regarding age, previous reports by Metz et al.⁹ and Barfzadeh et al.¹² found an association between

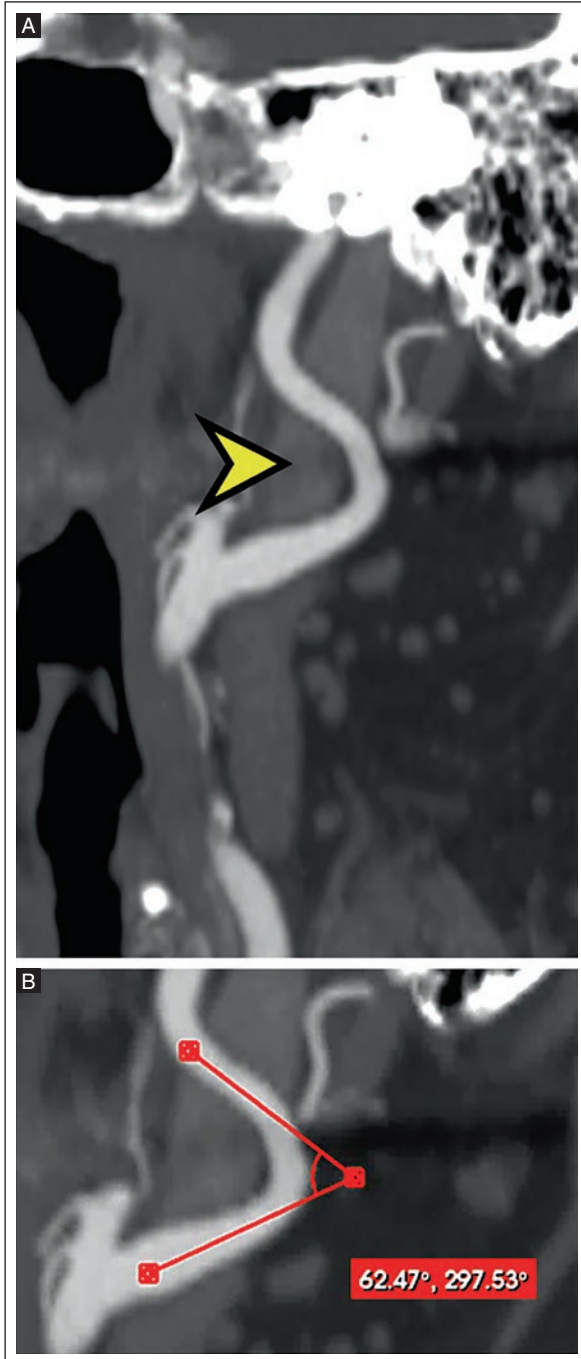


Figure 3. **A:** reconstruction of a neck CTA in the sagittal plane from a 74-year-old woman patient with kinking subtype A of EICA dolichoarteriopathy showing an angle less than 90° but more than 60° (arrowhead). **B:** magnified view with a measured angle of 62 degrees, classified as a grade I kinking subtype.

CTA: computed tomography angiography; EICA: extracranial internal carotid artery.

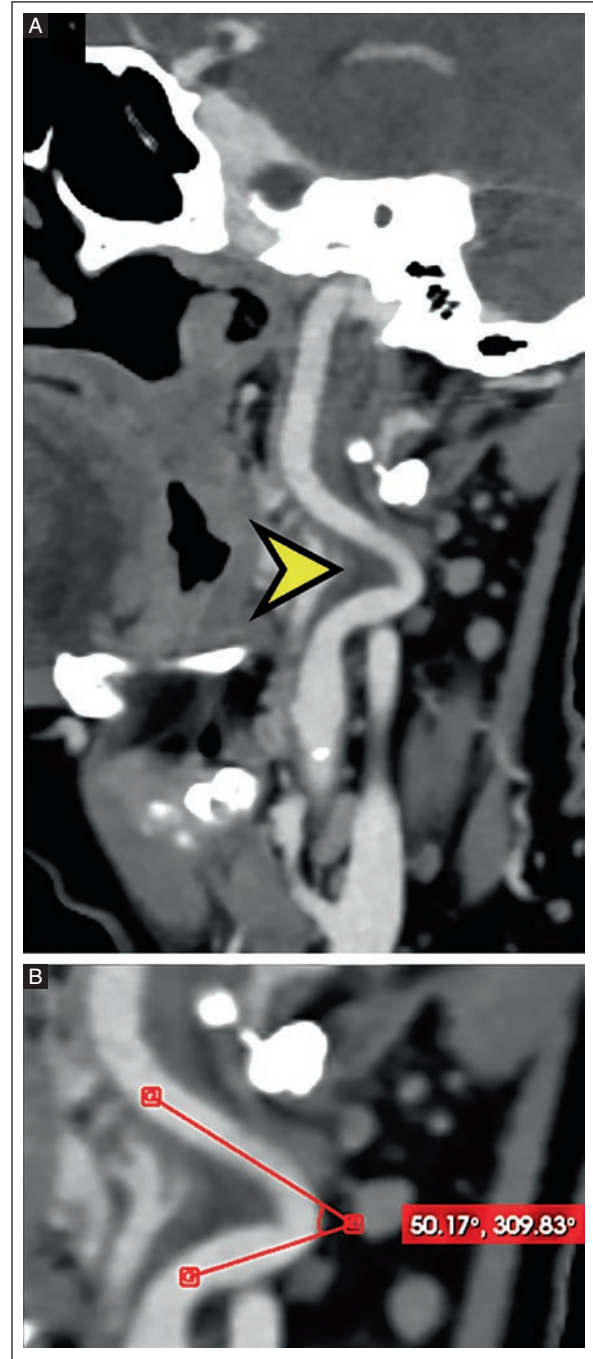


Figure 4. **A:** reconstruction in the sagittal plane of a neck CTA in a 64-year-old woman with grade II kinking of the EICA, a subtype of dolichoarteriopathy defined by an angulation between 30° and 60° (arrowhead). **B:** a magnified view with an angle measurement of 50 degrees, classified as a grade II kinking subtype.

CTA: computed tomography angiography; EICA: extracranial internal carotid artery.

advancing age and increased arterial elongation and tortuosity. Our study showed a significant association between advanced age and EICA dolichoarteriopathies

($p = 0.001$), which is consistent with the literature, where there is a significant association of these variants with advanced age¹⁴, supporting the idea that



Figure 5. A: sagittal plane reconstruction of a neck CTA in a 63-year-old woman showing severe or grade III kinking of the EICA, a subtype of dolichoarteriopathy defined by an angulation less than 30° (arrowhead). **B:** magnified view showing a 25-degree angle, classified as a grade III kinking subtype.

CTA: computed tomography angiography; EICA: extracranial internal carotid artery.

arterial elasticity, and degenerative changes in the vessel wall over time¹⁴. EICA dolichoarteriopathies have also been observed in the 0-16 age group, suggesting that there may be a congenital abnormality that resolves with somatic growth and re-emerges with age due to vascular remodeling.

The classification of EICA dolichoarteriopathy types is consistent across studies; however, the reported frequencies vary considerably. In our study, tortuosity was the most frequent type of EICA dolichoarteriopathy, accounting for 72.0% (n = 198) of the 275 variants, followed by kinking (n = 41, 14.9%) and coiling (n = 36, 13.1%). This distribution differs from previous literature. For example, in a study of 1217 Italian patients examined by ultrasound, Sacco et al.¹⁴ identified 437 affected arteries, with kinking being the most common variant (54.0%), followed by tortuosity (44.6%) and coiling (1.4%). Such discrepancies may be due to differences in imaging modalities or methodological approaches. Distinguishing whether frequencies were analyzed per number of patients or affected vessels is crucial for accurate interpretation and comparison. This distinction was taken into account in our study design.

Kinking is classified into three subtypes. The frequency of each subtype is reported differently in the literature. For example, Metz et al.⁹ reported an incidence of kinking and its subtypes studied by angiography in 1,000 British patients. They found that among all cases of kinking (16%), type A was the most common with 6.6% of all dolichoarteriopathy cases, followed by type C (6%) and type B (2.5%). Our study showed a similar overall prevalence of kinking of 15.0%, with type B being the most common. As the definitions of kinking subtypes are consistent across studies, these differences could reflect anatomic variability between populations or the influence of imaging techniques on the identification of kinking patterns. Our results challenge the assumption that type A is the predominant subtype and emphasize the need to include additional variables in dolichoarteriopathy assessments to improve understanding of these vascular variants.

One of the strengths of our study is the sample size, which was determined using statistical methods to ensure a representative population. In addition, CTA provides high-resolution imaging that precisely identifies vascular abnormalities. However, some limitations need to be considered. First, selection bias may have occurred because this was a retrospective study. Also, our data were obtained from a single medical center, and clinical findings were not recorded.

older individuals are at greater risk of these vascular abnormalities. The proposed underlying mechanism is related to progressive vascular remodeling, loss of

CONCLUSION

Our study showed a high prevalence (55.7%) of EICA dolichoarteriopathies in Mexican patients evaluated with neck CTA, with a significant association with older age groups, and tortuosity being the most common type. These findings underscore the need for investigation of vascular abnormalities, especially in older adults. Further studies are needed to evaluate EICA dolichoarteriopathy-associated clinical symptoms in a larger population, particularly in older adults.

Acknowledgments

The authors thank Professor Ana M. Contreras-Navarro for her guidance in preparing and writing this scientific paper. This original research in the Radiology Specialty field was an awarded thesis at the Tercera Convocatoria Nacional 2024-2025 "Las Mejores Tesis para Publicar en el JMeXFRI".

Funding

This research received no external funding.

Conflicts of interest

The authors declare that they have no conflicts of interest.

Ethical considerations

Protection of humans and animals. The authors declare that the procedures followed complied with the ethical standards of the responsible human experimentation committee and adhered to the World Medical Association and the Declaration of Helsinki. The procedures were approved by the institutional Ethics Committee.

Confidentiality, informed consent, and ethical approval. The authors have followed their institution's

confidentiality protocols. Informed consent was not required for this observational study of information collected during routine clinical care.

Declaration on the use of artificial intelligence. The authors declare that no generative artificial intelligence was used in the writing of this manuscript.

REFERENCES

- Lomini P. Dolicoarteriopatías carotídeas: un enfoque global. *Rev Argent Cardiol.* 2024;92(3):10-20. doi:10.7775/rac.es.v92.i3.XXXXX.
- Beigelman R, Izaguirre A, Milei J. Are kinking and coiling of carotid artery congenital or acquired? *Angiology.* 2009;61(1):107-112. doi: 10.1177/0003319709335790.
- Kelly A. Tortuosity of the internal carotid in relation to the pharynx. *J Laryngol Otol.* 1925;40(5):251-260.
- Charlick M, Das JM. *Anatomy, Head and Neck: Internal Carotid Arteries.* In: StatPearls [Internet]. Treasure Island (FL): StatPearls Publishing; 2025 [cited 2025 Feb 4]. Available from: <https://www.ncbi.nlm.nih.gov/books/NBK556061/>.
- Di Pino L, Franchina A, Costa S, Gangi S, Strano F, Ragusa M, et al. Prevalence and morphological changes of carotid kinking and coiling in growth: an echo-color Doppler study of 2856 subjects aged 0 to 96 years. *Int J Cardiovasc Imaging.* 2021;37(2):479-484. doi: 10.1007/s10554-020-02047-0.
- Beigelman R, Izaguirre A, Azzato F, Milei J. Carotid artery pathology, plaque structure: relationship between histological assessment, color Doppler ultrasonography and magnetic resonance imaging - dolichoarteriopathies - baroreceptors. In: Milei J, Ambrosio G, editors. *Carotid Artery Disease - From Bench to Bedside and Beyond.* London: IntechOpen; 2014. p. 31-83.
- Yu J. Current understanding of dolichoarteriopathies of the internal carotid artery: a review. *Int J Med Sci.* 2017;14(8):772-784. doi: 10.7150/ijms.19229.
- Takkar A, Khurana D, Khandelwal N. Kinked carotids: The "python" in neck. *Ann Indian Acad Neurol.* 2016;19(3):409-410. doi: 10.4103/0972-2327.181488.
- Metz H, Murray L, Bannister R, Bull J, Marshall J. Kinking of the internal carotid artery. *Lancet.* 1961; 1 (7174): 424-426. doi:10.1016/s0140-6736(61)90004-6.
- Weibel J, Fields W. Tortuosity, coiling and kinking of the internal carotid artery. Etiology and radiographic anatomy. *Neurology.* 1965; 15: 7-18. doi:10.1212/wnl.15.1.7.
- Quijano Y, García D. Variantes Anatómicas Del Círculo Arterial Cerebral En Un Anfiteatro Universitario en Bogotá (Colombia). *Rev Ciencias Salud (Spanish).* 2020; 18 (3): 01-08 doi:10.12804/revistas.urosario.edu.co/revsalud/a.9688.
- Barfzadeh A, Saba M, Pourzand P, Jalalif MR, Alizadeh SD, Mirkamali H, et al. Anatomical variations of the extracranial internal carotid artery: prevalence, risk factors, and imaging insights from CT-angiography. *Surg Radiol Anat.* 2024;46(8):1295-1299. doi:10.1007/s00276-024-03425-7.
- Pellegrino L, Prencipe G, Vairo F. Dolicho-arteriopathies (kinking, coiling, tortuosity) of the carotid arteries: study by color Doppler ultrasonography. *Minerva Cardioangiol (Italian).* 1998;46(3):69-76.
- Sacco S. Morphological Variations of the Internal Carotid Artery: Prevalence, Characteristics and Association with Cerebrovascular Disease. *Int J Angiol.* 2007;16(2):59-61. doi: 10.1055/s-0031-1278249.

Comparison of mammography breast density assessment by radiologists and Quantra artificial intelligence in women with and without breast implants: intra and interobserver agreement

Beatriz E. Gonzalez-Ulloa*, Claudia B. Corona-Gonzalez, and Rosa L. Molina-Gutierrez

Breast Imaging Department, Centro de Diagnostico Especializado por Imagen, Zapopan, Jalisco, Mexico

ABSTRACT

Introduction: Visual methods for assessing mammographic breast density (MBD) have variable reproducibility in women with dense breasts and/or implants. Assessment of MBD by artificial intelligence (AI) and radiologists (human readers, HRs) has been reported. This study compared the intraobserver agreement of HRs and the interobserver agreement of Quantra AI software and HRs in MBD assessment in women with and without breast implants. **Material and methods:** HRs and AI Quantra 2.2.2 assessed MBD in 2D mammograms and tomosynthesis of women over 35 years of age in two phases. Four (a, b, c, d) and two (a+b, non-dense and c+d, dense) MBD categories of the Breast Imaging Reporting and Data System (BI-RADS) were used. Intra and interobserver agreement was assessed with light and Cohen's kappa. **Results:** 4-HRs evaluated 678 mammograms in each phase: 548 without implants and 130 with implants. 4-HRs intraobserver agreement was substantial to almost perfect in women without implants in the two MBD categories. For women with implants, intraobserver agreement was moderate to substantial in the four and two MBD categories. In women without implants, interobserver agreement between AI Quantra and 4-HRs was moderate to substantial for the two MBD categories, while in women with implants, interobserver agreement was slight to fair for the four and two MBD categories. **Conclusion:** Intraobserver agreement for the 4-HRs was better in women without implants in the two MBD categories and acceptable in women with implants. The interobserver agreement between AI Quantra and 4-HRs was acceptable for the two MBD categories in women without implants, while in women with implants, the interobserver agreement between AI Quantra and 4-HRs was unacceptable for the four and two MBD categories. This is the first report on the comparison of AI Quantra and HRs in the assessment of MBD in women with and without breast implants.

Keywords: Mammography breast density. Breast implants. Artificial intelligence. Human readers. Quantra software.

INTRODUCTION

Mammography sensitivity decreases in women with dense breasts and breast implants¹⁻³. Radiologists use visual methods to assess mammographic breast density (MBD). The most common is the Breast Imaging Reporting and Data System (BI-RADS)^{4,5}. However, visual techniques are subjective, and their variability

reduces reproducibility⁶. Artificial intelligence (AI) has been compared to radiologists (human readers, HRs) in the MBD assessment⁷⁻¹⁵. Several AI software have been approved by the Food and Drug Administration (FDA)¹². One of these is AI Quantra v.2.2.2 (Hologic Inc.) which quantifies the densest area based on BI-RADS 5th Edition^{4,5}.

*Corresponding author:

Beatriz E. Gonzalez-Ulloa
E-mail: betyglez@yahoo.com

Received for publication: 08-01-2025

Accepted for publication: 27-02-2025

DOI: 10.24875/JMEXFRI.M25000103

Available online: 15-07-2025

J Mex Fed Radiol Imaging. 2025;4(2):102-111

www.JMeXFRI.com

2696-8444 / © 2025 Federación Mexicana de Radiología e Imagen, A.C. Published by Permanyer. This is an open access article under the CC BY-NC-ND (<https://creativecommons.org/licenses/by-nc-nd/4.0/>).

The AI software assesses MBD in women with breast implants in different ways. Some assess MBD in the displaced mediolateral oblique (MLO) and craniocaudal (CC) views¹⁶; others in the normal MLO and CC views¹⁷. There are no clinical data comparing the reproducibility of MBD assessment in women with and without breast implants. This study compared the intraobserver agreement of HRs and the interobserver agreement between AI Quantra v2.2.2 and HRs in MBD assessment in women with and without breast implants.

MATERIAL AND METHODS

This prospective cohort study was conducted from May 2 to June 30, 2022, in the Breast Imaging Department of the Centro de Diagnostico Especializado por Imagen in Zapopan, Jalisco, Mexico with a convenience sample of radiologists with training in breast imaging. They had current certification from the Mexican Council of Radiology and Imaging, and informed consent was obtained from the radiologists.

Study development and variables

Screening or diagnostic mammograms of women 35 years or older with and without breast implants were analyzed in phases 1 and 2 from a previously published study¹⁸. MBD was assessed in four (a, b, c, d) and two (a+b, non-dense and c+d, dense) categories based on the American College of Radiology BI-RADS 5th Edition. Sex and years of experience as a radiologist performing breast imaging examinations were recorded.

Procedure for assessing intraobserver agreement

MBD assessment between the first (phase 1) and second (phase 2) HRs reading was compared. In phase 1, each radiologist reviewed the anonymized images during regular work hours, with no knowledge of the AI Quantra assessment results.

Each participant repeated this process two weeks after phase 1 with the same images in a randomized order different from the first assessment. In phase 2, the radiologists reviewed the images individually and independently at times that differed from their regular work hours, with no knowledge of the results of their first assessment and the AI Quantra assessment.

Procedure for assessing interobserver agreement

The MBD assessment of the 4-HRs from both phases was compared to a single AI Quantra assessment. Interobserver agreement between AI Quantra and the 4-HRs was assessed in phases 1 and 2. Four and two MBD categories were analyzed.

Protocol for image acquisition and analysis

Digital mammography and digital breast tomosynthesis images were acquired using Selenia Dimensions equipment (Hologic, Bedford, MA, USA) with automatic acquisition parameters. Images were stored and reviewed in the PACS (SecureView, Diagnostic Workstation Bedford, MA, USA). Conventional projections, two CC and two MLO images of both breasts were obtained. Images with breast displacement were evaluated in women with implants. MBD was classified in these images according to the 5th edition of BI-RADS based on the densest area of fibroglandular tissue: category a, almost entirely fat; category b, scattered fibroglandular tissue; category c, heterogeneously dense; and category d, extremely dense.

AI Quantra software

Mammography images were analyzed with AI Quantra version 2.2.2 (Hologic Inc., Bedford, MA, USA). AI Quantra analyzes MBD in images with implant displacements. AI Quantra assessment is based on the distribution and texture of the fibroglandular tissue pattern with an estimate of breast composition based on dense tissue distribution by selecting the densest category according to BI-RADS 5th Edition.

Statistical analysis

Categorical variables are described as frequencies and percentages. The agreement of a dichotomous categorical variable between the 4-HRs was assessed using Cohen's kappa coefficient. The agreement of an ordinal variable between the 4-HRs was assessed with the weighted kappa coefficient. Kappa agreement scores were interpreted with this scale: slight = 0.00-0.20; fair = 0.21-0.40; moderate = 0.41-0.60; substantial = 0.61-0.80; almost perfect = 0.81-1.00. A *p* value < 0.05 was considered significant. The analysis was performed with SPSS version 25 (IBM Corp., Armonk, NY, USA).

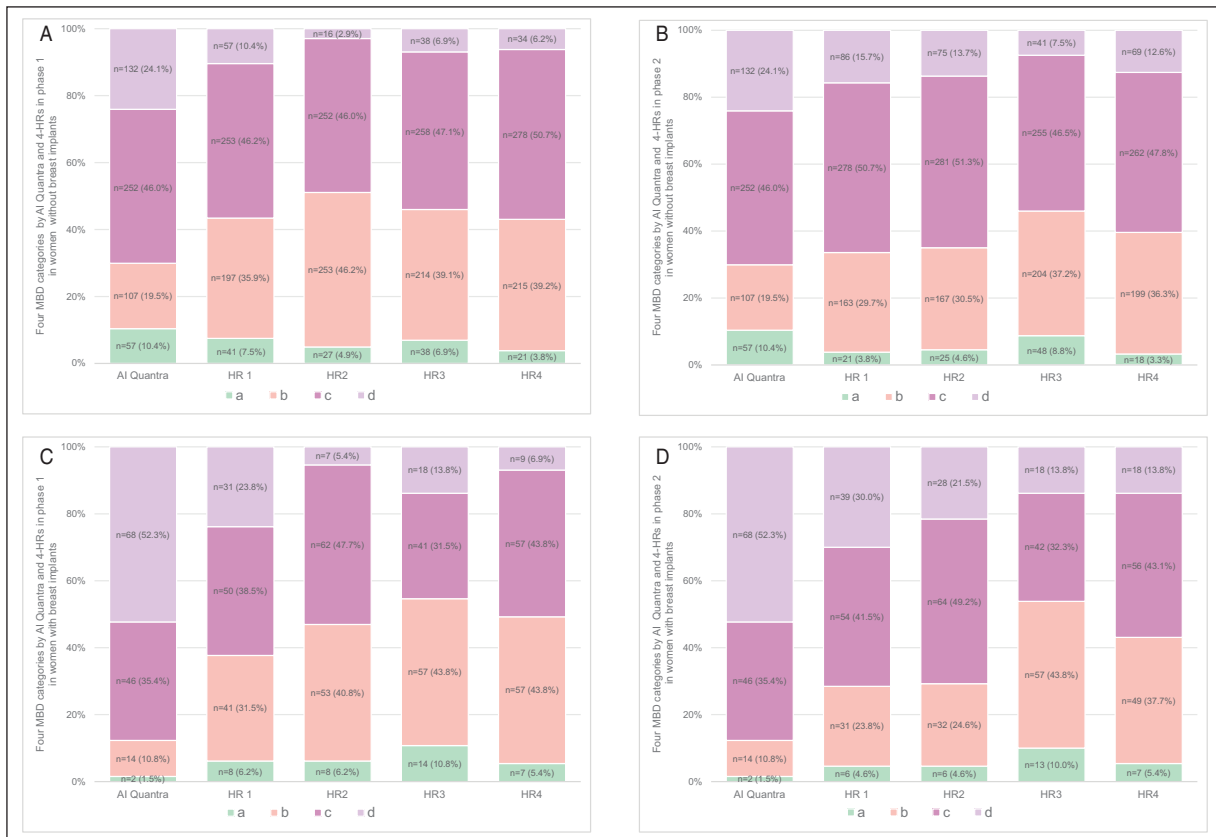


Figure 1. Concordance between AI Quantra and 4-HRs in classifying four MBD categories using BI-RADS 5th Edition: category a, almost entirely fat; category b, scattered fibroglandular tissue; category c, heterogeneously dense; and category d, extremely dense. **A-B:** 548 women without breast implants in phases 1 and 2. **C-D:** 130 women with breast implants in phases 1 and 2.

AI: artificial intelligence; BI-RADS: Breast Imaging Reporting and Data System; HRs: human readers; MBD: mammography breast density.

RESULTS

Four women radiologists with experience in interpreting breast images, ranging from 2 to 32 years, participated in the study.

Classification of the four MBD categories by AI Quantra™ and 4-HRs in phases 1 and 2 in women with and without breast implants

In phase 1, in women without breast implants (n = 548), AI Quantra reported a higher number of mammograms in category d (n = 132) than the 4-HRs (n = 16 to 57) and a higher number of mammograms in category a (n = 57) compared to 4-HRs (n = 21 to 41) (Figure 1A). There was concordance in category c, AI (n = 253) and HRs (n = 252 to 278). AI reported a lower number of mammograms in category b (n = 107) than the 4-HRs (n = 197 to 253).

In phase 2, in the MBD classification of four categories in women without breast implants (n = 548), AI Quantra reported a higher number of mammograms in categories a (n = 57) and d (n = 132) than the 4-HRs (n = 18 to 48) and (n = 41 to 86) (Figure 1B). AI reported a lower number of mammograms in category b (n = 107) than the 4-HRs (163 to 204). AI (n = 252) and the 4-HRs (n = 255 to 281) showed better concordance in category c.

In phase 1, in the MBD classification of four categories in women with breast implants (n = 130), AI Quantra reported a higher number of mammograms in category d (n = 68) than the 4-HRs (n = 7 to 31) (Figure 1C). There was better concordance in category c, AI (n = 46) and HRs (n = 41 to 62). AI reported a lower number of mammograms in categories a (n = 2) and b (n = 14) than the 4-HRs categories a (n = 7 to 14) and b (n = 41 to 57).

Figure 1D shows the MBD classification of four MBD categories in women with breast implants (n = 130) in phase 2. AI Quantra reported a lower number

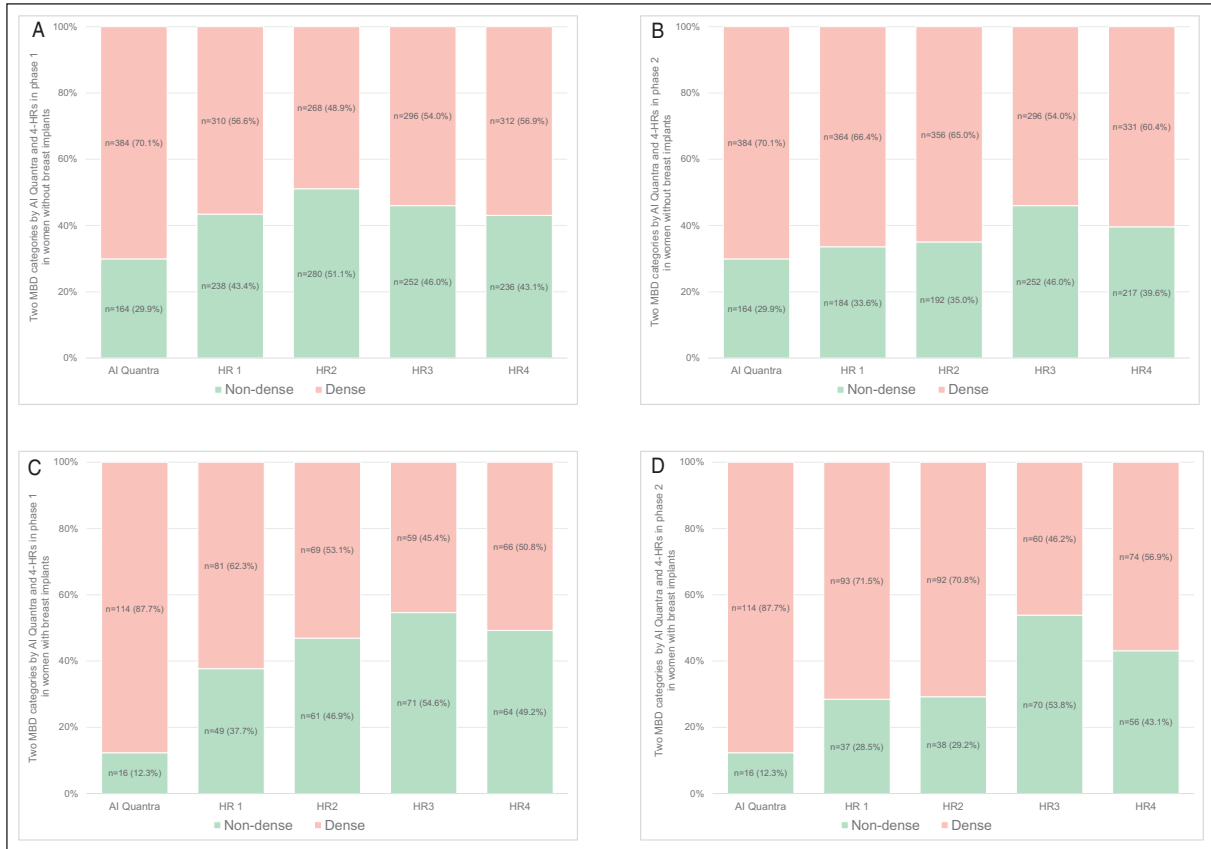


Figure 2. Concordance between AI Quantra and 4-HRs in classifying the two MBD categories (non-dense and dense) using BI-RADS 5th Edition: category a, almost entirely fat; category b, scattered fibroglandular tissue; category c, heterogeneously dense; and category d, extremely dense. **A-B:** 548 women without breast implants in phases 1 and 2. **C-D:** 130 women with breast implants in phases 1 and 2.

AI: artificial intelligence; BI-RADS: Breast Imaging Reporting and Data System; HRs: human readers; MBD: mammography breast density.

of mammograms in categories a ($n = 2$) and b ($n = 14$) than the 4-HRs ($n = 6$ to 13) and ($n = 31$ to 57). AI also reported a higher number in category d ($n = 68$) than the 4-HRs ($n = 18$ to 39). Concordance was better in category c for AI ($n = 46$) and the 4-HRs ($n = 42$ to 64 mammograms).

Classification of the two MBD categories (dense and non-dense) by AI Quantra and the 4-HRs in phases 1 and 2 in women with and without breast implants

In phase 1, in women without breast implants ($n = 548$), AI Quantra classified a higher number of mammograms as dense breasts ($n = 384$) than non-dense breasts ($n = 164$) (Figure 2A). The 4-HRs mammogram assessments of dense breasts ranged from 268 to 312, and of non-dense breasts, 236 to 280.

Figure 2B shows the two MBD categories classification in women without breast implants ($n = 548$) in phase 2. AI Quantra classified a higher number of mammograms

as dense breasts ($n = 384$) than 4-HRs (296 to 364). AI reported fewer mammograms as non-dense breasts ($n = 114$) than the 4-HRs ($n = 184$ to 252).

In phase 1, in the two MBD categories classification in women with breast implants ($n = 130$), AI Quantra reported a higher number of mammograms in the dense breast category ($n = 114$) compared to non-dense breasts ($n = 16$) (Figure 2C). The 4-HRs mammograms ranged from 59 to 81 in the dense breast category and 37 to 71 in non-dense breasts.

Figure 2D shows the two MBD categories classification in women with breast implants ($n = 130$) in phase 2. In this phase, 4-HRs had a lower number of mammograms in the dense breast category (60 to 93) than AI Quantra ($n = 114$). In phase 2, there were greater differences in breast density classification by 4-HRs in women with implants.

Figure 3 shows concordance between 4-HRs and AI Quantra in mammograms of the four MBD categories classification in women without breast implants. Figure 4

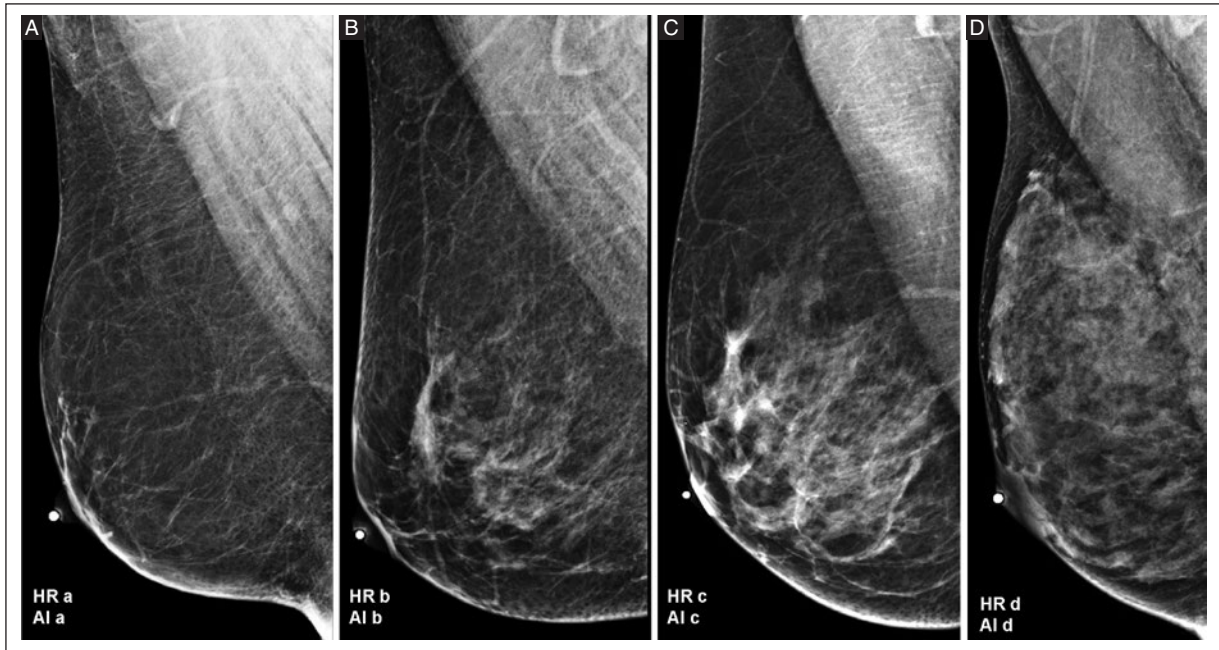


Figure 3. A, B, C, and D: mammography, MLO views of the right breast in women without breast implants showing concordance between 4-HRs and AI Quantra in classifying four MBD categories using BI-RADS 5th Edition: category a, almost entirely fat; category b, scattered fibroglandular tissue; category c, heterogeneously dense; and category d, extremely dense.

AI: artificial intelligence; BI-RADS: Breast Imaging Reporting and Data System; MBD: mammography breast density; HR: human reader; MLO: mediolateral oblique.

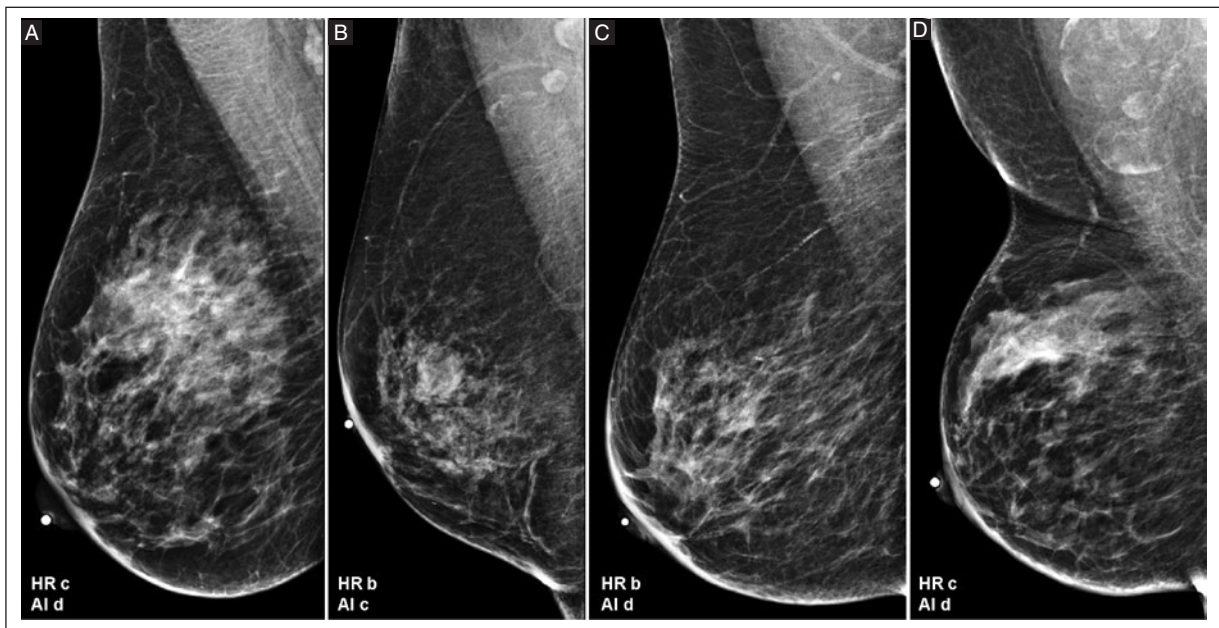


Figure 4. A, B, C, and D: mammography, MLO views of the right breast in women without breast implants, showing no concordance between 4-HRs and AI Quantra in classifying four MBD categories using BI-RADS 5th Edition: category a, almost entirely fat; category b, scattered fibroglandular tissue; category c, heterogeneously dense; and category d, extremely dense.

AI: artificial intelligence; BI-RADS: Breast Imaging Reporting and Data System; HR: human reader; MBD: mammography breast density; MLO: mediolateral oblique.

shows mammograms with no concordance between 4-HRs and AI Quantra in the four MBD categories classification in women without breast implants.

Intraobserver agreement of 4-HRs in the assessment of four and two MBD categories in women with and without breast implants

Intraobserver agreement was substantial for HR 1, 3, and 4, and moderate for HR2 in the four MBD categories in women without breast implants (Table 1). In two MBD categories (non-dense and dense), HR2 and HR4 agreement increased to substantial and almost perfect, respectively ($p < 0.001$). In women with breast implants, intraobserver agreement was comparable as moderate to substantial in the four and two MBD categories (non-dense and dense) ($p < 0.001$) (Table 2).

Interobserver agreement between AI Quantra and 4-HRs for four and two MBD categories in women without breast implants

In women without breast implants in phase 1, interobserver agreement between AI Quantra and 4-HRs was moderate for HR1, HR3, and HR4 and fair for HR2 for the four MBD categories (Table 3). In the two MBD categories, the agreement was moderate for all 4-HRs.

In women without breast implants in phase 2, interobserver agreement between AI Quantra and 4-HRs was moderate for the four and two MBD categories (non-dense and dense) (Table 4). The agreement was substantial for HR1, HR2, and HR4, and moderate for HR3.

Interobserver agreement between AI Quantra and 4-HRs for four and two MBD categories in women with breast implants

For women with breast implants, interobserver agreement between AI Quantra and 4-HRs for four and two MBD categories was slight to fair in both phases (Tables 5 and 6). Figure 5 shows mammograms with concordance between HRs and AI Quantra in classifying the four MBD categories in women with breast implants. Figure 6 shows no concordance between HRs and AI Quantra classifying the four MBD categories in women with breast implants.

DISCUSSION

In our study, the intraobserver agreement of the 4-HRs in the two MBD categories was better in women without breast implants and acceptable in women with breast implants. In women without breast implants, the interobserver agreement between AI Quantra and 4-HRs was acceptable for the two MBD categories. In contrast, for women with breast implants, agreement was unacceptable for the four and two MBD categories. This report is the first that compares MBD assessment between AI Quantra and HRs in women with and without breast implants.

Intraobserver agreement was better (substantial to almost perfect) in women without breast implants in two MBD categories (non-dense and dense), while in four MBD categories intraobserver agreement was comparable between women with and without breast implants. However, in women with implants, intraobserver agreement was acceptable for HRs in four and two MBD categories with substantial agreement for three HRs and moderate for one. The better intraobserver agreement in two MBD categories (non-dense and dense) may be because it is easier for the human eye to distinguish low and high breast density.

The interobserver agreement between AI Quantra and 4-HRs in women without breast implants was moderate to substantial but only fair in HR 2. In contrast, in women with breast implants, interobserver agreement between AI Quantra and the 4-HRs was unacceptable, with slight to fair interobserver agreement in the four and two MBD categories as AI Quantra software was not designed to assess women with breast implants. The human eye has its limitations in assessing women with breast implants. However, the HRs showed an acceptable and comparable MBD assessment in women with and without breast implants.

The concordance in classifying MBD categories by AI Quantra and 4-HRs in both phases, showed fewer non-dense breasts by AI Quantra than by the 4-HRs in women with and without breast implants. In phase 2, although the HRs reported a higher number of dense breasts, AI Quantra had a higher percentage of mammograms reported as dense breasts. The highest concordance of AI Quantra and 4-HRs in both phases was seen in HR1, a radiologist with more years of experience. The concordance in classifying MBD by AI Quantra and 4-HRs was found in 1 out of 4 women with breast implants. It is more difficult to assess breast density in women with breast implants, despite the displaced projections.

Table 1. Intraobserver agreement of 4-HRs in four and two MBD categories between phases 1 and 2 in women without breast implants

Reader	Four MBD categories ^a		Two MBD categories ^b	
	Weighted kappa (95% CI)	Agreement	Light kappa (95% CI)	Agreement
HR1	0.73 (0.68 to 0.77)	Substantial	0.77 (0.72 to 0.82)	Substantial
HR2	0.58 (0.53 to 0.64)	Moderate	0.64 (0.58 to 0.70)	Substantial
HR3	0.78 (0.73 to 0.82)	Substantial	0.79 (0.74 to 0.84)	Substantial
HR4	0.80 (0.76 to 0.84)	Substantial	0.87 (0.83 to 0.91)	Almost perfect

^aFour MBD categories refer to a, b, c, d; ^bTwo MBD categories refer to a+b and c+d (non-dense and dense, respectively). All p values are < 0.001. CI: confidence interval; HRs: human readers; MBD: mammographic breast density.

Table 2. Intraobserver agreement of 4-HRs in four and two MBD categories between phases 1 and 2 in women with breast implants

Reader	Four MBD categories ^a		Two MBD categories ^b	
	Weighted kappa (95% CI)	Agreement	Light kappa (95% CI)	Agreement
HR1	0.74 (0.65 to 0.83)	Substantial	0.76 (0.64 to 0.88)	Substantial
HR2	0.54 (0.44 to 0.64)	Moderate	0.60 (0.48 to 0.73)	Moderate
HR3	0.72 (0.62 to 0.81)	Substantial	0.71 (0.58 to 0.83)	Substantial
HR4	0.74 (0.64 to 0.83)	Substantial	0.78 (0.68 to 0.89)	Substantial

^aFour MBD categories refer to a, b, c, d; ^bTwo MBD categories refer to a+b and c+d (non-dense and dense, respectively). All p values are < 0.001. CI: confidence interval; HRs: human readers; MBD: mammographic breast density.

Table 3. Interobserver agreement between AI Quantra and 4-HRs with four and two MBD categories in women without breast implants in phase 1

Reader	Four MBD categories ^a		Two MBD categories ^b	
	Weighted kappa (95% CI)	Agreement	Light's kappa (95% CI)	Agreement
AI Quantra vs. HR1	0.57 (0.51 to 0.62)	Moderate	0.60 (0.53 to 0.66)	Moderate
AI Quantra vs. HR2	0.40 (0.35 to 0.45)	Fair	0.49 (0.43 to 0.56)	Moderate
AI Quantra vs. HR3	0.48 (0.43 to 0.53)	Moderate	0.55 (0.49 to 0.62)	Moderate
AI Quantra vs. HR4	0.47 (0.42 to 0.52)	Moderate	0.60 (0.53 to 0.66)	Moderate

^aFour MBD categories refer to a, b, c, d; ^bTwo MBD categories refer to a+b and c+d (non-dense and dense, respectively). BI-RADS: Breast Imaging Reporting and Data System; CI: confidence interval. All p values are < 0.001. AI: artificial intelligence; HRs: human readers; MBD: mammographic breast density.

Table 4. Interobserver agreement between AI Quantra and 4-HRs with four or two MBD categories in women without breast implants in phase 2

Reader	Four MBD categories ^a		Two MBD categories ^b	
	Weighted kappa (95%CI)	Agreement	Light kappa (95% CI)	Agreement
AI Quantra vs. HR1	0.59 (0.53 to 0.64)	Moderate	0.65 (0.59 to 0.72)	Substantial
AI Quantra vs. HR2	0.59 (0.54 to 0.64)	Moderate	0.68 (0.62 to 0.75)	Substantial
AI Quantra vs. HR3	0.51 (0.46 to 0.56)	Moderate	0.55 (0.49 to 0.62)	Moderate
AI Quantra vs. HR4	0.56 (0.51 to 0.61)	Moderate	0.64 (0.57 to 0.70)	Substantial

^aFour MBD categories refer to a, b, c, d; ^bTwo MBD categories refer to a+b and c+d (non-dense and dense, respectively). BI-RADS: Breast Imaging Reporting and Data System; CI: confidence interval. All values are p < 0.001. AI: artificial intelligence; HRs: human readers; MBD: mammographic breast density.

Table 5. Interobserver agreement between AI Quantra and 4-HRs with four and two MBD categories in women with breast implants in phase 1

Reader	Four MBD categories ^a		Two MBD categories ^b	
	Weighted kappa (95% CI)	Agreement	Light's kappa (95% CI)	Agreement
AI Quantra vs. HR1	0.24 (0.14 to 0.34)	Fair	0.34 (0.20 to 0.50)	Fair
AI Quantra vs. HR2	0.11 (0.04 to 0.18)	Slight	0.24 (0.12 to 0.36)	Fair
AI Quantra vs. HR3	0.13 (0.05 to 0.20)	Slight	0.18 (0.08 to 0.28)	Slight
AI Quantra vs. HR4	0.11 (0.05 to 0.19)	Slight	0.22 (0.11 to 0.33)	Fair

^aFour MBD categories refer to a, b, c, d; ^bTwo MBD categories refer to a+b and c+d (non-dense and dense, respectively). BI-RADS: Breast Imaging Reporting and Data System; CI: confidence interval. All p values are < 0.001. AI: artificial intelligence; HRs: human readers; MBD: mammographic breast density.

Table 6. Interobserver agreement between AI Quantra and 4-HRs with four and two MBD categories in women with breast implants in phase 2

Reader	Four MBD categories ^a		Two MBD categories ^b	
	Weighted kappa (95% CI)	Agreement	Light kappa (95% CI)	Agreement
AI Quantra vs. HR1	0.22 (0.02 to 0.26)	Fair	0.25 (0.07 to 0.42)	Fair
AI Quantra vs. HR2	0.21 (0.11 to 0.32)	Fair	0.28 (0.11 to 0.46)	Fair
AI Quantra vs. HR3	0.09 (0.01 to 0.17)	Slight	0.16 (0.05 to 0.26)	Slight
AI Quantra vs. HR4	0.13 (0.04 to 0.21)	Slight	0.21 (0.08 to 0.34)	Fair

^aFour MBD categories refer to a, b, c, d; ^bTwo MBD categories refer to a+b and c+d (non-dense and dense, respectively). BI-RADS: Breast Imaging Reporting and Data System; CI: confidence interval. All p values are < 0.001. AI: artificial intelligence; HRs: human readers; MBD: mammographic breast density.

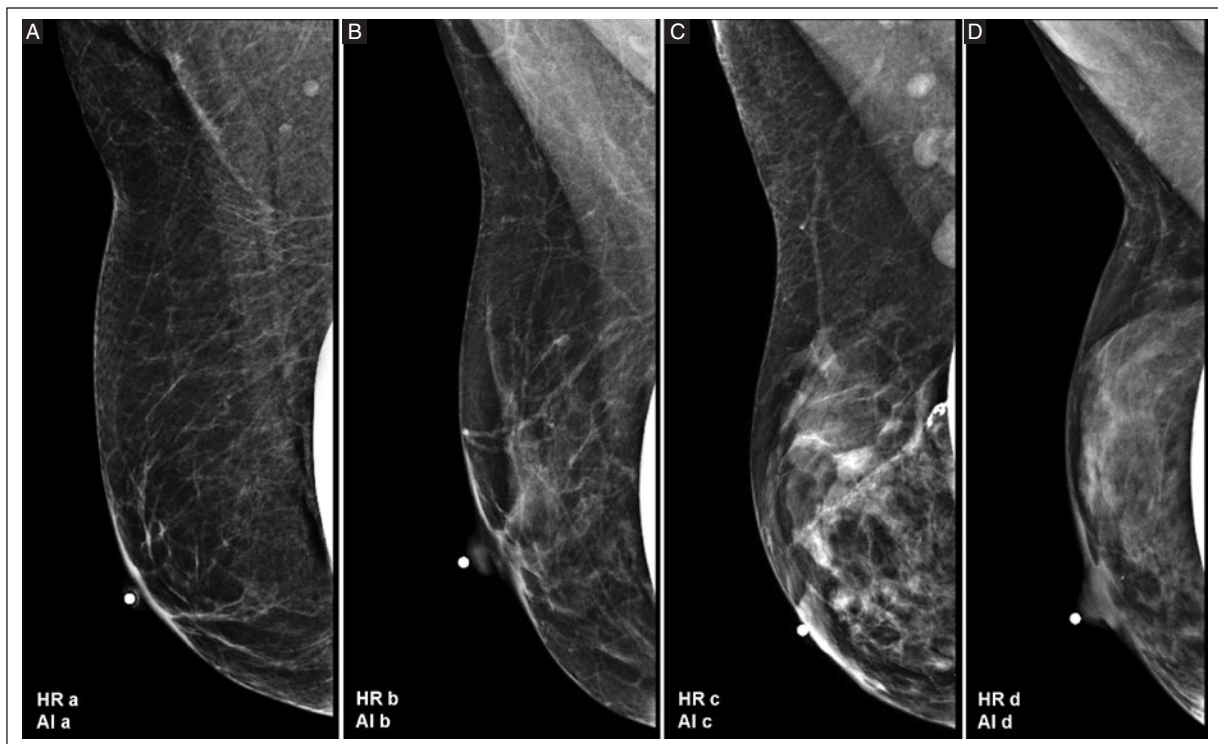


Figure 5. A, B, C, and D: mammography, MLOID views of the right breast in women with breast implants showing concordance between HRs and AI Quantra in classifying four MBD categories using BI-RADS 5th Edition: category a, almost entirely fat; category b, scattered fibroglandular tissue; category c, heterogeneously dense; and category d, extremely dense.

AI: artificial intelligence; BI-RADS: Breast Imaging Reporting and Data System; MBD: mammography breast density; HR: human reader; MLOID: implant displacement mediolateral oblique.

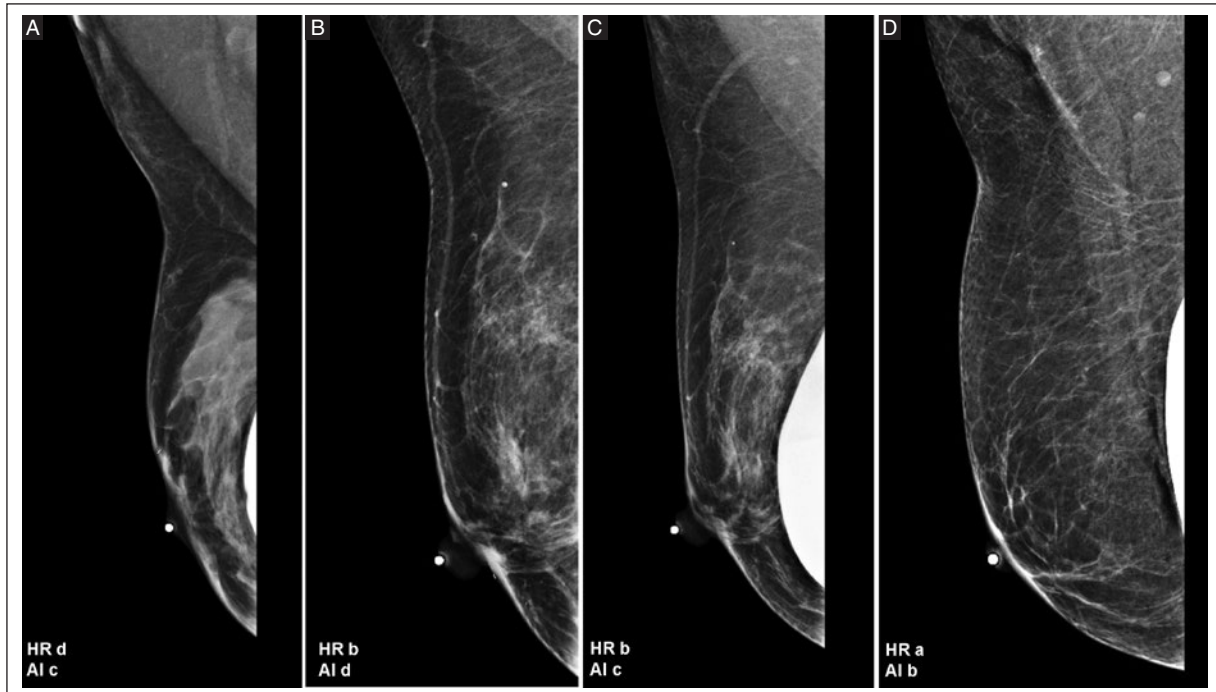


Figure 6. A, B, C, and D: mammography, MLOID views of the right breast in women with breast implants show no concordance between HRs and AI Quantra in classifying four MBD categories using BI-RADS 5th Edition: category a, almost entirely fat; category b, scattered fibroglandular tissue; category c, heterogeneously dense; and category d, extremely dense.

AI: artificial intelligence; BI-RADS: Breast Imaging Reporting and Data System; HR: human reader; MBD: mammography breast density; MLOID: implant displacement mediolateral oblique.

The strengths of our study include the prospective design, the participation of four radiologists with different levels of breast imaging experience, and a sufficient sample size to determine intraobserver and interobserver agreement. The study has several limitations: it evaluated only Quantra software, is a single-institution study, was performed by four radiologists at the same workstation, and all mammograms were acquired from a single mammography unit.

CONCLUSION

In our study, intraobserver agreement of the 4-HRs in women without breast implants was better (substantial to almost perfect) for the two MBD categories than for the four MBD categories, while in women with breast implants, intraobserver agreement was comparable (moderate to substantial) for both the four and two MBD categories. In women without breast implants, the interobserver agreement between AI Quantra and 4-HRs was acceptable (moderate to substantial) for the two MBD categories. However, for women with breast implants, the interobserver agreement between AI

Quantra and 4-HRs was unacceptable (slight to fair) for both the four and two MBD categories. It would be advisable for the industry to offer software capable of assessing MBD in women with breast implants since there is increasing number of them every day. Prospective studies with a large sample size in different populations are needed to assess the reproducibility of AI Quantra in assessing MBD.

Acknowledgments

The authors thank Professor Ana M. Contreras-Navarro for her guidance in preparing and writing this scientific paper.

Funding

This research received no external funding.

Conflicts of interest

The authors declare no conflicts of interest.

Ethical considerations

Protection of humans and animals. The authors declare that no experiments involving humans or animals were conducted for this research.



Confidentiality, informed consent, and ethical approval. The authors have obtained approval from the Ethics Committee for the analysis of routinely obtained and anonymized clinical data, so informed consent was not necessary. Relevant guidelines were followed.

Declaration on the use of artificial intelligence. The authors declare that no generative artificial intelligence was used in the writing of this manuscript.

REFERENCES

- McCormack VA, dos Santos Silva I. Breast density and parenchymal patterns as markers of breast cancer risk: a meta-analysis. *Cancer Epidemiol Biomarkers Prev.* 2006;15(6):1159-1169. doi: 10.1158/1055-9965.EPI-06-0034.
- Miglioretti DL, Rutter CM, Geller BM, Cutter G, Barlow WE, Rosenberg R, et al. Effect of breast augmentation on the accuracy of mammography and cancer characteristics. *JAMA.* 2004;291(4):442-450. doi: 10.1001/jama.291.4.442.
- Handel N. The effect of silicone implants on the diagnosis, prognosis, and treatment of breast cancer. *Plast Reconstr Surg.* 2007;120 (7 Suppl 1): 81S-93S. doi:10.1097/01.prs.0000286578.94102.2b.
- D'Orsi C, Sickles EA, Mendelson EB, Morris EA. *Breast Imaging Reporting and Data System: ACR BI-RADS breast imaging atlas.* 5th Edition. Reston: American College of Radiology. 2013.
- American College of Radiology. *ACR BI-RADS Atlas: Breast Imaging Reporting and Data System.* 5th. Reston, VA: American College of Radiology; 2013. ACR BI-RADS® Mammography.
- Richard-Davis G, Whittemore B, Disher A, Rice VM, Lenin RB, Dollins C, et al. Evaluation of Quantra Hologic Volumetric Computerized Breast Density Software in Comparison with Manual Interpretation in a Diverse Population. *Breast Cancer (Auckl).* 2018; 12:1178223418759296. doi: 10.1177/1178223418759296.
- Rahmat K, Ab Mumin N, Ramli Hamid MT, Fadzli F, Ng WL, Muhammad Gowdh NF. Evaluation of automated volumetric breast density software in comparison with visual assessments in an Asian population: A retrospective observational study. *Medicine (Baltimore).* 2020;99(39): e22405. doi: 10.1097/MD.00000000000022405.
- Ciatto S, Houssami N, Apruzzese A, Bassetti E, Brancato B, Carozzi F, et al. Categorizing breast mammographic density: intra- and interobserver reproducibility of BI-RADS density categories. *Breast.* 2005;14(4): 269-275. doi: 10.1016/j.breast.2004.12.004.
- Tari DU, Santonastaso R, De Lucia DR, Santarsiere M, Pinto F. Breast Density Evaluation According to BI-RADS 5th Edition on Digital Breast Tomosynthesis: AI Automated Assessment Versus Human Visual Assessment. *J Pers Med.* 2023;13(4):609. doi:10.3390/jpm13040609.
- Delsol-Perez C, Reyes-Mosqueda A, Rios-Rodriguez T, Perez-Montemayor D. Interobserver agreement between radiologists and artificial intelligence in mammographic breast density classification. *J Mex Fed Radiol Imaging.* 2024;3(2):122-127. doi: 10.24875/JMEXFRI.M24000074.
- Sartor H, Lång K, Rosso A, Borgquist S, Zackrisson S, Timberg P. Measuring mammographic density: comparing a fully automated volumetric assessment versus European radiologists' qualitative classification. *Eur Radiol.* 2016;26(12):4354-4360. doi: 10.1007/s00330-016-4309-3.
- Kusumaningtyas N, Supit N, Murtala B, Muis M, Chandra M, Sanjaya E, et al. A systematic review and meta-analysis of correlation of automated breast density measurement. *Radiography (Lond).* 2024;30(5):1455-1467. doi: 10.1016/j.radi.2024.08.003.
- Larsen M, Aglen CF, Lee CI, Hoff SR, Lund-Hanssen H, Lång K, et al. Artificial Intelligence Evaluation of 122 969 Mammography Examinations from a Population-based Screening Program. *Radiology.* 2022;303(3): 502-511. doi: 10.1148/radiol.212381.
- Larsen M, Olstad CF, Lee CI, Hovda T, Hoff S, Marinussen M. Performance of an AI System for Breast Cancer Detection on Screening Mammograms from Breast Screen Norway. *Radiol Artif Intell.* 2024;6(3): e230375. doi.org/10.1148/ryai.230375.
- Taylor CR, Monga N, Johnson C, Hawley JR, Patel M. Artificial Intelligence Applications in Breast Imaging: Current Status and Future Directions. *Diagnostics (Basel).* 2023;13(12):2041. doi: 10.3390/diagnostics 13122041.
- Hologic Inc. *Understanding Quantra 2.2 user guide for cenova 3.0.1 English Man 05503-302 rev 002.* Hologic; Bedford, MA, USA: 2019. <https://www.hologic.com>.
- Lunit INSIGHT MMG. <https://www.lunit.io/en/products/mmg>. Accessed February 18, 2024.
- Gonzalez-Ulloa B, Corona-Gonzalez C, Molina-Gutierrez R. Mammography breast density assessment with Quantra artificial intelligence software: intra and interobserver agreement with radiologist. *J Mex Fed Radiol Imaging.* 2024;3(4):221-230. doi:10.24875/JMEXFRI.M24000088.

Duplex US acquisition and analysis protocol for portal hypertension: a technical note

Mauricio Figueroa-Sanchez^{1,2,3*}, Aldo A. Montero-Cedeño⁴, and Guillermo Subias-Rodriguez^{5,6}

¹Radiology and Imaging Department, Antiguo Hospital Civil of Guadalajara “Fray Antonio Alcalde”; ²University Center of Health Sciences, Universidad of Guadalajara; ³Laboratorio Vascular S.C.; ⁴Bañuelos Radiólogos Centro de Neuroimagen. Guadalajara, Jalisco, Mexico; ⁵Facultad Mexicana de Medicina de la Universidad La Salle; ⁶Hospital Angeles. Mexico City, Mexico

ABSTRACT

Duplex ultrasound (US) is a useful non-invasive imaging modality with high specificity and moderate sensitivity for assessing portal hypertension. Liver cirrhosis is the most common cause of portal hypertension, accounting for 90% of all causes. Portal hypertension can cause complications such as variceal bleeding, ascites, and hepatic encephalopathy. A comprehensive duplex US acquisition and analysis protocol for portal hypertension, as well as its usefulness for evaluation, etiology, and anatomic location, has not been established. This technical note proposes a comprehensive duplex US protocol for portal hypertension that uses a vascular preset of the abdomen and liver and morphologic and hemodynamic assessment of five regions in sequential order: splenic, pancreatic, cardiac, hepatic, and inframesocolic. Morphological parameters include dimension, volume, echotexture, echogenicity, and the presence of lesions. Hemodynamic parameters include vessel diameter, flow direction, spectral morphology, flow velocity, the presence of thrombi, resistance index (RI), and pulsatility index (PI). In the liver, the assessment includes atrophy or hypertrophy, regenerative nodules, and the surface pattern. Hepatic and splenic elastography are recommended as complementary examinations. This technical note, which includes all available duplex US modalities, such as grayscale, color Doppler, power Doppler, and B-Flow examinations, is published for educational purposes.

Keywords: Portal hypertension. Ultrasound. Duplex ultrasound. Liver cirrhosis. Technical note.

INTRODUCTION

Portal hypertension is a serious complication of chronic liver disease (CLD) that can lead to variceal bleeding, ascites, and hepatic encephalopathy^{1,2}. A non-invasive imaging examination that assesses portal hypertension is recommended because measurement of the hepatic venous pressure gradient (HVPG), the gold standard for diagnosing portal hypertension, is invasive and requires direct cannulation of the right

main hepatic vein by an interventional radiologist³. In addition, this examination is costly and difficult to access in low-to-middle-income countries, such as Mexico. Duplex ultrasound (US) is a useful non-invasive imaging modality for the evaluation of portal hypertension. It has high specificity and moderate sensitivity for detecting portal hypertension^{4,5}. Duplex US examination may have implications for etiologic and non-etiological therapies, prevention of the first episode of decompensation, management of acute bleeding

*Corresponding author:

Mauricio Figueroa-Sanchez

E-mail: figueroa_sanchez@hotmail.com

2696-8444 / © 2025 Federación Mexicana de Radiología e Imagen, A.C. Published by Permanyer. This is an open access article under the CC BY-NC-ND (<https://creativecommons.org/licenses/by-nc-nd/4.0/>).

Received for publication: 23-01-2025

Accepted for publication: 08-03-2025

DOI: 10.24875/JMEXFRI.M25000104

Available online: 15-07-2025

J Mex Fed Radiol Imaging. 2025;4(2):112-124

www.JMeXFRI.com

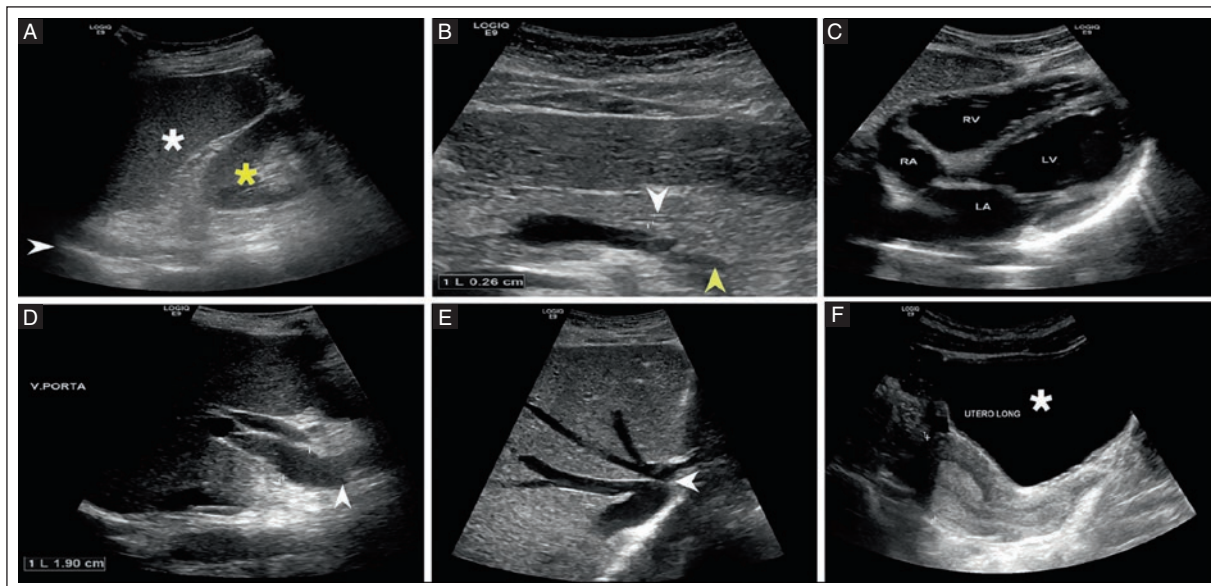


Figure 1. Duplex grayscale US showing the 5 regions of the portal hypertension assessment protocol. **A:** splenic region, sagittal view, showing the spleen (white asterisk), hemidiaphragm (arrowhead), and left kidney (yellow asterisk) with no abnormalities. **B:** pancreatic region, transverse view, showing normal pancreas, Wirsung duct (white arrowhead), splenic vein (yellow arrowhead), and peripancreatic region. **C:** cardiac region with subxiphoid approach, view of the four chambers with no alterations. **D:** hepatic region with intercostal approach, sagittal view, showing portal vein dilatation (19 mm) (white arrowhead). **E:** hepatic region with subcostal approach, transverse view, showing the three hepatic veins at their confluence with the vena cava (white arrowhead). **F:** inframesocolic region, sagittal view, showing bladder (asterisk) and uterus with normal size and morphology without ascites.

US: ultrasound.

episodes, prevention of further decompensation, and diagnosis and management of splanchnic vein thrombosis and other vascular disorders of the liver^{3,4,6}.

Hepatic and splenic elastography are complementary and useful in predicting the severity of portal hypertension^{3,5,7,8}. Contrast-enhanced duplex US examination can improve the detection of vascular abnormalities and the assessment of portal hemodynamics⁵. The presence or absence of splenomegaly, gastroesophageal varices, portosystemic shunts, or ascites on computed tomography may be helpful to confirm or rule out clinically significant portal hypertension in CLD patients⁹. On the other hand, magnetic resonance imaging is useful for visualizing portosystemic collaterals, confirming the presence of portal vein thrombosis or cavernoma, and, in some cases, provides information on flow and hemodynamics^{3,6}.

Portal pressure is normally between 7 and 12 mmHg at rest and under fasting conditions. The HVPG represents the portal perfusion pressure of the liver, which is between 1 and 4 mmHg. Values above 5 mmHg indicate portal hypertension and values above 10 mmHg correspond to clinically significant portal hypertension, which is when clinical complications ensue.

The causes of portal hypertension can be classified according to their anatomical location¹: prehepatic, intrahepatic, or posthepatic³. Liver cirrhosis is the most common cause of portal hypertension, accounting for 90% of all causes. The formation of scar tissue and regenerative nodules leads to increased intrahepatic vascular resistance and portal pressure³. The most common extrahepatic cause of portal hypertension is portal vein thrombosis in the trunk of the portal vein or its branches³. This condition often occurs in the context of CLD^{4,6}. A comprehensive duplex US acquisition and analysis protocol for portal hypertension and its usefulness for assessment, etiology, and anatomic location has not been defined³. This technical note proposes a comprehensive duplex US acquisition and analysis protocol for portal hypertension.

DUPLEX US PORTAL HYPERTENSION PROTOCOL

The duplex US acquisition and analysis protocol includes morphologic and hemodynamic assessment of five regions in sequential order: splenic (Figure 1A), pancreatic (Figure 1B), cardiac (Figure 1C), hepatic

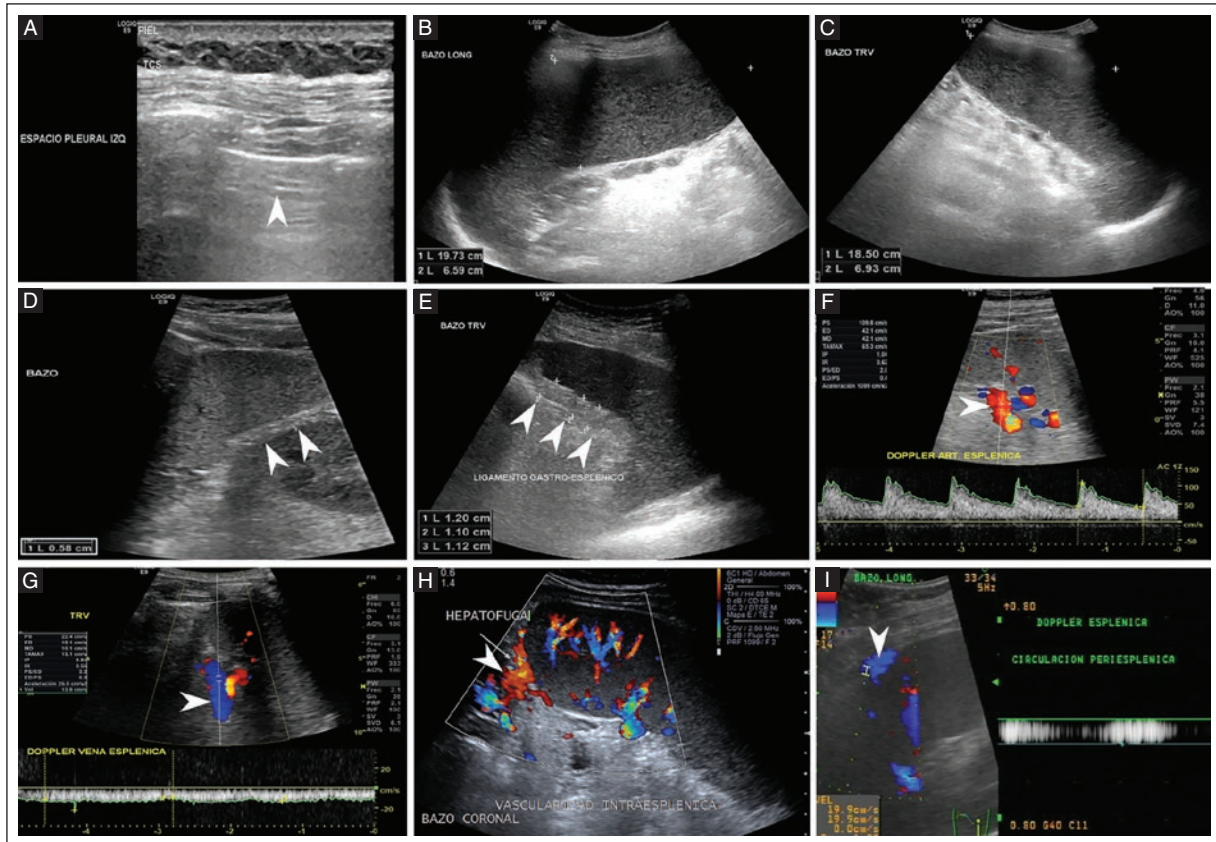


Figure 2. Morphologic US duplex findings of the splenic region in portal hypertension assessment. **A:** a 71-year-old man with CLD. Grayscale US, sagittal view with high-frequency linear transducer (10 MHz) with normal left pleural space (white arrowhead) without pleural effusion. **B-C:** a 59-year-old woman diagnosed with CLD. Grayscale US, longitudinal and transverse view, with longitudinal (19.7 cm), anteroposterior (6.5 cm), and transverse (18.5 cm) diameters and a spleen volume of 1,238 cm³ (not shown). **D:** a 27-year-old man with CLD, sagittal view of the spleen in grayscale US with normal gastro-splenic ligament (5.8 mm) (arrowheads). **E:** a 78-year-old woman with CLD, transverse view of the spleen with thickening of the gastro-splenic ligament (11 to 12 mm) (arrowheads). Hemodynamic US duplex findings of the splenic region in portal hypertension assessment. **F:** US duplex of a 30-year-old man with CLD, transverse view, showing splenic artery with patency; spectral morphology with a slight increase in velocity (109.8 cm/s) (arrowhead). **G:** US duplex of a 40-year-old man, transverse view, showing the splenic vein with patency, hepato-petal flow, and normal velocity of 22.4 cm/s (arrowhead). **H:** color Doppler US of a 46-year-old man with CLD, transverse view, showing increased intrasplenic vascularity and hepatofugal flow in the upper perisplenic area (white arrowhead). **I:** a 59-year-old woman with CLD, US duplex Doppler, sagittal view, showing perisplenic hepatofugal flow in the upper and subphrenic areas (arrowhead).
 US: ultrasound; CLD: chronic liver disease.

(Figure 1D-E), and inframesocolic (Figure 1F) regions. The patient should fast for 4-6 hours and ingest two liters of water two hours before starting the duplex US examination; if necessary, the patient can drink one or two additional glasses of water to achieve adequate gastric distension.

Morphologic duplex US findings of the splenic region in portal hypertension assessment

The evaluation begins with grayscale US with longitudinal and transverse projections in the left lung base with

the patient in the right lateral decubitus. The mobility of the diaphragm and the presence of lesions are assessed. In the pleural space, the presence of pleural effusion is evaluated, and collections or lesions in the subphrenic space are described (Figure 2A).

The examination continues with the spleen in the longitudinal projection, measuring the longitudinal and anteroposterior diameter (cm) (Figure 2B), and in the transverse projection, measuring the transverse diameter (cm) (Figure 2C) (Table 1A). The spleen volume is determined from these three measurements (cm³) whereby the normal value must be less than 322 (cm³)¹⁰. The echotexture of the spleen (homogeneous or

Table 1A. Morphologic grayscale US findings of the splenic region in portal hypertension assessment

Description	Dimension	Echotexture (homogeneous/heterogeneous)	Echogenicity	Lesion (yes/no)
Spleen, volume, $L \times AP \times T^a$, cm^3				
Gastrosplenic ligament ^b , AP, mm				
Left kidney, volume, $L \times AP \times T$, cm^3				

^aThe volume is calculated by multiplying these parameters: the result is multiplied by 0.52⁹; ^bOnly one diameter is measured for the gastrosplenic ligament; with an upper normal limit of 8 mm (author's experience, MFS). AP: anteroposterior; L: longitudinal; T: transverse; US: ultrasound.

Table 1B. Hemodynamic duplex US findings in the splenic region^a in portal hypertension assessment

Description	Diameter (mm)	Direction of flow (antegrade/retrograde)	Spectral morphology	Flow velocity (cm/s)	Thrombosis (yes/no)
Splenic artery ^b					
Splenic vein ^c					
Splenic hilar collateral circulation					
Collateral perisplenic upper circulation					
Collateral perisplenic inferior circulation					
Gastrosplenic shunts					
Left renal artery ^b					
Left renal vein					
Splenorenal shunts					

^aThe evaluation is supplemented by splenic elastography; ^bSplenic and left renal arteries: to assess resistivity index (RI) and pulsatility index (PI). ^cThe intrasplenic vascularity is qualitatively assessed to determine whether it is decreased or increased. US: ultrasound.

heterogeneous), echogenicity (hyperechogenic, iso-echogenic, or hypoechoic), and focal lesions are evaluated together with their characteristics. The anteroposterior diameter of the gastrosplenic ligament is measured on the inner surface of the spleen. The normal value is less than 8 mm (Fig. 2D); thickening is considered to be greater than 8 mm (author's experience, MFS) as, to our knowledge, there is no reference to this finding in the medical literature in relation to portal hypertension (Figure 2E). The examination continues with the left kidney in longitudinal and transverse projections, measuring the longitudinal, anteroposterior, and transverse diameters¹¹. The volume is calculated by multiplying these parameters. The results are then multiplied by 0.52, which corresponds to the formula of an ellipsoid¹¹.

Hemodynamic duplex US findings of the splenic region in portal hypertension assessment

It starts in the splenic artery (Figure 2F) with the assessment of diameter (mm), flow direction (antegrade

or retrograde), spectral morphology, flow velocity (cm/s), the presence of thrombi, resistance index (RI) (normal value of 0.56)^{4,12}, and the pulsatility index (PI) (normal value ≥ 1)⁴ (Table 1B).

We continue with the splenic vein (Figure 2G) and evaluate the same parameters as those of the splenic artery. The ideal position for assessment is the transverse section of the spleen to obtain an approximate angle of 0 degrees. Intrasplenic vascularity is assessed qualitatively to determine whether it is increased or decreased (Figure 2H). The presence of collateral circulation in the splenic hilum, upper (Figure 2I) and lower perisplenic regions, and gastrosplenic shunts is assessed.

The left renal artery is assessed for diameter (mm), flow direction, spectral morphology (monophasic, biphasic, triphasic, or tetraphasic), flow velocity (cm/s), and the presence of thrombi, as well as RI (normal value < 0.7) and PI (normal value between 1.0 and 1.5)¹³. We continue with the left renal vein to determine the diameter (mm), flow direction, spectral morphology, flow velocity (cm/s), the presence of thrombi, and confirm or rule out a splenorenal shunt; this finding is always considered abnormal.

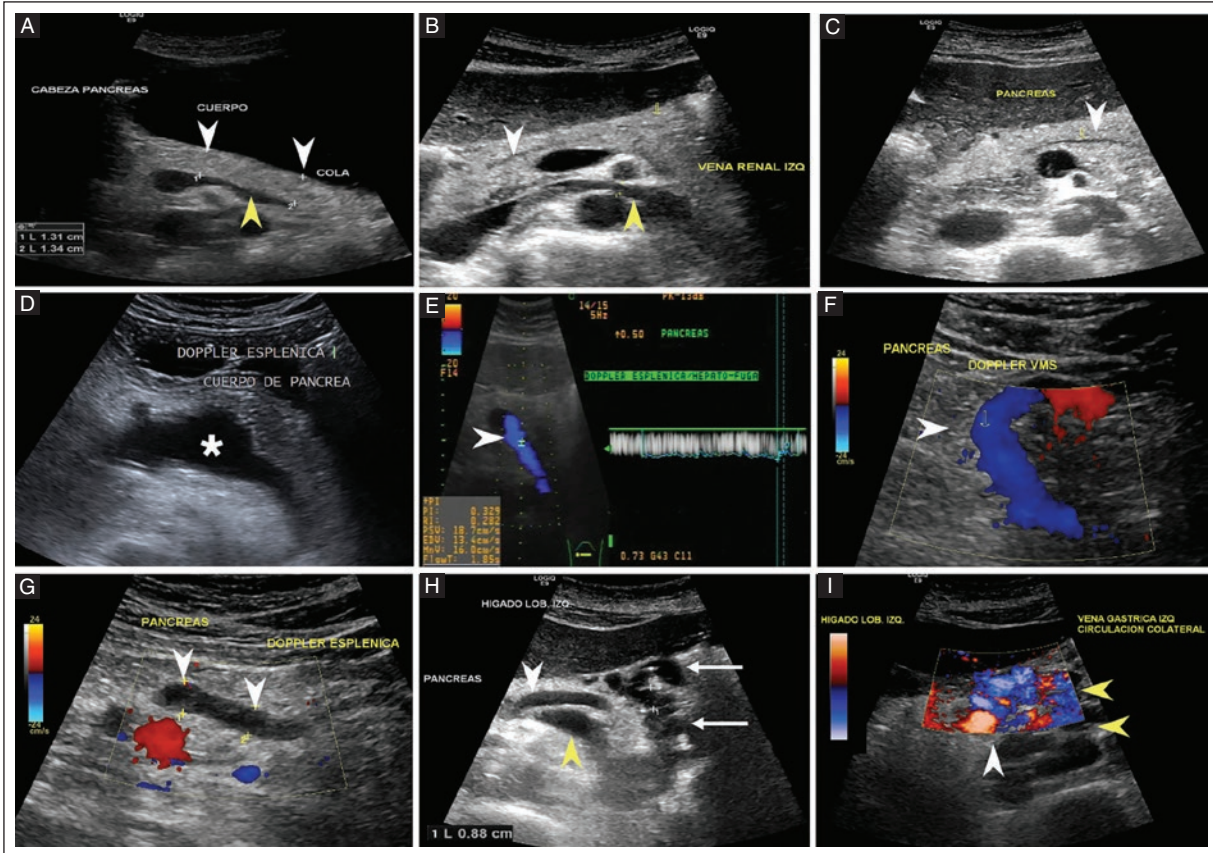


Figure 3. Morphologic US duplex findings of the pancreatic region in portal hypertension assessment. **A:** a 32-year-old woman, transverse grayscale view showing all segments of the pancreas (white arrowheads) and splenic vein (yellow arrowhead) with AP measurement of the pancreatic body and tail of 13 mm. **B:** a 39-year-old woman, grayscale US transverse view showing normal pancreas and Wirsung duct 2.6 mm (not shown) (white arrowhead) and left renal vein (yellow arrowhead) until it reaches the vena cava. **C:** a 48-year-old man with CLD. Grayscale US transverse view showing normal pancreas and Wirsung duct (white arrowhead). **D:** a 46-year-old woman with CLD. Grayscale US transverse view of the pancreas showing aneurysmal dilatation (22 mm, not shown) of the splenic vein (white asterisk). Hemodynamic US duplex findings of the pancreatic region in portal hypertension assessment. **E:** a 41-year-old male with portal hypertension; US duplex transverse view of the pancreas showing hepatofugal flow in the splenic vein at a velocity of 18.7 cm/s (arrowhead). A 48-year-old man with idiopathic portal hypertension. **F:** color Doppler sagittal view of the superior mesenteric vein (white arrowhead) with patency and hepatofugal flow. **G:** color Doppler US, transverse view of the pancreas with endoluminal hypoechoic material along the entire length of the splenic vein (white arrowheads) with absent flow due to chronic thrombosis. **H:** a 59-year-old woman with CLD. Grayscale US transverse view of the pancreas showing normal artery (white arrowhead) and splenic vein (yellow arrowhead) and 8.8 mm peripancreatic collateral circulation (white arrows). **I:** a 59-year-old woman with CLD, color Doppler US transverse view showing the left gastric vein (white arrowhead) and the adjacent collateral circulation (yellow arrowheads).

AP: anteroposterior; CLD: chronic liver disease; US: ultrasound.

Morphologic duplex US findings of the pancreatic region in portal hypertension assessment

With the patient in the right lateral decubitus position and later in the supine decubitus position, we proceed with a morphologic assessment of the pancreatic region using the splenic vein (Figure 3A) and the left renal vein (Figure 3B) as anatomic references (Table 2A). The pancreas is assessed by measuring (cm) all segments, the

head, body, and tail, its echotexture (homogeneous or heterogeneous), its echogenicity (compared to the liver), and the presence of lesions. The AP diameter of the Wirsung duct (normal, 2-3 mm) and its morphology according to contours, regular or irregular (Figure 3C), are evaluated. Identification of the Wirsung duct can be difficult if it is not dilated, especially for inexperienced operators. Intraductal stones associated with chronic calcifying pancreatitis may be encountered.

Table 2A. Morphologic US grayscale findings of the pancreatic region in portal hypertension assessment

Description	Dimension	Echotexture (homogeneous/heterogeneous)	Echogenicity relative to the liver	Lesion (yes/no)
Pancreas, cm				
AP view head				
AP view body				
AP view tail				
Wirsung duct ^{a,b} , mm				

^aIt is only visible when dilated. It can be difficult to identify for inexperienced observers if it is not dilated; ^bMorphology: regular or irregular. AP: anteroposterior; US: ultrasound.

Table 2B. Hemodynamic duplex US findings in the pancreatic region in portal hypertension assessment

Description	Diameter (mm)	Direction of flow (antegrade/retrograde)	Spectral morphology	Flow velocity (cm/s)	Thrombosis (yes/no)
Splenic vein					
Superior mesenteric vein					
Collateral peripancreatic circulation					
Collateral periduodenal circulation					
Collateral perigastric circulation					
Collateral periesophageal circulation					
Collateral retroperitoneal circulation					
Collateral paraumbilical circulation					
Left gastric vein					

US: ultrasound.

Hemodynamic duplex US findings of the pancreatic region in portal hypertension assessment

The splenic vein is examined along its entire course from the splenic hilum to its junction with the superior mesenteric vein and the splenomesoportal confluence (Table 2B). The diameter (mm) (Figure 3D), the antero- grade or retrograde flow direction (Figure 3E-F), spec- tral morphology, flow velocity (cm/s), and the presence of a thrombus (Figure 3G) are determined.

The peripancreatic collateral circulation (Figure 3H) and the periduodenal, perigastric, periesophageal, retro- peritoneal, and paraumbilical circulation are assessed by determining the diameter (mm), antero- grade or retrograde flow direction, spectral morphology, flow velocity (cm/s),

and the presence of a thrombus. The left gastric vein is evaluated with the same parameters. Its normal diameter is < 5 mm (Figure 3I)¹⁴.

Duplex US findings of the cardiac region in portal hypertension assessment

The vena cava hiatus is assessed with duplex US, determining the diameter, flow direction, spectral mor- phology, flow velocity, and the presence of thrombosis (Table 3). Grayscale US examination with a subxiphoid approach and cephalic orientation identifies the four heart chambers and evaluates their mobility, interven- tricular septum integrity, right and left ventricle, and right and left atrium diameters, and the presence of thrombi, myxomas, or pericardial effusion.

Table 3. Duplex US findings of the cardiac region in portal hypertension assessment

Description
<p>Duplex US: Caval hiatus, measurement of diameter, assessment of permeability, anterograde or retrograde flow direction, spectral morphology, flow velocity, and presence of thrombosis.</p>
<p>Grayscale US: Four-chamber view of the heart: check motility integrity of the interventricular septum diameter of each of the four chambers, presence of thrombosis, myxoma or pericardial effusion, and in the vena cava, flow velocity, spectral morphology, flow direction, and presence of thrombosis.</p>

US: ultrasound.

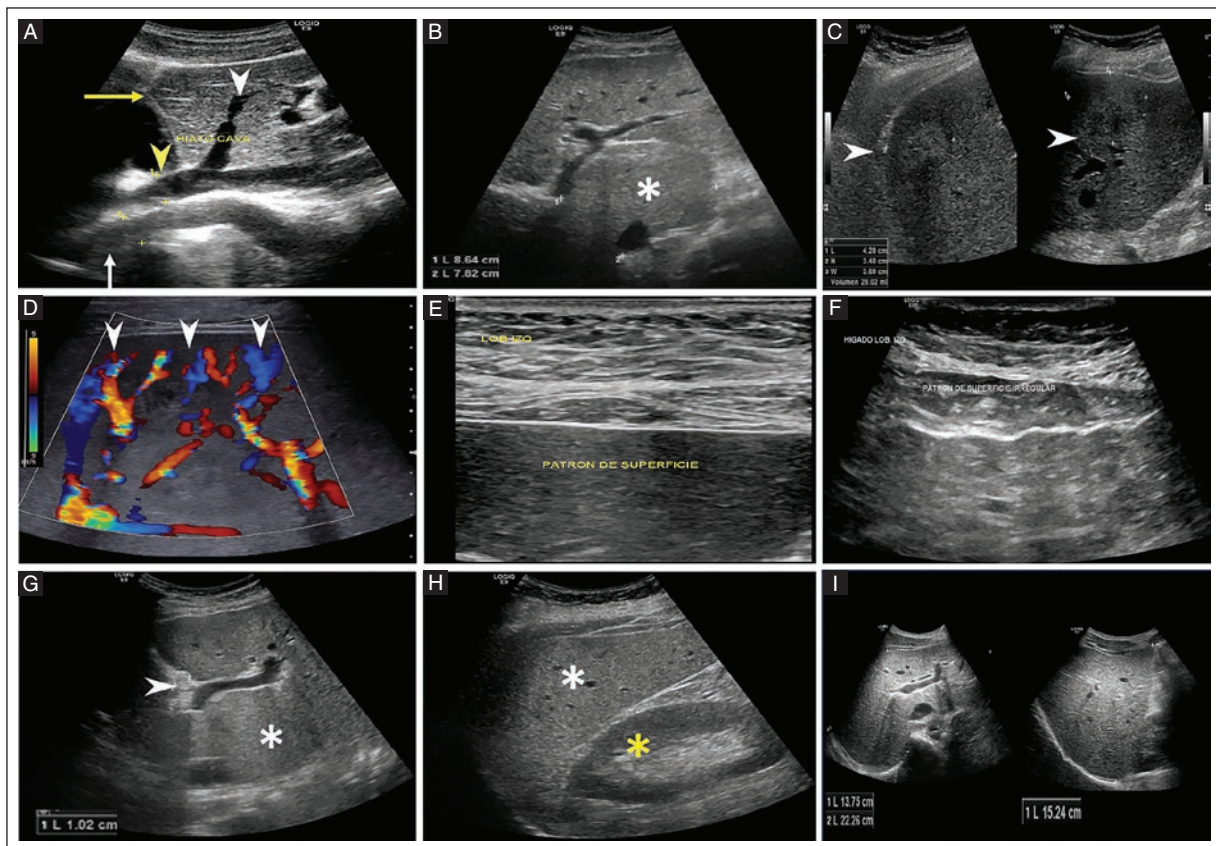


Figure 4. Morphologic grayscale US findings of the hepatic region in the assessment of portal hypertension. **A:** a 22-year-old woman, grayscale US, longitudinal view showing the left hepatic lobe, hiatus cava (yellow arrowhead), left hepatic vein (white arrowhead), left hemidiaphragm (yellow arrow), and aortic hiatus (white arrow) with no alterations. **B:** a 69-year-old man with alcoholic liver disease, Grayscale US transverse view of the left lobe showing left portal vein, venous ligament, and compensatory hypertrophy of the caudate lobe (white asterisk). **C:** an 81-year-old woman with CLD. Grayscale US, sagittal, and transverse views of the right hepatic lobe in segment V with a hyperechogenic, solid, well-defined image measuring $4.2 \times 3.6 \times 3.4$ cm in longitudinal, transverse and AP diameters, respectively. Regeneration nodule volume of 28 cc (white arrowheads). **D:** a 28-year-old man with hepatocarcinoma. US color Doppler shows a solid lesion with hypervascularity within it and neoformation vessels. **E:** a 35-year-old woman, Grayscale US, obtained with a high-frequency linear transducer showing a normal surface pattern of the left hepatic lobe with smooth borders. **F:** a 78-year-old woman with CLD, image obtained with a high-frequency linear transducer showing an irregular surface pattern of the left hepatic lobe and a heterogeneous echotexture. **G:** a 69-year-old man with alcoholic liver disease, Grayscale US, transverse view of the left hepatic lobe showing a 10 mm thickening of the falciform ligament (white arrowhead) and hypertrophy of the caudate lobe (white asterisk). **H:** a 32-year-old man. Grayscale US with diffusely increased echogenicity of the right hepatic lobe (white asterisk) and normal right kidney (yellow asterisk). **I:** a 40-year-old woman with no liver pathology, composite image with transverse and longitudinal views with a transverse diameter of 22.6 cm, an AP of 13.7 cm, and a longitudinal diameter of 15.2 cm. Estimated liver volume of $2,461.35 \text{ cm}^3$.

AP: anteroposterior; CLD: chronic liver disease; US: ultrasound.

Table 4. Morphologic US grayscale findings of the hepatic region in portal hypertension assessment

Description ^a	Dimension	Echotexture (homogeneous/heterogeneous)	Echogenicity	Atrophy/hypertrophy	Regeneration nodule	Lesion (yes/no)	Superficial pattern (regular/irregular)
Left lobe of the liver							
Ligamentum falciform, AP, mm							
Right lobe of the liver							
Gallbladder, volume L × AP × T, cm ³							
Gallbladder ^b							
Gallbladder wall thickness, mm							
Liver volume, L × AP × T, cm ³							
Right kidney							
Right kidney, volume, L × AP × T, cm ³							

^aThe venous ligament is used as an anatomical reference. ^bGallbladder: its content and the presence of lesions are assessed. L: longitudinal; AP: anteroposterior; T: transverse; US: ultrasound.

Morphologic grayscale US findings of the hepatic region in portal hypertension assessment

The examination is performed with grayscale US in supine decubitus and then in left lateral decubitus. It starts with the left hepatic lobe in sagittal projection (Figure 4A), then in transverse projection (Table 4) (Figure 4B). We assess the homogeneous or heterogeneous echotexture, echogenicity, the presence of atrophy or hypertrophy, regeneration nodules (Figure 4C), and lesions (Figure 4D). The abnormal liver pattern may be microgranular (less than 3 mm) or macrogranular (more than 3 mm), and the surface pattern regular or irregular/granular¹⁵ (Figure 4E-F). The venous and falciform ligaments are identified. The AP diameter (mm) of the falciform ligament is measured (Figure 4G). Right hepatic lobe assessment is continued (Figure 4H) with the same parameters as the left hepatic lobe.

We continue with the gallbladder, measuring its dimensions in the longitudinal, anteroposterior, and transverse diameters and determining its volume (cm³). Its contents, the presence of lesions, and its wall thickness (normal value 2-3 mm) are assessed. With the patient in the left oblique decubitus position, with a transverse projection and a subcostal approach, the

maximum transverse diameter of the left and right hepatic lobes (cm) and the maximum anteroposterior diameter are measured. In longitudinal projection, the maximum longitudinal diameter of the right lobe is measured, and the liver volume is determined¹⁰ (Figure 4I). The volume is calculated by multiplying these parameters and then multiplying the result by 0.52, which is the formula of an ellipsoid¹¹.

Mobility and lesions in the right hemidiaphragm are assessed. The pleural space is searched for an effusion, and the presence or absence of collections or lesions in the perihepatic, subhepatic, and subphrenic spaces are described.

Hemodynamic duplex US findings of the hepatic region in portal hypertension assessment

Examination starts in the left hepatic vein, determining the diameter (mm), flow direction (antegrade or retrograde), spectral morphology, flow velocity (cm/s), and the presence of a thrombus, indicating whether it is acute or chronic and benign or malignant (Table 5) (Figure 5A). We continue with the left portal vein and the hepatic artery and determine the same parameters.

Table 5. Hemodynamic duplex US findings of the hepatic region^a in portal hypertension assessment

Description	Diameter (mm)	Direction of flow (antegrade/retrograde)	Spectral morphology	Flow velocity (cm/s)	Thrombosis (yes/no)	Thrombus acute/chronic	Thrombus benign/malignant
Left hepatic vein							
Left portal vein							
Left hepatic artery ^b							
Main portal vein							
Main hepatic artery							
Right portal vein							
Middle hepatic vein							
Right hepatic vein							
Right hepatic artery							
Collateral pericholecystic circulation							
Intrahepatic arterio-portal shunt							
Collateral perihepatic circulation							
Umbilical vein recanalization							
Right renal artery ^b							
Right renal vein							

^aThe assessment is supplemented by liver elastography. ^bTo assess resistivity index (RI) and the pulsatility index (PI). US: ultrasound.

In the latter, we evaluate the RI (normal value 0.55 to 0.7)¹⁶ and PI (normal value 0.9 to 1)¹⁷. We continue with the main portal vein, determining diameter (mm), flow direction (antegrade or retrograde), spectral morphology, flow velocity (cm/s) (Figure 5B-C), the presence of a thrombus, indicating if it is acute or chronic, and benign (Figure 5D-E) or malignant (Figure 5F), and recanalization or cavernomatous transformation (Figure 5G-H). Then, the main hepatic artery is assessed using the same parameters, adding the RI (normal value: 0.55-0.77)¹⁶ and PI (normal value: 1)¹⁶ (Figure 5I).

The right portal vein and right and middle hepatic veins (Figure 6A-C) are assessed by measuring the diameter (mm), flow direction (antegrade or retrograde), spectral morphology, flow velocity (cm/s), and the presence of a thrombus, specifying if it is acute or chronic and benign or malignant. The right hepatic artery is next, with an assessment of the same parameters. The RI (normal value 0.55-0.77) and PI (normal value 1) are assessed¹⁶.

The assessment continues with the pericholecystic collateral circulation (Figure 6D), intrahepatic arterio-portal shunts, perihepatic collateral circulation (Figure 6E),

and through the falciform ligament, the recanalization of the umbilical vein (Figure 6F-G). We continue with the right renal artery and vein, measuring the same parameters: diameter (mm), flow direction (antegrade or retrograde), spectral morphology, flow velocity (cm/s), and the presence of a thrombus. In addition, RI (normal value < 0.7) and PI (normal value between 1.0 and 1.5) are measured in the right renal artery^{13,18}. The assessment is complemented with hepatic (Figure 6H) and splenic elastography (Figure 6I) to assess steatosis, inflammation, and/or stiffness¹⁸.

Morphologic grayscale US findings of the inframesocolic area in portal hypertension assessment

With the patient in the supine position, grayscale US is performed, starting with the left parietocolic gutter for ascitic fluid (Figures 7A, B, C), collateral circulation (Figures 7D, E, F), and lesions (Table 6A). The right parietocolic gutter and pelvis are examined for the same findings¹⁵.

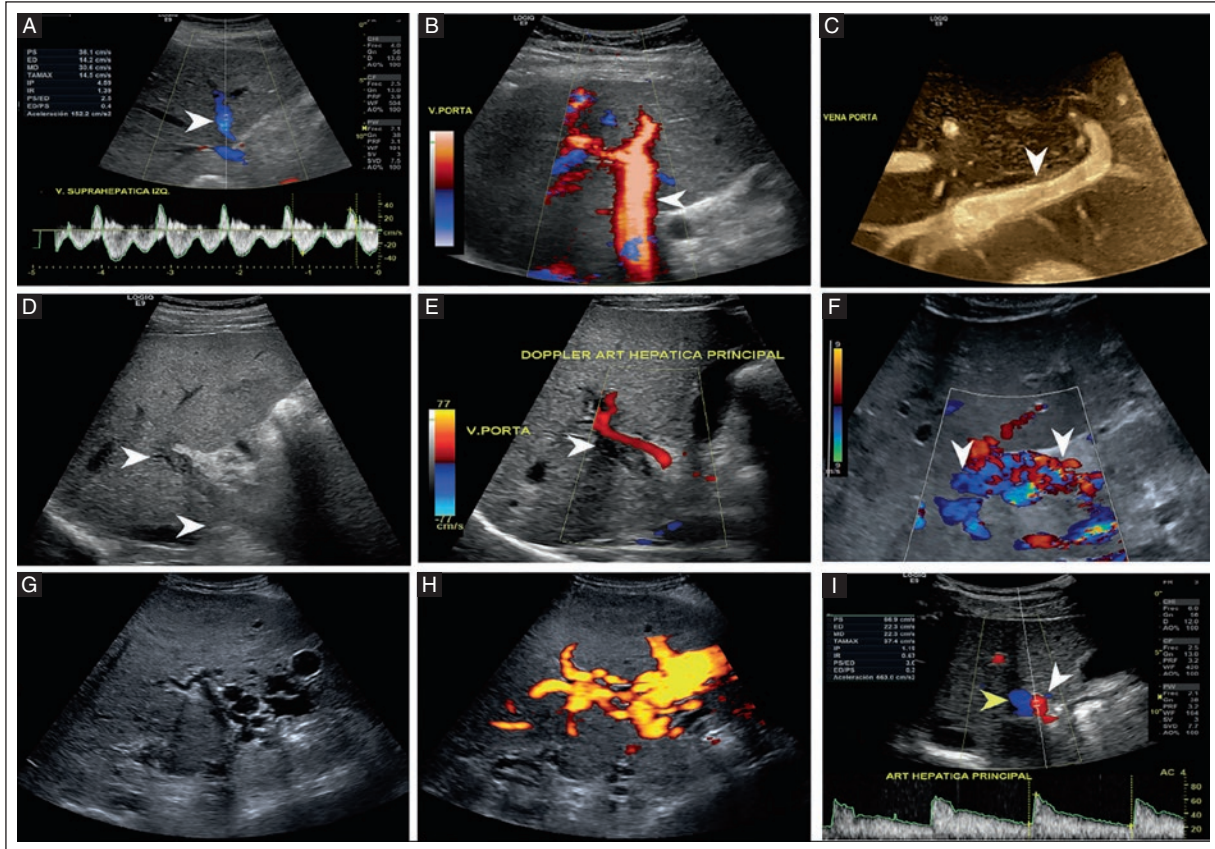


Figure 5. Hemodynamic US duplex findings of the hepatic region in portal hypertension assessment. **A:** a 39-year-old woman, subcostal transverse view of the liver US duplex showing the left hepatic vein with patency and normal spectral morphology. **B:** a 54-year-old woman with CLD, sagittal view with patient in left oblique position and intercostal approach with US power Doppler, showing portal vein dilated (white arrowhead) of 16 mm (not shown) with predominant hepato-petal flow. **C:** a 40-year-old woman, transverse view, subcostal with US B-flow of the porta hepatis with normal patency (white arrowhead). **D:** a 48-year-old man with idiopathic portal hypertension. **D:** grayscale US, sagittal view with patient in left oblique position and intercostal approach showing the main portal vein with endoluminal echogenic material along its entire course in relation to chronic thrombosis (white arrowheads). **E:** a color Doppler US sagittal view with patient in left oblique position and intercostal approach showing absent flow in the main portal vein (white arrowhead) and a compensatory increase in the main hepatic artery secondary to chronic portal vein thrombosis. **F:** a 28-year-old man with hepatocarcinoma. US color Doppler showing endoluminal echogenic material in the main portal vein (not shown) with intralesional flow (white arrowheads) in relation to a malignant portal vein thrombus. **G:** a 36-year-old woman with Budd-Chiari syndrome. **G:** grayscale US and **H:** US power Doppler transverse views showing multiple dilated, tortuous, periportal vessels in relation to cavernomatous transformation of the portal vein. **I:** a 40-year-old man with CLD, US duplex, showing hepatic artery (white arrowhead) with patency, spectral morphology, velocity, and normal IR and IP with hepatofugal flow (blue color) in the portal vein (yellow arrowhead).

US: ultrasound; CLD: chronic liver disease.

Hemodynamic duplex US findings of the inframesocolic area in portal hypertension assessment

The examination continues with duplex US to determine the presence of perirectal plexuses, describing their diameter, flow direction, spectral morphology, and flow velocity (Table 6B). We continue with the omental veins and retroperitoneal veins, evaluating the same parameters¹⁵.

CONCLUSION

This technical note proposes a comprehensive duplex US acquisition and analysis protocol of portal hypertension with the assessment of five regions: splenic, pancreatic, cardiac, hepatic, and inframesocolic. Radiologists must have a profound knowledge of the embryology, anatomy, hemodynamics, and pathophysiology of the portal system and splanchnic circulation to optimally and accurately assess the morphological and

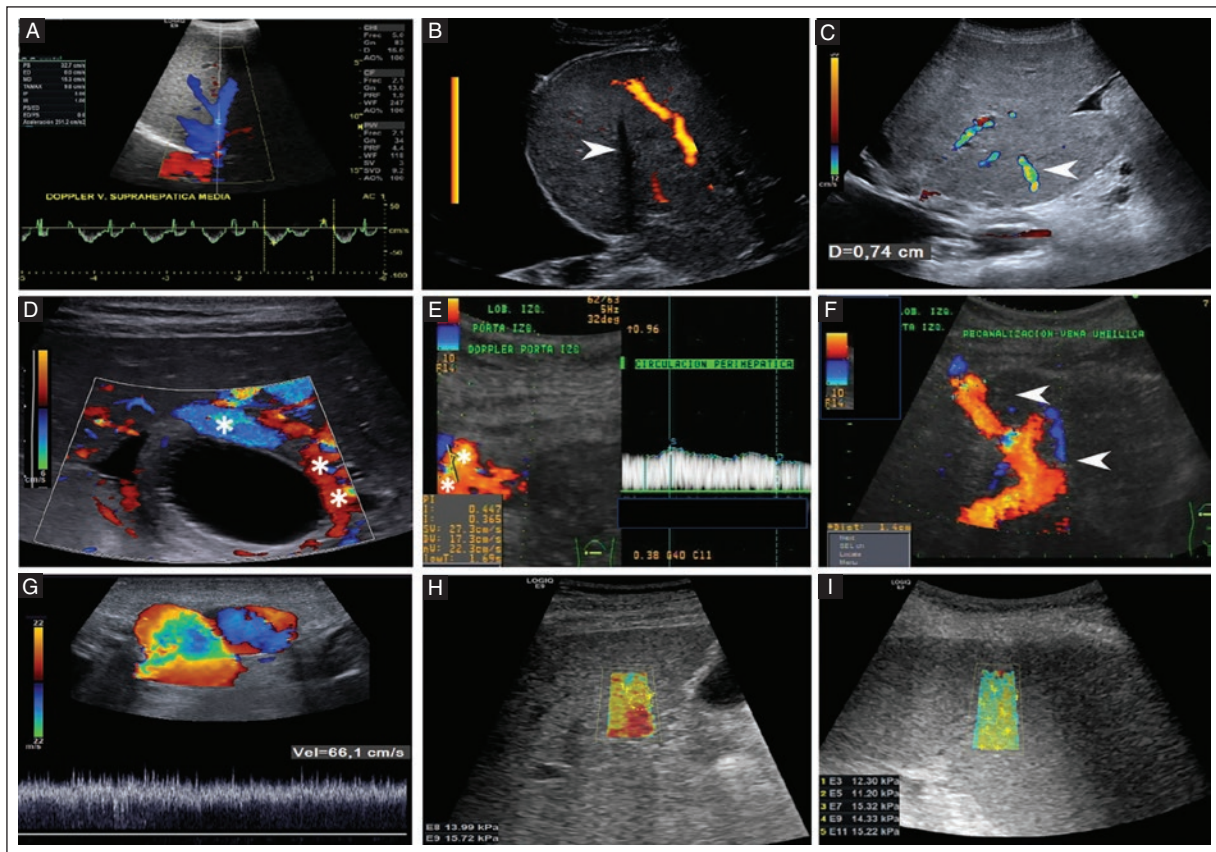


Figure 6. Hemodynamic US duplex findings of the hepatic region in portal hypertension assessment. **A:** a 32-year-old woman patient with US duplex showing the middle hepatic vein with patency, tetraphasic spectral morphology, and normal velocity. **B:** a 36-year-old woman with chronic Budd-Chiari syndrome; US power Doppler sagittal view of the right hepatic lobe showing the right hepatic vein (white arrowhead) with absent flow, secondary to chronic thrombosis and patency of the right portal vein with hepato-petal flow, with abundant fluid in the right pleural cavity. **C:** a color Doppler US sagittal view of the left hepatic lobe of the same patient showing severe hypertrophy of the caudate lobe and dilatation of its draining vein (white arrowhead) with a diameter of 7.4 mm (caliper not shown), perihepatic free fluid and in the right pleural cavity. **D:** a 58-year-old man with alcoholic liver disease. US color Doppler with significant pericholecystic collateral circulation (white asterisks). **E:** a 69-year-old woman, transverse view with US duplex showing collateral circulation in the wall and perihepatic area due to recanalization of the umbilical vein (asterisks) with a hepato-fugal velocity of 27.3 cm/s. **F:** a 69-year-old woman with CLD. Color Doppler US transverse view of the left lobe showing a 14 mm dilated vessel along the entire course of the falciform ligament in relation to recanalization of the umbilical vein (white arrowheads). **G:** US duplex with a high-resolution linear transducer in transverse view in the periumbilical region shows a periumbilical collateral circulation with dilated and tortuous vessels of 2.2 cm caliber (not shown) with severe hepatofugal flow with a velocity of 66.1 cm/s. **H:** a 69-year-old man with alcoholic liver disease. Oblique view with intercostal approach of the right hepatic lobe over segment V using ARFI elastography with two determinations of 13.9 and 15.7 kPa; the median after 12 determinations (not shown) was 12.2 kPa. Metavir score F4 = cirrhosis. **I:** a 72-year-old woman with CLD. A transverse approach to the spleen with ARFI elastography showing five measurements after 12 determinations (not shown) was 12.8 kPa, Metavir score F0 = normal.

US: ultrasound; CLD: chronic liver disease; kPa: kilopascals; ARFI: Acoustic Radiation Force Impulse.

hemodynamic imaging findings to confirm or rule out portal hypertension, defining the site of obstruction (pre-hepatic, intrahepatic or posthepatic), information that is essential for clinical management of the patient. Furthermore, duplex US examination is useful for patient follow-up and determining prognosis. It is widely available with no exposure to radiation and at low cost. Validation of this comprehensive duplex US acquisition and analysis protocol for portal hypertension requires

prospective studies in different hospital centers or vascular laboratories by radiologists with different levels of experience.

Acknowledgments

The authors thank Professor Ana M. Contreras-Navarro for her guidance in preparing and writing this scientific paper.

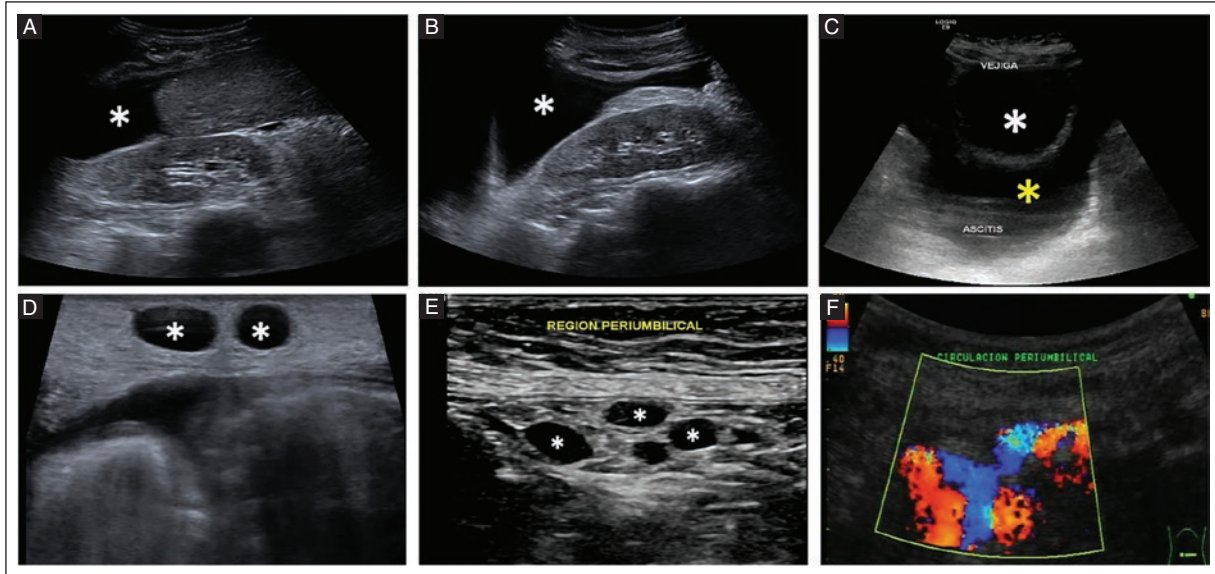


Figure 7. Grayscale US findings of the inframesocolic region in portal hypertension assessment. **A** and **B**: a 36-year-old woman with Budd-Chiari syndrome, longitudinal view on grayscale US in the right and left parietocolic gutter with free fluid in both gutters (asterisks). **C**: a 77-year-old woman with post-necrotic cirrhosis, grayscale US, transverse view showing the bladder (white asterisk) and abundant free fluid around the bladder (yellow asterisk). A 48-year-old man with alcoholic liver disease. **D-E**: grayscale US with a high-resolution linear transducer (10 MHz) showing multiple 8 to 10 mm periumbilical dilated vessels (white asterisks) in relation to the collateral circulation. **F**: color Doppler US with sectorial transducer (6 MHz) showing multiple dilated periumbilical vessels in relation to the collateral circulation.

US: ultrasound; CLD: chronic liver disease.

Table 6A. Morphologic grayscale US findings of the inframesocolic region in portal hypertension assessment

Description
Left paracolic gutter: describe ascitic fluid, collateral circulation or lesions, if present.
Right paracolic gutter: describe the ascitic fluid, collateral circulation or any lesions, if present.
Pelvic cavity: describe the ascitic fluid, collateral circulation or any lesions, if present.

US: ultrasound.

Table 6B. Hemodynamic duplex US findings of the inframesocolic region in the assessment of portal hypertension

Description	Diameter (mm)	Direction of flow (antegrade/retrograde)	Spectral morphology	Flow velocity (cm/s)
Perirectal plexus				
Omental veins				
Retroperitoneal veins				

US: ultrasound.

Funding

This research received no external funding.

Conflicts of interest

The authors declare that they have no conflicts of interest.

Ethical considerations

Protection of humans and animals. The authors declare that the procedures followed complied with the ethical standards of the responsible human experimentation committee and adhered to the World Medical Association and the Declaration of Helsinki.

Confidentiality, informed consent, and ethical approval. For the analysis of routinely obtained and anonymized clinical data, informed consent was not necessary.

Declaration on the use of artificial intelligence. The authors declare that no generative artificial intelligence was used in the writing of this manuscript.

REFERENCES

1. Garcia-Tsao G, Bosch J. Management of varices and variceal hemorrhage in cirrhosis. *N Engl J Med*. 2010;362(9):823-832. doi: 10.1056/NEJMr0901512.
2. Tsochatzis EA, Bosch J, Burroughs AK. Liver cirrhosis. *Lancet*. 2014;383(9930):1749-1761. doi: 10.1016/S0140-6736(14)60121-5.
3. de Franchis R, Bosch J, Garcia-Tsao G, Reiberger T, Ripoll C; Baveno VII Faculty. Baveno VII - Renewing consensus in portal hypertension. *J Hepatol*. 2022;76(4):959-974. doi: 10.1016/j.jhep.2021.12.022. Erratum in: *J Hepatol*. 2022;77(1):271. doi: 10.1016/j.jhep.2022.03.024.
4. Berzigotti A, Piscaglia F. Ultrasound in portal hypertension-part 1. *Ultraschall Med*. 2011;32(6):548-568; quiz 569-571. English, German. doi: 10.1055/s-0031-1281856.
5. Maruyama H, Yokosuka O. Ultrasonography for Noninvasive Assessment of Portal Hypertension. *Gut Liver*. 2017;11(4):464-473. doi: 10.5009/gnl16078.
6. Smith RE, Friedman AD, Murchison JA, Tanner SB, Smith PA, Dollar BT. Acute Life-Threatening Complications of Portal Hypertension: a Review of Pathophysiology, Incidence, Management, and Cost. *SN Compr Clin Med*. 2020;2:1628-1645. doi: 10.1007/s42399-020-00435-5.
7. Barr RG, Wilson SR, Rubens D, Garcia-Tsao G, Ferraioli G. Update to the Society of Radiologists in Ultrasound Liver Elastography Consensus Statement. *Radiology*. 2020;296(2):263-274. doi: 10.1148/radiol.2020.192437.
8. Elkrief L, Rautou PE, Ronot M, Lambert S, Dioguardi Burgio M, Francoz C, et al. Prospective comparison of spleen and liver stiffness by using shear-wave and transient elastography for detection of portal hypertension in cirrhosis. *Radiology*. 2015;275(2):589-598. doi: 10.1148/radiol.14141210.
9. Heo S, Lee SS, Choi SH, Kim DW, Park HJ, Kim SY, et al. CT Rule-in and Rule-out Criteria for Clinically Significant Portal Hypertension in Chronic Liver Disease. *Radiology*. 2023;309(1):e231208. doi: 10.1148/radiol.231208.
10. Kim DW, Ha J, Lee SS, Kwon JH, Kim NY, Sang YS, et al. Population-based and Personalized Reference Intervals for Liver and Spleen Volumes in Healthy Individuals and Those with Viral Hepatitis. *Radiology*. 2021;301(2):339-347. doi: 10.1148/radiol.2021204183.
11. Pampa-Saico S, Alexandru S, Pizarro-Sánchez MS, López-Picasso M, García Puente-Suárez L, Barba R, et al. Volumen renal total y función renal en pacientes nefrectomizados por neoplasias renales. *Nefrología* 2021;41(4):446-452. doi: 10.1016/j.nefro.2020.10.009.
12. Conangla-Planes M, Serres X, Persiva O, Agustín S. Diagnostic imaging of portal hypertension. *Radiology*. 2018;60(4):290-300. doi: 10.1016/j.rx.2017.12.010.
13. Tublin ME, Bude RO, Platt JF. The resistive index in renal Doppler sonography: where do we stand? *AJR Am J Roentgenol*. 2003;180(4):885-892. doi: 10.2214/ajr.180.4.1800885.
14. Cannella R, Giambelluca D, Pellegrinelli A, Cabassa P. Color Doppler Ultrasound in Portal Hypertension: A Closer Look at Left Gastric Vein Hemodynamics. *J Ultrasound Med*. 2021;40(1):7-14. doi: 10.1002/jum.15386.
15. Augustine A, John R, Simon B, Chandramohan A, Keshava SN. Imaging Approach to Portal Hypertension. *J Gastrointest Abdom Radiol ISGAR*. 2023;6(2):123-137. doi: 10.1055/s-0043-1764311.
16. McNaughton DA, Abu-Yousef MM. Doppler US of the liver made simple. *Radiographics*. 2011;31(1):161-188. doi: 10.1148/rg.311105093. Erratum in: *Radiographics*. 2011;31(3):904.
17. Noh MAE, Abd-Elmageed MK, Amer AAM, ELhamouly MS. Role of portal color Doppler ultrasonography as noninvasive predictive tool for esophageal varices in cirrhotic patients. *Egypt J Radiol Nucl Med*. 2022; 53(4):1-11. doi: 10.1186/s43055-021-00681-0.
18. Peltec A, Sporea I. Multiparametric ultrasound as a new concept of assessment of liver tissue damage. *World J Gastroenterol*. 2024;30(12):1663-1669. doi: 10.3748/wjg.v30.i12.1663.

Normal T2 relaxometry values of peripheral nerves on 3.0T MRI in healthy Mexican subjects: an exploratory study

Cynthia Castro-Teran¹ , Beatriz Elias-Perez*¹ , and Arturo Hernandez-Medina¹ 

Department of Magnetic Resonance, Angeles Lomas Hospital, Huixquilucan, State of Mexico, Mexico

ABSTRACT

T2 relaxometry in magnetic resonance imaging (MRI) provides quantitative information on peripheral nerves. This study aimed to determine the normal MRI 3.0T T2 relaxometry values of the ulnar, median, and sciatic peripheral nerves in healthy Mexican subjects. This cross-sectional study examined the T2 relaxation times and T2 maps in 3.0T MRI of four anatomical regions: the elbow at the level of the cubital tunnel to assess the ulnar nerve; the wrist at the level of the carpal tunnel to assess the median nerve and the right and left hip at the level of the piriformis muscles to assess the sciatic nerves of both hips. One hundred twenty peripheral nerves from 30 healthy Mexican volunteers were examined: 30 ulnar nerves, 30 median nerves, 30 right sciatic nerves, and 30 left sciatic nerves. The mean \pm SD T2 relaxation time of the ulnar nerve was 73.91 ms \pm 16.8 ms; of the median nerve, 58.8 ms \pm 9 ms; of the right sciatic nerve, 70.5 ms \pm 13.9 ms and of the left sciatic nerve, 70.2 ms \pm 17.2 ms. The T2 relaxometry values of the ulnar, median, and sciatic peripheral nerves averaged 59 to 74 ms. These values are comparable to normal reference values in other populations. This study is the first that establishes normal T2 relaxometry values in healthy Mexican subjects.

Keywords: Magnetic resonance imaging. Relaxometry. Peripheral nerves. Median nerve. Ulnar nerve. Sciatic nerve.

INTRODUCTION

Specific high-resolution T2-weighted magnetic resonance imaging (MRI) sequences have been used for the morphological study of nerves^{1,2}. The T2 relaxation time, which corresponds to the signal loss after a radio-frequency (RF) pulse follows an exponential, tissue-specific decay, describes the time in which transverse magnetization decreases to 37% of its initial value, allows separation of each component of the tissues³, and provides quantitative information about the relaxation properties and internal structure of the tissue.

Normal T2 relaxometry values of the peripheral median, ulnar, and sciatic nerves with a 3.0 Tesla (T) resonator average 35 to 85 milliseconds (ms)⁴⁻⁶. The T2 relaxation time may vary depending on age, sex, relaxometry sequence parameters with echo time interval, magic angle, RF field, receiver coil sensitivity, region of interest (ROI) measurement, hardware differences (receiver coils, RF channels), and magnet field strength (1.5T, 3.0T or 7.0T)^{3,7-10}.

Various conditions affecting the structure and composition of peripheral nerves are associated with an abnormal T2 relaxation time^{10,11}. The T2 relaxation time

*Corresponding author:

Beatriz Elias-Perez
E-mail: betyelias@hotmail.com

Received for publication: 04-02-2025

Accepted for publication: 19-03-2025

DOI: 10.24875/JMEXFRI.M25000105

Available online: 15-07-2025

J Mex Fed Radiol Imaging. 2025;4(2):125-130

www.JMeXFRI.com

2696-8444 / © 2025 Federación Mexicana de Radiología e Imagen, A.C. Published by Permanyer. This is an open access article under the CC BY-NC-ND (<https://creativecommons.org/licenses/by-nc-nd/4.0/>).

has been studied in the central nervous system, but there are few studies of the peripheral nerves². This study aimed to determine the normal 3.0T MRI T2 relaxometry values of the ulnar, median, and sciatic nerves in healthy Mexican subjects.

MATERIAL AND METHODS

This prospective cross-sectional study was conducted from May to November 2024 in the Department of Magnetic Resonance of the Hospital Angeles Lomas in Huixquilucan, State of Mexico, Mexico. We included healthy Mexican subjects aged 18 to 75. Individuals with contraindications for MRI, with suspected peripheral nerve damage on MRI, or with an incomplete MRI were excluded. Written informed consent was obtained, and the institutional ethics and research committees approved the study.

Study development and variables

Data on age, sex, weight, height, and body mass index (BMI) were collected. MRI T2 relaxation time and color T2 maps of four anatomical regions were obtained at the elbow at the level of the cubital tunnel to assess the ulnar nerve, at the wrist at the level of the carpal tunnel to assess the median nerve, and at the right and left hip at the level of the piriformis muscles to assess the sciatic nerves of both hips.

Imaging acquisition and analysis protocol

A 3.0T resonator (MAGNETOM Skyra, Siemens Healthineers, Erlangen, Germany) was used. The MRI T2 relaxation time protocol is described in table 1. Images of the ulnar nerve were acquired with an Ultraflex coil with 18 RF channels. Axial T2-weighted multiple echo data image combination (MEDIC) sequences (TR/TE 575/22 ms) were used for anatomical assessment. Images of the median nerve were acquired at the wrist with a 16-channel RF hand/wrist coil. An isotropic coronal T2-weighted MEDIC sequence (TR/TE 28/15 ms) was used for anatomical assessment. Images of the sciatic nerve were acquired with a 30-channel RF body coil. An isotropic coronal T2-weighted MEDIC sequence (TR/TE 23/13 ms) was used to localize the right and left sciatic nerves.

The area of spin-echo multi-echo sequences (T2 relaxometry) was determined with the anatomical T2-weighted sequences, in which 11 slices, each with 12 images with different echo time weighting, were

selected. These images were automatically processed by the equipment, providing two image series: one in grayscale and one in color (T2 map), which were merged to determine the anatomical region. Once the analyzed nerve was located, a ROI of 2-2.5 cubic millimeters was manually placed.

Fat suppression was performed in the T2 sequences to define the ROI and rule out compressive pathology of the peripheral nerves. ROI selection and T2 relaxation time were determined with syngo.MR software (Siemens Healthineers, Erlangen, Germany). The mean relaxation time of all pixels within the ROI was determined.

Statistical analysis

The data matrix was acquired with the quantitative T2 relaxation time of each peripheral nerve. The Shapiro-Wilk normality test was performed with a $p < 0.05$ and showed a non-normal distribution of T2 relaxation time for the ulnar, median, and sciatic nerves. The median and interquartile range (IQR) were used as measures of central tendency for quantitative T2 relaxation times. Inferential analysis between age and T2 relaxation time of each nerve analyzed was performed with Pearson's correlation; a p value < 0.05 was considered statistically significant for the tests. Rkward v0.8.0 software (Friedrichsmeier, 2024)¹² was used for the analysis.

RESULTS

Thirty healthy Mexican subjects and a total of 120 peripheral nerves were assessed with T2 relaxometry and color T2 maps on 3.0T MRI: 30 ulnar nerves, 30 median nerves, 30 right sciatic nerves, and 30 left sciatic nerves. The age, sex, weight, height, and BMI of the participants are listed in supplementary table 1. The mean age was 41 ± 14.2 years (min 21, max 74 years) with a predominance of women ($n = 18, 60.0\%$). Mean weight was 75.9 ± 14.4 kg, height 163.6 ± 11.5 cm and BMI 28.3 ± 4.2 . The T2 relaxation times of the ulnar, median, right and left sciatic nerves are reported for each patient.

Table 2 shows a T2 relaxation time for the ulnar nerve of 73.91 ± 16.8 ms; for the median nerve, 58.8 ± 9.0 ms; the right sciatic nerve, 70.5 ± 13.9 ms, and the left sciatic nerve, 70.2 ± 17.2 ms. Figure 1 at the level of the cubital tunnel shows the ulnar nerve with homogeneous hyperintensity with normal-appearing hypointense fascicles and a T2 relaxation time of 77.75 ms. Figure 2 at the level of the carpal tunnel shows the median nerve with homogeneous hyperintensity with normal-appearing

Table 1. 3.0T MRI T2 relaxation time protocol of the ulnar, median, and sciatic nerves of healthy Mexican subjects

Region	Peripheral nerve	Sequence	Fat saturation	FOV (mm)	Matrix	TR (ms)	TE (ms)	Slice thickness/gap (mm)
Elbow ^a	Ulnar	T2-weighted axial	Yes	90*90	240*320	575	22	2.5/0.3
Elbow ^a		T2 map SE ME axial	Yes	90*90	169*192	2400	12 echos, 10 ms each (10-120)	3.0/6.0
Wrist ^b	Median	T2-weighted coronal iso	Yes	100*100	233*256	128	15	0.4/0.0
Wrist ^b		T2 map SE ME axial	Yes	90*90	169*192	2400	12 echos, 10 ms each (10-120)	3.0/6.0
Hip ^c	Sciatic	T2-weighted coronal iso	Yes	250*400	360*576	23	13	1.0/0.0
Hip ^c		T2 map SE ME axial	Yes	159*159	169*192	2400	12 echos, 10 ms each (10-120)	3.5/7.0

^aAt the cubital tunnel level; ^bAt the carpal tunnel level; ^cAt the piriformis muscles. T:tesla; MRI: magnetic resonance imaging; T2- weighted image; SE: spin-echo; ME: multi-echo; FOV: field-of-view; T2- weighted image; TR: repetition time; TE: echo time; ms: milliseconds; mm: millimeters.

Table 2. 3.0T MRI T2 relaxation time of the ulnar, median, and sciatic nerves of healthy Mexican subjects

Description	Mean ± SD	Minimum	Median	Maximum	Q1	Q3	IQR
Ulnar nerve, ms	73.91 ± 16.8	46	73.9	117	62.2	85.0	22.7
Median nerve, ms	58.8 ± 9.0	44	58.8	77	52.2	66.0	13.7
Right sciatic nerve, ms	70.5 ± 13.9	43	70.5	103	61.2	79.2	18.0
Left sciatic nerve, ms	70.2 ± 17.2	32	66	107	61.0	86.0	25.0

T: tesla; MRI: magnetic resonance imaging; SD: Standard Deviation; Q1: first quartile; Q3: third quartile; IQR: interquartile range; ms: milliseconds; T2- weighted image.

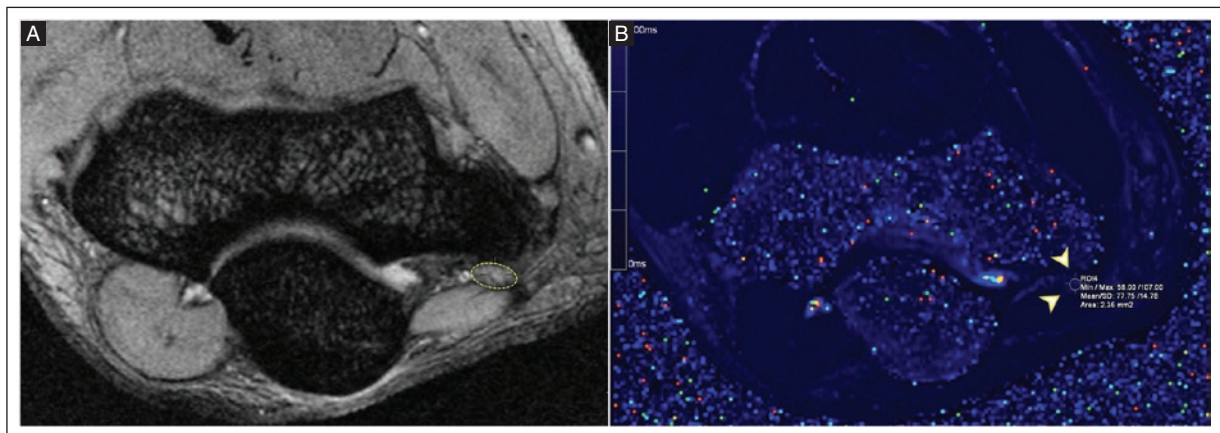


Figure 1. Axial MRI at the level of the cubital tunnel. **A:** T2 relaxometry multi-echo sequence (TR = 2400 ms; TE = 12 ms) shows homogeneous hyperintensity with normal appearing hypointense fascicles of the ulnar nerve (yellow dashed circle). **B:** T2 relaxometry color map with ROI of 2.36 mm² in the ulnar nerve with a T2 relaxation time mean of 77.75 ms (yellow arrowheads).

ME: multi-echo; mm²: square millimeters; MRI: magnetic resonance imaging; ms: milliseconds; ROI: region of interest; SE: spin echo; T2- weighted image; TE: echo time; TR: repetition time.

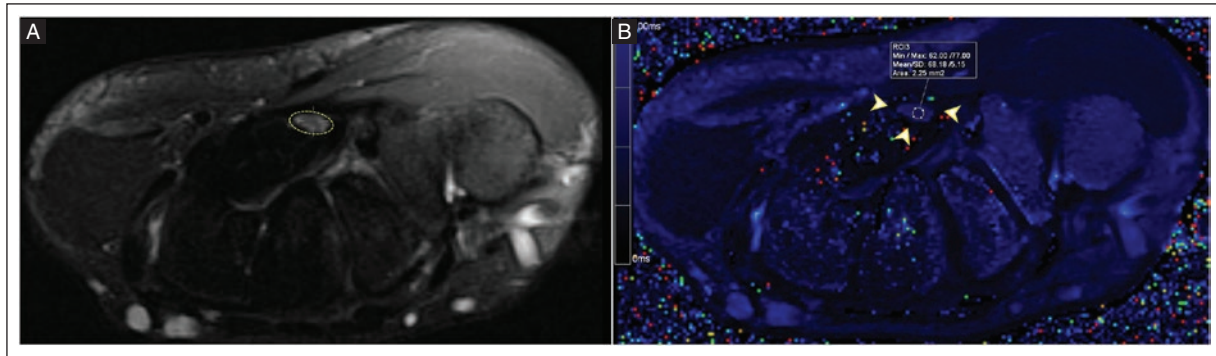


Figure 2. Axial MRI at the level of the carpal tunnel. **A:** T2 relaxometry multi-echo sequence (TR = 2400 ms; TE = 12 ms) shows homogeneous hyperintensity with normal appearance hypointense fascicles in the median nerve (yellow dashed circle). **B:** T2 relaxometry color map with a ROI of 2.25 mm² in the median nerve with a T2 relaxation time mean of 68.18 ms (yellow arrowheads).

ME: multi-echo; mm²: square millimeters; MRI: magnetic resonance imaging; ms: milliseconds; ROI: region of interest; SE: spin echo; T2- weighted image; TE: echo time; TR: repetition time.

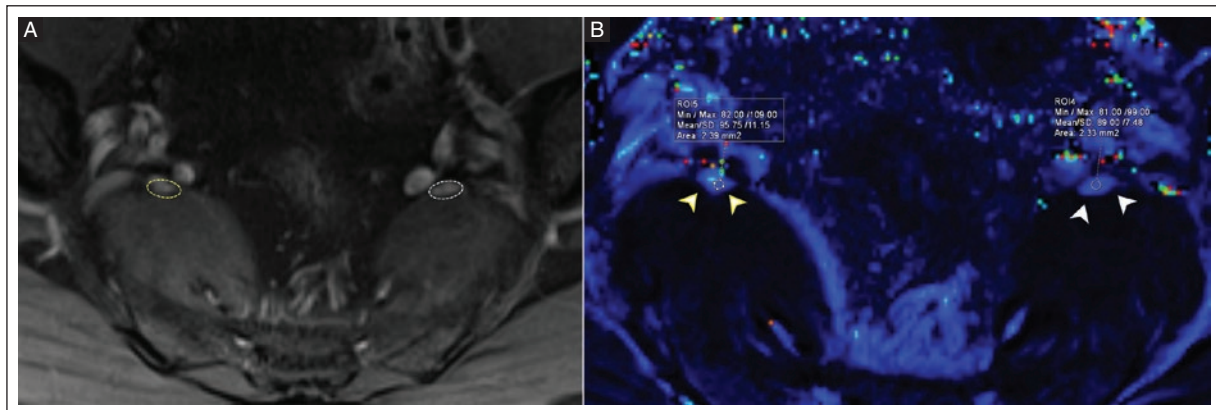


Figure 3. Axial MRI at the level of the piriformis muscles. **A:** T2 relaxometry multi-echo sequence (TR = 2400 ms; TE = 10 ms) showing the right (yellow dashed circle) and left (white dashed circle) sciatic nerve with homogeneous hyperintensity and normal appearing hypointense fascicles. **B:** T2 relaxometry color map showing a ROI of 2.39 mm² in the right sciatic nerve with a mean 97.75 ms T2 relaxation time (yellow arrowheads) and a 2.33 mm² ROI in the left sciatic nerve with a mean 89 ms T2 relaxation time (white arrowheads).

ME: multi-echo; mm²: square millimeters; MRI: magnetic resonance imaging; ms: milliseconds; ROI: region of interest; SE: spin echo; T2- weighted image; TE: echo time; TR: repetition time.

hypointense fascicles and a T2 relaxation time of 68.18 ms. Figure 3, at the level of the piriformis muscles, shows the right and left sciatic nerves with homogeneous hyperintensity, hypointense fascicles of normal aspect and a T2 relaxation time of 97.75 ms for the right sciatic nerve and 89 ms for the left sciatic nerve.

The linear regression showed a weak correlation between the participant's age and the T2 relaxation times of the ulnar nerve, median nerve, and sciatic nerve (Figure 4). For the ulnar nerve and the median nerve, the correlation was positive when the T2 relaxation times increased with increasing age. The sciatic

nerve, analyzed bilaterally (n = 60), showed a significant negative linear correlation ($p = 0.025$); as age increased, T2 relaxation times decreased.

DISCUSSION

In our study, the T2 relaxometry values on 3.0T MRI of the ulnar, median, and sciatic nerves were in a mean range of 59 to 74 ms. These values are comparable to normal reference values in other populations. This study is the first that determines normal T2 relaxometry values in healthy Mexican subjects.

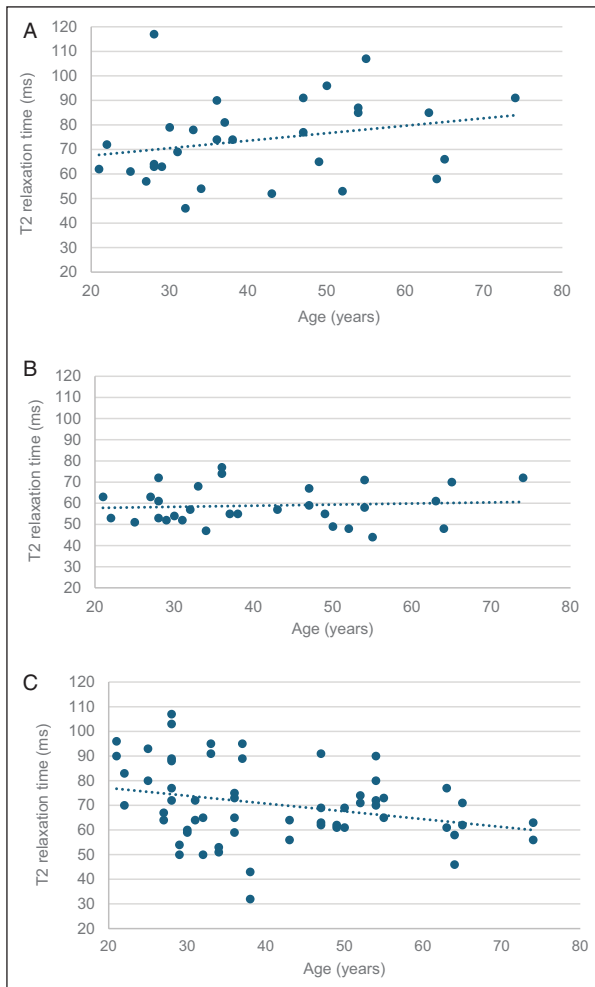


Figure 4. Scatter plots showing the correlation between the age of each patient and the T2 relaxation time. **A:** ulnar nerve with a weak positive correlation ($r = 0.08$, $p = 0.66$), **B:** median nerve with a weak positive correlation ($r = 0.26$, $p = 0.16$), **C:** sciatic nerve with a significant negative correlation ($r = -0.28$, $p = 0.026$).

ms: milliseconds; T2- weighted image.

The assessment of neuropathies by MRI is usually based on qualitative findings. Reports of quantitative assessments of peripheral nerves by T2 relaxometry are scarce^{1,4-7,11,13}. Normal T2 relaxation times of peripheral nerves average 35 to 85 ms. Kronlage et al.⁴ reported in German subjects, a median nerve mean value of 69.58 ± 7.00 ms; a mean value for the ulnar nerve of 75.30 ± 10.19 ms, and a mean value for the sciatic nerve of 70.85 ± 4.91 ms. Preisner et al.⁵ reported 64.54 ± 8.2 ms for the sciatic nerve in German patients. Gambarota et al.⁶ reported a mean T2 relaxation time of 35.5 ± 2.8 ms for the median nerve in Swedish subjects. Cha et al.¹⁴ showed the T2 relaxation time

variability of the median nerve in healthy subjects according to the level of the carpal tunnel where the examination is performed: the distal radioulnar carpal tunnel was 44.0 ms (40.4-47.6), the proximal carpal tunnel, 41.8 ms (36.8-46.9), and the distal carpal tunnel, 41.8 ms (36.8-46.9). In our study, the ulnar, median and sciatic nerves were examined with a 3.0T MRI. This resulted in a mean T2 relaxation time for the ulnar nerve of 73.91 ± 16.8 ms; for the median nerve 58.8 ± 9.0 ms; for the right sciatic nerve 70.5 ± 13.9 ms, and for the left sciatic nerve 70.2 ± 17.2 ms. These values are comparable to normal reference values of other populations. The T2 relaxometry values of the ulnar, median, and sciatic peripheral nerves in our study can be considered normal values in healthy Mexican individuals.

The inhomogeneity of the magnetic field must be considered. Also, the different providers and programs that process the images may result in variable T2 relaxation time quantitative values. The T2 relaxation time of the nerve varies depending on the magnetic field strength. It decreases with increasing magnetic field strength. Since the magnetic field gradients increase with the magnetic field strength of the MRI, the dephasing effect increases at a higher field strength. However, the advantage is that sequences with the shortest possible TE can take full advantage of the increased signal-to-noise ratio and better define the image⁷. Gambarota et al.⁷ in Swedish individuals reported T2 relaxometry values of the median nerve with different magnetic field strengths. The results were 50 ms in a 1.5T MRI resonator⁸; a mean of 35 ms in a 3.0T MRI resonator, and 20 ms in a 7.0T MRI resonator⁶. On the other hand, T2 relaxometry time was reported as a reproducible and reliable method⁵. In our study, only a 3.0T MRI resonator was used, so our results in Mexican subjects only apply to this magnetic field strength.

A correlation between T2 relaxations time and age has not been defined^{7,13}. Kronlage et al.¹³ in a study of 60 German healthy subjects evaluated 3.0T MRI T2 relaxation of the median, ulnar, and sciatic nerves. They found a significant correlation with height ($r = 0.28$, $p = 0.04$), weight ($r = 0.40$, $p = 0.002$), and body mass index ($r = 0.35$, $p = 0.008$), but not with age ($r = 0.23$, $p = 0.09$). We found a weak correlation between age and T2 relaxation time. For the ulnar and the median nerve, the correlation was positive, and T2 relaxation time increased with increasing age. The sciatic nerve had a significant negative linear correlation ($p=0.025$) as T2 relaxation times decreased with increasing age. There are insufficient data to establish a correlation between age and T2 relaxation time.

The strengths of the study relate to the imaging modality and the study protocol for determining the T2 relaxation time, making it reproducible. The weaknesses of the study are related to the sample size and the fact that only a 3.0T MRI scanner was used.

CONCLUSION

In our study, 3.0T MRI T2 relaxometry values of the ulnar, median, and sciatic peripheral nerves in healthy Mexican subjects were comparable to normal values in other populations. We believe that the T2 relaxometry values of the examined peripheral nerves in our exploratory study can be considered normal values in healthy Mexican subjects. Further studies with a larger population and different magnetic field strengths are needed to confirm the consistency of the values considered normal in peripheral nerves.

Acknowledgments

The authors thank Professor Ana M. Contreras-Navarro for her guidance in preparing and writing this scientific paper. This original research in the Radiology Specialty field was an awarded thesis at the Tercera Convocatoria Nacional 2024-2025 "Las Mejores Tesis para Publicar en el JMeXFRI".

Funding

This research received no external funding.

Conflicts of interest

The authors declare no conflicts of interest.

Ethical considerations

Protection of humans and animals. The authors declare that the procedures followed complied with the ethical standards of the responsible human experimentation committee and adhered to the World Medical Association and the Declaration of Helsinki.

The procedures were approved by the institutional Ethics Committee.





Confidentiality, informed consent, and ethical approval. The authors have followed their institution's confidentiality protocols, obtained informed consent from patients, and received approval from the Ethics Committee. The SAGER guidelines were followed according to the nature of the study.

Declaration on the use of artificial intelligence. The authors declare that no generative artificial intelligence was used in the writing of this manuscript.

REFERENCES

1. Preisner F, Behnisch R, Schwehr V, Godel T, Schwarz D, Foesleitner O, et al. Quantitative MR-neurography at 3.0T: Inter-scanner reproducibility. *Front Neurosci.* 2022;16:817316. doi:10.3389/fnins.2022.817316.
2. Carneiro AAO, Vilela GR, Araujo DB de, Baffa O. MRI relaxometry: methods and applications. *Braz J Phys.* 2006;36(1a):9-15. doi:10.1590/S0103-97332006000100005.
3. Bojorquez JZ, Bricq S, Acquitter C, Brunotte F, Walker PM, Lalande A. What are normal relaxation times of tissues at 3 T? *Magn Reson Imaging.* 2017;35(2016):69-80. doi: 10.1016/j.mri.2016.08.021.
4. Kronlage M, Schwehr V, Schwarz D, Godel T, Heiland S, Bendszus M, et al. Magnetic resonance neurography: normal values and demographic determinants of nerve caliber and T2 relaxometry in 60 healthy individuals. *Clin Neuroradiol.* 2019;29(1):19-26. doi:10.1007/s00062-017-0633-5.
5. Preisner F, Behnisch R, Foesleitner O, Schwarz D, Wehrstein M, Meredig H, et al. Reliability and reproducibility of sciatic nerve magnetization transfer imaging and T2 relaxometry. *Eur Radiol.* 2021;31(12):9120-9130. doi:10.1007/s00330-021-08072-9.
6. Gambarota G, Veltien A, Klomp D, Van Alfen N, Mulken RV, Heerschap A. Magnetic resonance imaging and T2 relaxometry of human median nerve at 7 Tesla. *Muscle Nerve.* 2007;36(3):368-373. doi:10.1002/mus.20826.
7. Gambarota G. T2 relaxometry of human median nerve. *Semin Musculoskelet Radiol.* 2009;13(1):24-28. doi:10.1055/s-0029-1202242.
8. Chappell KE, Robson MD, Stonebridge-Foster A, Glover A, Allsop JM, Williams AD, et al. Magic angle effects in MR neurography. *AJNR Am J Neuroradiol.* 2004;25(3):431-440.
9. Hofstadler B, Bäumer P, Schwarz D, Kronlage M, Heiland S, Bendszus M, et al. MR neurography: Normative values in correlation to demographic determinants in children and adolescents. *Clin Neuroradiol.* 2020;30(4):671-677. doi:10.1007/s00062-019-00834-9.
10. Giannini JE, Franco LP, Montalba ZC, López PD, Astudillo AC. Magnetic resonance neurography: technical aspects and clinical applications. *Rev Chil Radiol.* 2021;27(2):88-103. doi:10.4067/S0717-93082021000200088.
11. Wang D, Wang C, Duan X, Yang Z, Bai Z, Hu H, et al. MR T2 value of the tibial nerve can be used as a potential non-invasive and quantitative biomarker for the diagnosis of diabetic peripheral neuropathy. *Eur Radiol.* 2018;28(3):1234-1241. doi:10.1007/s00330-017-5043-1.
12. Friedrichsmeier, T and the RKWard Team (2024). RKWard: Graphical interface to the statistical language R. Version 0.8.0. <https://rkwart.kde.org>.
13. Kronlage M, Bäumer P, Pitarokoiili K, Schwarz D, Schwehr V, Godel T, et al. Large coverage MR neurography in CIDP: diagnostic accuracy and electrophysiological correlation. *J Neurol.* 2017;264(7):1434-1443. doi: 10.1007/s00415-017-8543-7.
14. Cha JG, Han JK, Im SB, Kang SJ. Median nerve T2 assessment in the wrist joints: preliminary study in patients with carpal tunnel syndrome and healthy volunteers. *J Magn Reson Imaging.* 2014;40(4):789-795. doi: 10.1002/jmri.24448.

Multimodality imaging with US, CT and MRCP for diagnosing atypical Lemmel syndrome: a case report

Roberto Hernandez-Juarez^{1,2*} , Edgar R. Austria-Franco¹ , Mario R. Prada-Bonilla¹ ,
and Asael G. Flores-Mata¹ 

¹Department of Radiology and Imaging, Mexico Angeles Hospital; ²Mexican Faculty of Medicine, La Salle University, Mexico City, Mexico

ABSTRACT

Lemmel syndrome is a rare cause of obstructive jaundice caused by extrinsic compression of the common bile duct by a periampullary duodenal diverticulum (PAD). This case report describes Lemmel syndrome in a 71-year-old woman with abdominal pain and jaundice due to a PAD with a completely intradiverticular major papilla. Abdominal ultrasound (US) revealed a distended gallbladder with gallstones and wall thickening with no evidence of an obstructive mass. Computed tomography (CT) revealed a duodenal diverticulum with mixed contents, causing extrinsic compression of the common bile duct. 3.0T magnetic resonance cholangiopancreatography (MRCP) confirmed the intradiverticular location of the biliary and pancreatic ducts. Endoscopic retrograde cholangiopancreatography (ERCP) was performed with sphincterotomy and biliary stenting. The procedure decompressed the biliary tree, resolved the obstruction and inflammatory process, and resulted in a favorable clinical recovery. This presentation is unique due to the intradiverticular location of the biliary and pancreatic ducts with no tumor-related findings. This case report provides diagnostic evidence of a rare anatomic variant, classified as type I Lemmel syndrome according to the both Boix and Li-Tanaka classifications. It highlights the role of non-invasive radiologic techniques in evaluating atypical biliopancreatic disorders. It is reported for educational purposes.

Keywords: Lemmel syndrome. Acute cholangitis. Intradiverticular papillary obstruction. Periampullary duodenal diverticulum. Case report.

INTRODUCTION

Lemmel syndrome was first described by Gerhard Lemmel in 1934, as a rare cause of obstructive jaundice resulting from extrinsic compression of the common bile duct by a periampullary duodenal diverticulum (PAD)¹⁻³. This condition is more common in women (70%), with a mean age at diagnosis of 70 years^{2,3}. PAD prevalence is between 5% and 33%, based on ERCP series⁴. PAD can distort the anatomy of the Vater

papilla, cause clinical symptoms in about 5% of cases, and increase the risk of choledocholithiasis even after cholecystectomy²⁻⁶. Clinical manifestations include jaundice, abdominal pain, and complications such as cholangitis or pancreatitis^{2,3,5}.

Imaging techniques, abdominal ultrasound (US), computed tomography (CT), and magnetic resonance cholangiopancreatography (MRCP), play a key role in diagnosis because they accurately identify PAD and its anatomical relationship with the bile duct^{1,5,7-9}.

*Corresponding author:

Roberto Hernandez-Juarez
E-mail: dr.robertto2021@gmail.com

Received for publication: 25-03-2024

Accepted for publication: 14-05-2025

DOI: 10.24875/JMEXFRI.24000012

Available online: 15-07-2025

J Mex Fed Radiol Imaging. 2025;4(2):131-136

www.JMeXFRI.com

2696-8444 / © 2025 Federación Mexicana de Radiología e Imagen, A.C. Published by Permanyer. This is an open access article under the CC BY-NC-ND (<https://creativecommons.org/licenses/by-nc-nd/4.0/>).

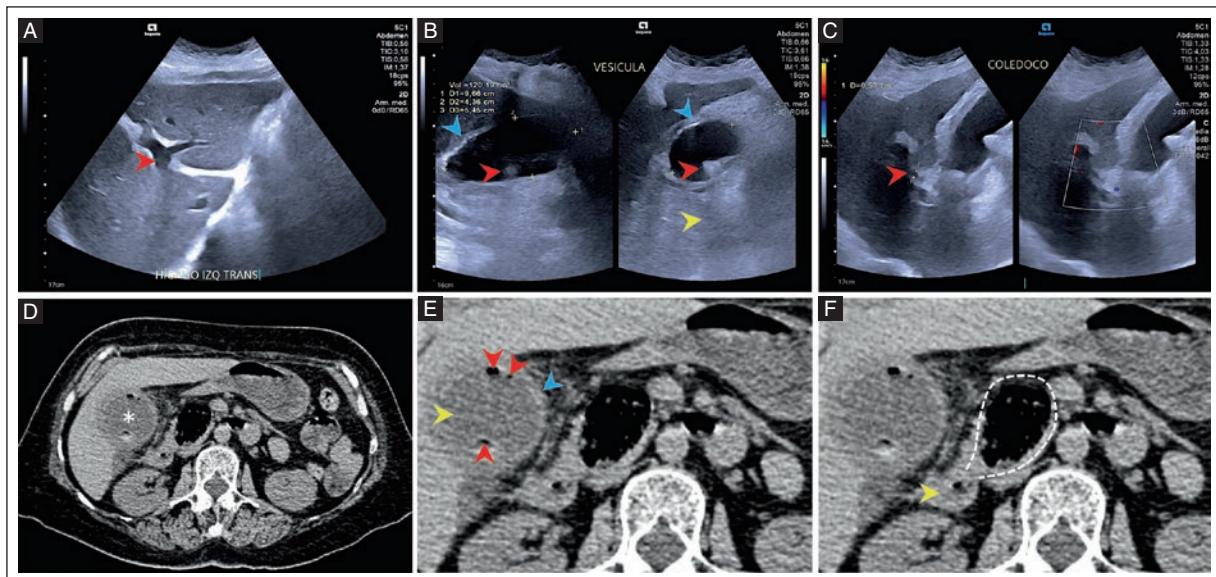


Figure 1. A 71-year-old woman with abdominal pain and jaundice diagnosed with Lemmel syndrome. **A:** grayscale US, transverse view of the left lobe of the liver showing intrahepatic bile duct dilatation (red arrowhead). **B:** grayscale US in split-screen mode with longitudinal and transverse views of a dilated gallbladder (9.6 × 4.6 × 5.4 cm, calculated volume of 120.2 cm³) with wall thickening (blue arrowheads) and hyperechoic images (red arrowheads) causing posterior acoustic shadowing (yellow arrowhead). **C:** grayscale US and color Doppler in split-screen mode with a longitudinal view of the common bile duct (red arrowhead) with a 5.3 mm diameter in its retroduodenal segment. **D:** non-contrast CT, axial view soft tissue window showing gallbladder enlargement (asterisk). **E:** non-contrast CT, axial view, soft tissue window shows gallbladder wall thickening (blue arrowhead), fluid content (yellow arrowhead), and gas (red arrowheads). **F:** non-contrast CT, axial view, soft tissue window shows a sac-like formation (dashed line) with food content and gas, originating from the second segment of the duodenum (yellow arrowhead). CT: computed tomography; US: ultrasound.

Despite advances in imaging, Lemmel syndrome is a diagnostic challenge due to its non-specific presentation and overlapping with other benign or malignant causes of biliary obstruction⁷⁻⁹.

PAD classifications, such as those by Boix¹⁰ and Li-Tanaka⁵, correlate the characteristics of the diverticulum during endoscopic retrograde cholangiopancreatography (ERCP)^{2-5,9,10}. There is no consensus on the optimal diagnostic or therapeutic approach; systematic studies are few, and most publications are case reports based on individual experience. This case report of a 71-year-old woman with abdominal pain and jaundice due to PAD with a completely intradiverticular major papilla, classified as type I according to the Boix-Li-Tanaka classification, highlights the value of diagnostic imaging based on Lemmel syndrome radiological findings. It focuses on the usefulness of MRCP and CT as non-invasive diagnostic tools in patients with non-neoplastic obstructive jaundice.

CLINICAL CASE DESCRIPTION

A 71-year-old woman diagnosed with diabetes mellitus came to the emergency department with severe

abdominal pain radiating to the right upper quadrant, accompanied by nausea and vomiting. On physical examination, her vital signs were normal, and she had scleral and skin jaundice. The abdomen was soft and compressible but tender on deep palpation in the right upper quadrant, with a positive Murphy's sign. Bowel sounds were normal. There were no masses or organomegaly, and no signs of peritonitis. Laboratory results were a C-reactive protein of 133 mg/L (normal: 0.2-0.9 mg/L), leukocytes of 12.68 × 10⁹/L (normal: 4-10 × 10⁹/L), total bilirubin of 3.93 mg/dL (normal: 0.4-1.9 mg/dL), alkaline phosphatase of 80 U/L (normal: 39-99 U/L), AST of 38 U/L (normal: 12-42 U/L), serum amylase of 102 U/L (normal: 38-149 U/L), and a serum procalcitonin of 0.4 ng/mL (normal: < 0.1-0.5 ng/mL).

Imaging findings

Abdominal US examination (ACUSON Sequoia™, Siemens Inc., Forchheim, Germany) showed a distended gallbladder (120.2 cc) with wall thickening and hyperechoic images with posterior acoustic shadowing suggestive of cholelithiasis, and a reduction in the

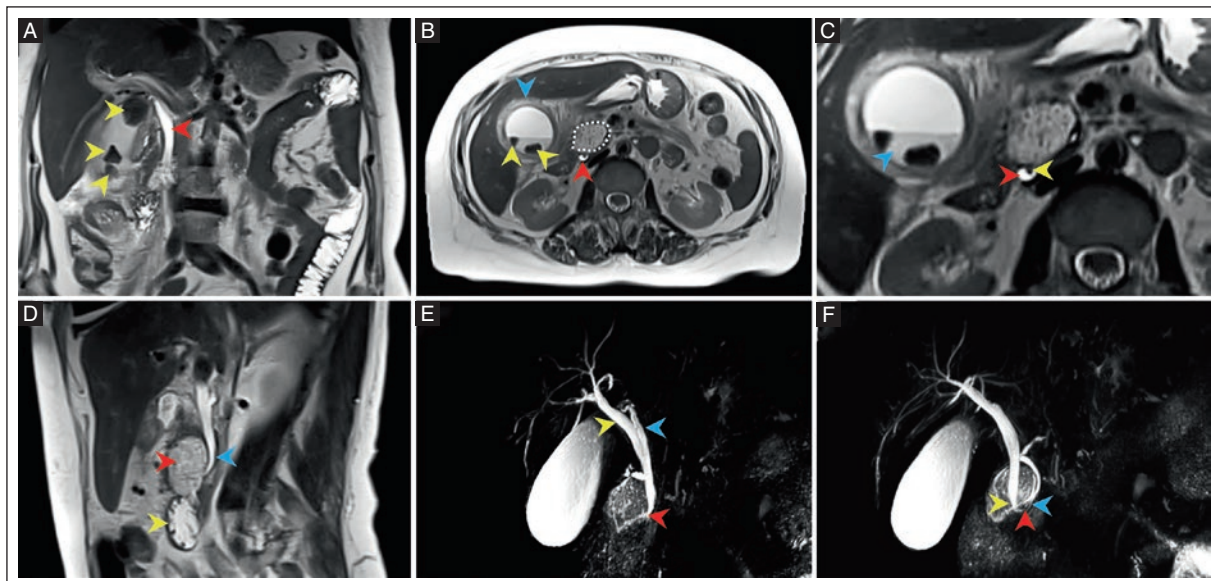


Figure 2. 3.0T MRI of a 71-year-old woman with abdominal pain and jaundice diagnosed with Lemmel syndrome. **A:** coronal T2-weighted HASTE view shows a distended gallbladder with hypointense areas suggestive of gallstones (yellow arrowheads) and proximal common bile duct dilatation (red arrowhead). **B:** axial T2-weighted HASTE view shows a distended gallbladder with wall thickening (blue arrowhead), a fluid level and intraluminal hypointense images consistent with gallstones (yellow arrowheads). A saccular formation (dashed line) is seen exerting a mass effect on the distal common bile duct (red arrowhead). **C:** axial T2-weighted HASTE view shows a fluid level with biliary sludge (blue arrowhead), a distal common bile duct segment (red arrowhead), and an intraductal microstone (yellow arrowhead). **D:** sagittal T2-weighted HASTE view shows a saccular image (red arrowhead) arising from the second segment of the duodenum (yellow arrowhead) compressing the distal common bile duct (blue arrowhead). **E:** 3D MIP reconstruction shows a saccular formation compressing both the common bile duct and the pancreatic duct (red arrowhead) and dilatation of the common hepatic duct (yellow arrowhead) and the cystic duct (blue arrowhead). **F:** a 3D MIP reconstruction shows compression of the common bile duct (yellow arrowhead) and the pancreatic duct (blue arrowhead). The Vater papilla is within the diverticulum (red arrowhead). The diagnosis was Lemmel syndrome, type I PAD, according to the Boix and Li-Tanaka classifications.

3.0 T: 3 Tesla; 3D MIP: three-dimensional maximum intensity projection; HASTE: Half-Fourier Acquisition Single-shot Turbo Spin Echo; MRI: magnetic resonance imaging; PAD: periampullary diverticulum.

diameter of the common bile duct (5.3 mm) at its retro-duodenal portion (Figure 1A-C).

A CT scan (SOMATOM Definition AS 128™; Siemens Healthineers Inc., Erlangen, Germany) showed an ovoid, heterogeneous structure with mixed gas and food debris originating from the second segment of the duodenum, consistent with a PAD (Figure 1D-F), causing extrinsic compression of the common bile duct. The gallbladder was enlarged with heterogeneous contents (fluid and gas) and wall thickening.

MRCP (MAGNETOM Vida 3.0T, Siemens Healthineers Inc., Erlangen, Germany) showed an enlarged gallbladder with marked wall thickening, pericholecystic edema, multiple 9 to 14 mm gallstones (Figure 2A-B), and mixed contents of fluid, biliary sludge and a microlith in the distal third (Figure 2C). The biliary tree had central intrahepatic dilatation, and the common bile duct was dilated 10 mm (not shown). A 4.7 × 2.8 cm saccular

formation arising from the anterior wall of the second segment of the duodenum, containing food debris, was visualized and compressed the common bile duct and the pancreatic duct in their intrapancreatic portions. The common bile and pancreatic ducts were intradiverticular (Figure 2D-F). According to the Boix and Li-Tanaka classifications, the diagnosis was type I Lemmel syndrome with simultaneous intradiverticular compression of the common bile duct and the pancreatic duct (Figure 3).

Clinical outcome

ERCP with sphincterotomy and biliary stent insertion was performed (Figure 4). The procedure successfully decompressed the biliary tree, resolved the obstruction and inflammatory process, and led to a favorable clinical recovery.

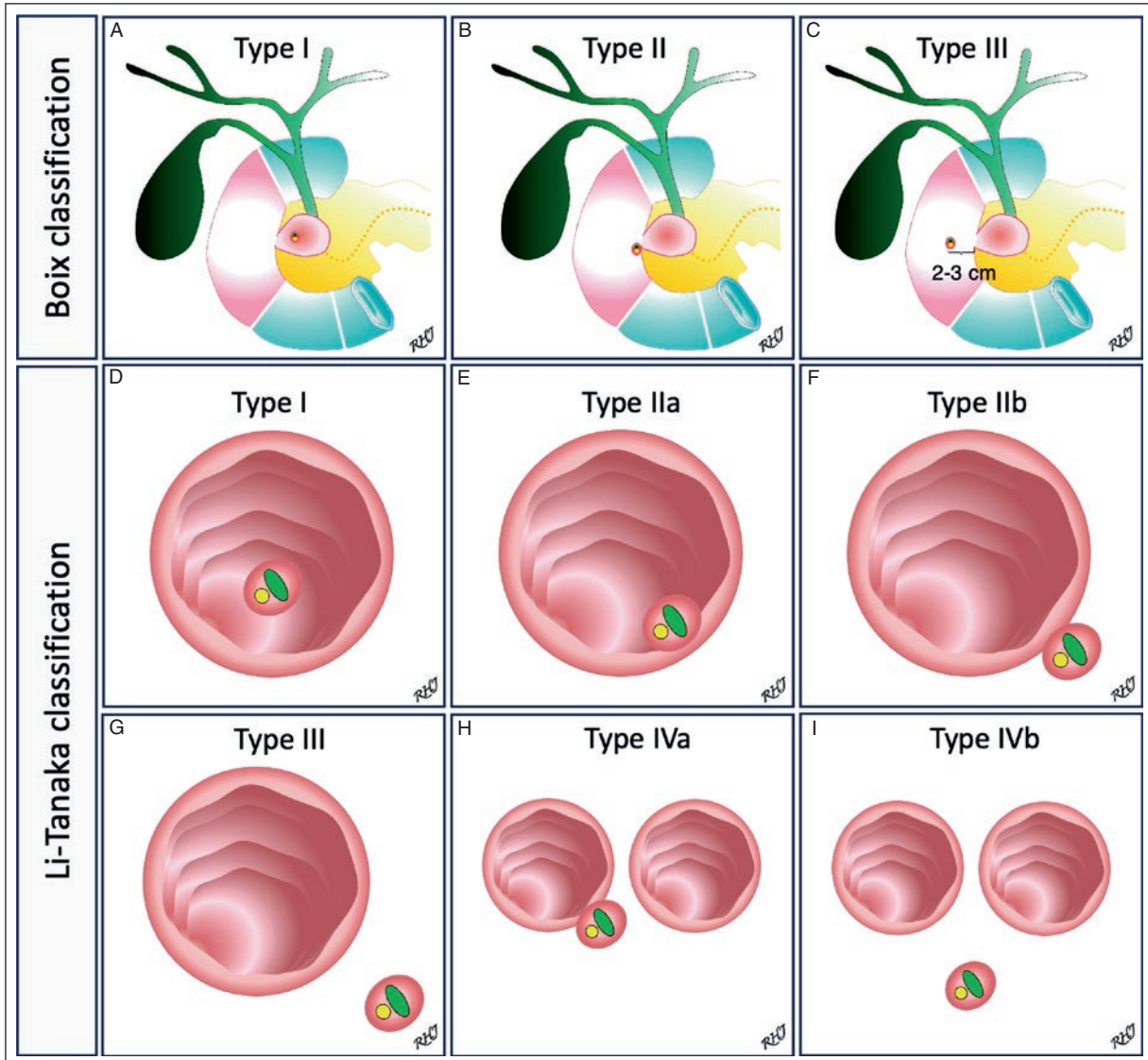


Figure 3. Boix classification for periampullary duodenal diverticula. **A:** type I, diverticulum within the papilla. **B:** type II, diverticulum at the papillary border. **C:** type III, diverticulum is 2-3 cm from the papilla. Li-Tanaka classification categorizes PAD and the relationship between the diverticula and the main papilla. **D:** type I, the papilla is within the diverticulum. **E:** type IIa, the papilla is at the margin of the diverticulum within the margin. **F:** type IIb, the papilla is in the margin of the diverticulum outside the margin, <1 cm. **G:** type III, the papilla is outside the margin, ≥ 1 cm. **H:** type IVa, ≥ 2 diverticula; the papilla is outside the margins of at least one diverticulum, <1 cm. **I:** type IVb, ≥ 2 diverticula; the papilla is outside the margins of all diverticula, ≥ 1 cm.

PAD: periampullary diverticulum.

DISCUSSION

This article reports the case of a 71-year-old woman with abdominal pain and obstructive jaundice diagnosed with Lemmel syndrome secondary to PAD compressing intradiverticular biliary and pancreatic ducts. This anatomical variant was classified as Boix and Li-Tanaka type I PAD and represents a rare form that increases the complexity of diagnosis and treatment.

Despite the lack of standardized protocols, MRCP and CT evaluation allowed accurate anatomical imaging and a safe and effective treatment approach.

MRCP is a non-invasive technique for the comprehensive assessment of the pancreatobiliary tree. It is particularly useful in patients with obstructive jaundice of unknown cause^{11,12}. Its ability to visualize the proximal and distal ducts and extrabiliary structures, especially when combined with T1, T2, or 3D-weighted

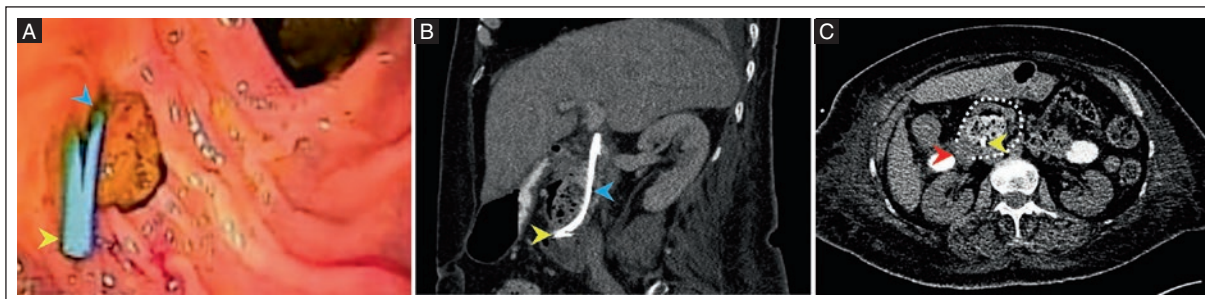


Figure 4. A 71-year-old woman with abdominal pain and jaundice diagnosed with Lemmel syndrome. **A:** ERCP image showing a duodenal diverticulum with an intradiverticular ampulla of Vater (blue arrowhead) and the distal end of a 7 Fr, 10-cm plastic biliary stent (yellow arrowhead). **B:** non-contrasted CT, oblique coronal view, soft tissue window shows a plastic biliary stent in the common bile duct (blue arrowhead), the distal end is in the diverticulum (yellow arrowhead). **C:** non-contrasted CT, axial view, soft tissue window shows a saccular formation with food content and gas (dashed line), arising from the second segment of the duodenum (red arrowhead); the distal end of the plastic biliary stent is positioned intradiverticularly (yellow arrowhead).

ERCP: endoscopic retrograde cholangiopancreatography; CT: computed tomography; Fr: French—unit of measure of the outer diameter of flexible tubes.

sequences, makes it essential in rare entities such as Lemmel syndrome. T2-weighted HASTE (Half-Fourier Acquisition Single-shot Turbo Spin Echo) sequences allow rapid, high-contrast visualization of fluid-rich tissue and facilitate the identification of atypical findings, including simultaneous compression of the bile and pancreatic ducts by an intradiverticular PAD, even in the absence of marked biliary dilatation^{6,13}. The combination of multiplanar MRCP and CT increases diagnostic sensitivity, helps exclude alternative periampullary pathologies, and avoids unnecessary invasive procedures—a particularly important issue in older adult patients or those with comorbidities^{2,9}. However, there is still a lack of systematic descriptions of imaging findings in Lemmel syndrome in the literature, and few studies correlate these findings with anatomical classifications such as Boix¹⁰ or Li-Tanaka⁵. This case adds to the evidence supporting MRCP as the imaging modality of choice for compressive bile duct lesions. It highlights the need for standardizing imaging criteria in rare conditions such as Lemmel syndrome^{11,12}.

PAD is a common anatomical variant encountered during ERCP. Large registries such as the Swedish Registry of Gallstone Surgery and ERCP report a 5 to 33% prevalence¹¹. When the major papilla is located within a PAD, cannulation becomes a technical challenge and increases the risk of complications^{3,15}. The Boix classification is traditionally used to describe this anatomical relationship, although it has limited clinical applicability^{4,6}. Gustafsson et al.⁴ reported that Boix type I PAD is associated with a lower cannulation success rate (80.1%) and a higher incidence of adverse

events than other types. In contrast, the Li-Tanaka classification offers a more detailed and predictive anatomical description and identifies type I as the most technically difficult to cannulate (success rate of 23.1%). In comparison, types II and IV have cannulation success rates over 99%, providing greater utility for endoscopic planning⁵. These findings underscore the importance of systematically incorporating such classifications into pre-ERCP imaging examination, especially with multiplanar CT and MRCP, to anticipate technical difficulties, optimize procedural strategies, and reduce morbidity. Accurate anatomic delineation of the PAD is critical for improving outcomes. It should be a standard diagnostic workup in patients with suspected Lemmel syndrome or complex periampullary pathology.

CONCLUSION

This case report of atypical Lemmel syndrome supports multimodality imaging with MRCP as the cornerstone of diagnosis. The preference for non-invasive imaging techniques, in combination with detailed pre-operative anatomical assessment, allows anticipating technical difficulties in endoscopic procedures, improving diagnostic accuracy, and contributing to safer and more effective clinical management.

Acknowledgments

We thank Professor Ana M. Contreras-Navarro for her guidance in preparing and writing this scientific paper.

Funding

This research received no external funding.

Conflicts of interest

The authors declare no conflicts of interest.

Ethical considerations

Protection of humans and animals. The authors declare that the procedures followed complied with the ethical standards of the responsible human experimentation committee and adhered to the World Medical Association and the Declaration of Helsinki.

Confidentiality, informed consent, and ethical approval. The authors have obtained approval from the Ethics Committee for the analysis of routinely obtained and anonymized clinical data, so informed consent was not necessary. Relevant guidelines were followed.

Declaration on the use of artificial intelligence. The authors declare that no generative artificial intelligence was used in the writing of this manuscript.

REFERENCES

1. Azzam AZ, Alsinan TA, Alrebeh GA, Alhaider T, Alnaqab LJ, Amin TM. Lemmel Syndrome as a Rare Cause of Prolonged Right Hypochondrial Pain: A Case Report. *Cureus*. 2021; 13(12):e20093. doi: 10.7759/cureus.20093.
2. Kapp JR, Müller PC, Gertsch P, Gubler C, Clavien PA, Lehmann K. A systematic review of the perforated duodenal diverticula: lessons learned from the last decade. *Langenbecks Arch Surg*. 2022; 407(1): 25-35. doi: 10.1007/s00423-021-02238-1.
3. Wijarnpreecha K, Panjawatnan P, Manatsathit W, Cheungpasitporn W, Pungpapong S, Lukens FJ, et al. Association Between Juxtapapillary Duodenal Diverticula and Risk of Cholelithiasis: A Systematic Review and Meta-analysis. *J Gastrointest Surg*. 2018; 22(12): 2167-2176. doi: 10.1007/s11605-018-3865-z.
4. Gustafsson A, Tingstedt B, Olsson G. The impact of periampullary diverticula on cannulation and adverse events in endoscopic retrograde cholangiopancreatography. *Therap Adv Gastroenterol*. 2024; 17: 17562848241279105. doi: 10.1177/17562848241279105.
5. Yue P, Zhu KX, Wang HP, Meng WB, Liu JK, Zhang L, et al. Clinical significance of different periampullary diverticulum classifications for endoscopic retrograde cholangiopancreatography cannulation. *World J Gastroenterol*. 2020; 26(19): 2403-2415. doi: 10.3748/wjg.v26.i19.2403.
6. Luchynskyy B, Mazza J, Olivacce Q, Tang BO, Patadia D. Lemmel syndrome: Early recognition and prompt treatment for better patient outcomes. *Chest*. 2024; 166(4): A2668-A2669. doi: 10.1016/j.chest.2024.06.1622.
7. Maloku H, Nuh Aybay M. Periampullary diverticulitis (Lemmel's syndrome) misdiagnosed as pancreatic head tumor: A report of two cases. *Int J Surg Case Rep*. 2023; 106:108198. doi:10.1016/j.ijscr.2023.108198.
8. Kang HS, Hyun JJ, Kim SY, Jung SW, Koo JS, Yim HJ, et al. Lemmel's Syndrome, an Unusual Cause of Abdominal Pain and Jaundice by Impacted Intradiverticular Enterolith: Case Report. *J Korean Med Sci*. 2014; 29(6): 874-878. doi: 10.3346/jkms.2014.29.6.874.
9. Iqbal Ali, Shetty SK, Shetty V. Lemmel Syndrome: A Surgical Enigma. *Cureus*. 2024; 16(7):e65620. doi: 10.7759/cureus.65620.
10. Boix J, Lorenzo V, Añaños F, Domènech E, Morillas RM, Gassull MA. Impact of periampullary duodenal diverticula at endoscopic retrograde cholangiopancreatography: a proposed classification of periampullary duodenal diverticula. *Surg Laparosc Endosc Percutan Tech*. 2006; 16(4): 208-211. doi: 10.1097/00129689-200608000-00002.
11. Vidal BPC, Lahan-Martins D, Penachim TJ, Rodstein MAM, Cardia PP, Prando A. MR Cholangiopancreatography: What Every Radiology Resident Must Know. *Radiographics*. 2020; 40(5): 1263-1264. doi: 10.1148/rg.2020200030.
12. Hoegger MJ, Fraum TJ, Stephen VT, Ludwig DR, Itani M, Lanier MH, et al. Body MRI Approach: Guide for Common Indications. *Radiographics*. 2025; 45(3): e240154. doi: 10.1148/rg.240154.
13. Love JS, Yellen M, Melitas C, Yazici C, Zar F. Diagnosis and management of Lemmel syndrome: An unusual presentation and literature review. *Case Rep Gastroenterol*. 2022; 16(3): 663-674. doi: 10.1159/000528031.
14. Bello HR, Sekhar A, Filice RW, Radmard AR, Davarpanah AH. Pancreaticoduodenal Groove: Spectrum of Disease and Imaging Features. *RadioGraphics*. 2022; 42(4): 1062-1080. doi: 10.1148/rg.210168.
15. Cagir Y, Durak MB, Simsek C, Yuksel I. Effect of periampullary diverticulum morphology on ERCP cannulation and clinical results. *Scand J Gastroenterol*. 2025; 60(4): 292-299. doi: 10.1080/00365521.2025.2469121.

CTA and MRA findings of a persistent hypoglossal artery

Rebeca de J. Ramos-Sanchez*¹ and Alberto Gudiño-Bravo¹

Neuroimaging Department, Instituto Nacional de Neurología y Neurocirugía "Manuel Velasco Suárez", México City, México

A 55-year-old man with a history of an ischemic stroke due to a more than 80% stenosis of the right and left internal carotid arteries (ICA) managed with carotid stenting. Computed tomography angiography (CTA) showed a right ICA cervical segment and basilar artery anastomosis (Figure 1A), passing through the hypoglossal canal (Figure 1B), consistent with a persistent hypoglossal artery (PHA). Magnetic resonance angiography (MRA) showed hypoplasia of the intracranial segments of both vertebral arteries (Figure 1C).

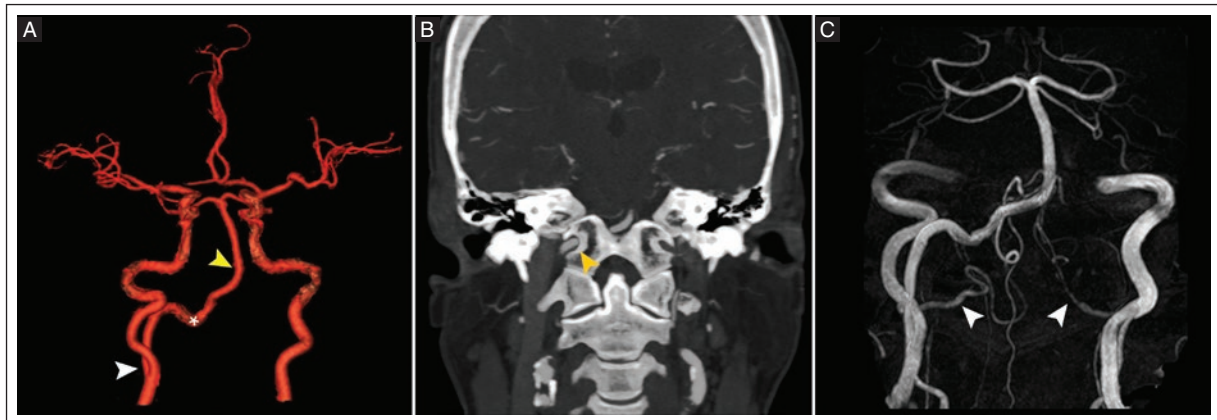


Figure 1. A 55-year-old man with a history of ischemic stroke. **A:** the 3D CTA shows an anastomosis between the right extracranial ICA (white arrowhead) and the basilar artery (yellow arrowhead) consistent with a PHA (asterisk). **B:** a coronal CTA shows the PHA passing through the hypoglossal canal (yellow arrowhead). **C:** 3D-TOF MRA shows hypoplasia of the intracranial segments of both vertebral arteries (white arrowheads).

CTA: computed tomography angiography; ICA: internal carotid artery; PHA: persistent hypoglossal artery; MRA: magnetic resonance angiography; TOF: time of flight.

A PHA is a rare anatomical variant with a 0.1 to 0.2% incidence. It is more common in women, typically on the left side, and usually asymptomatic¹. However, it can be associated with intracranial aneurysms, glossopharyngeal neuralgia, and hypoglossal nerve palsy². PHA is an additional challenge for carotid endarterectomy and skull base surgery in the context of significant carotid stenosis^{2,3}. Carotid-vertebrobasilar anastomoses are patent embryologic variants that create an abnormal connection between the anterior and posterior circulation, often resulting in hypoplasia of the vertebrobasilar system and commonly affecting the vertebral arteries³, as in this case. Figure 2 is a schematic representation of persistent carotid-vertebrobasilar anastomoses. PHA is the second most common carotid-vertebrobasilar anastomosis after the persistent trigeminal artery¹. The most important PHA imaging feature is its course through the hypoglossal canal^{2,3}.

***Corresponding author:**

Rebeca de J. Ramos-Sanchez
E-mail: rramossanchez25@gmail.com

Received for publication: 08-06-2024
Accepted for publication: 05-02-2025
DOI: 10.24875/JMEXFRI.24000021

Available online: 15-07-2025
J Mex Fed Radiol Imaging. 2025;4(2):137-138
www.JMeXFRI.com

2696-8444 / © 2025 Federación Mexicana de Radiología e Imagen, A.C. Published by Permanyer. This is an open access article under the CC BY-NC-ND (<https://creativecommons.org/licenses/by-nc-nd/4.0/>).

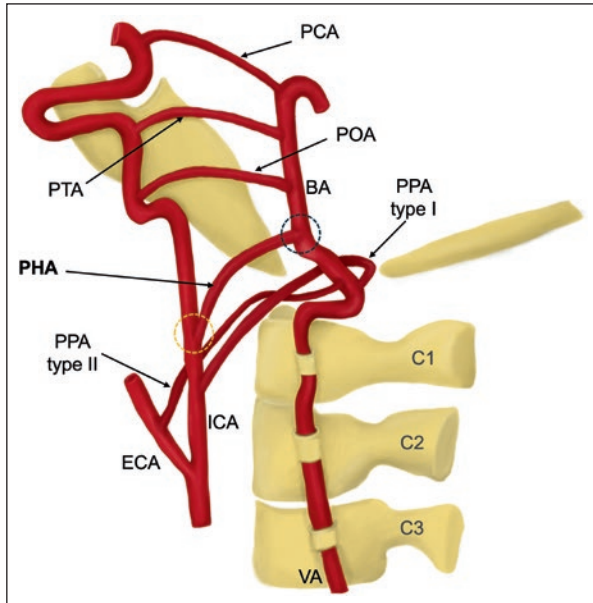


Figure 2. Schematic representation of the types of persistent carotid-vertebrobasilar anastomoses. The PHA arises from the distal extracranial segment of the ICA (yellow dotted circle), typically between the vertebral bodies C1 and C3. It runs through an enlarged hypoglossal canal and joins the basilar artery inferiorly (black dotted circle).

BA: basilar artery; C: cervical; ECA: external carotid artery; ICA: internal carotid artery; PCA: posterior communicating artery; PHA: persistent hypoglossal artery; POA: persistent otic artery; PPA: persistent proatlantal artery; PTA: persistent trigeminal artery; VA: vertebral artery.

Acknowledgments

The authors thank Professor Ana M. Contreras-Navarro for her guidance in preparing and writing this scientific paper.

Funding

This paper received no external funding.

Conflicts of interest

The authors declare no conflicts of interest.

Ethical considerations

Protection of humans and animals. The authors declare that the procedures followed complied with the ethical standards of the responsible human experimentation committee and adhered to the World Medical Association and the Declaration of Helsinki.

Confidentiality, informed consent, and ethical approval. The authors followed their center's protocol for sharing patient data.

Declaration on the use of artificial intelligence. The authors declare that no generative artificial intelligence was used in the writing of this manuscript.

REFERENCES

1. Coulier B. Persistent Hypoglossal Artery. *J Belg Soc Radiol.* 2018;102(1):28. doi: 10.5334/jbsr.1481.
2. Madden NJ, Calligaro KD, Dougherty MJ, Maloni K, Troutman DA. Persistent Hypoglossal Artery: Challenges Associated with Carotid Revascularization. *Vasc Endovascular Surg.* 2019;53(7):589-592. doi: 10.1177/1538574419859102.
3. Vasović L, Milenković Z, Jovanović I, Cukuranović R, Jovanović P, Stefanović I. Hypoglossal artery: a review of normal and pathological features. *Neurosurg Rev.* 2008;31(4):385-396. doi: 10.1007/s10143-008-0145-5.

PHILIPS

Ultrasound

Affiniti

Designed for your everyday

Stepping up to today's Philips Affiniti Ultrasound System means stepping up to the next level of performance to help with a confident diagnosis using streamlined workflow.

Upgrade to the latest Affiniti capabilities



Intuitive use

Experience a user interface and workflow that helps increase your productivity.



Enhances user workflow with **system-guided protocols** that can be easily customized to suit your needs



Tablet-like 30.48 cm (12 in) touchscreen with workflow-related controls for ease of use



Next Gen AutoSCAN reduces button pushes by up to 54% with pixel-by-pixel real-time optimization and reduces the need for user adjustment while also enhancing transducer plunkability.*



At just 83.5 kg (184 lb), the system is **16% lighter** than its predecessor system**



Shared transducer family across Affiniti and Compact 5000*** series systems helps maximize your investment



Wireless networking aids workflow

* When comparing VM10 performance to VM7.

** HD15.

*** R.S. #1437E2024 SSA.



Battery backup with sleep mode allows the system to **sleep in 2 seconds and return to full functionality in 20 seconds**

Consumes nearly 40% less power compared to our legacy predecessor system*



Intelligent imaging



Flow Viewer

Defines vasculature with a 3D-like appearance using both the velocity and power of the Doppler signal to accurately represent vascular flow topography



MicroFlow Imaging (MFI)

Provides remarkable sensitivity and detail in assessing blood flow



Find out more at

www.philips.com.mx/healthcare/solutions/ultrasound



Improved Diagnostic **Accuracy**, Especially for **Dense Breasts**

Automatically analyze and generate
quantitative density assessment

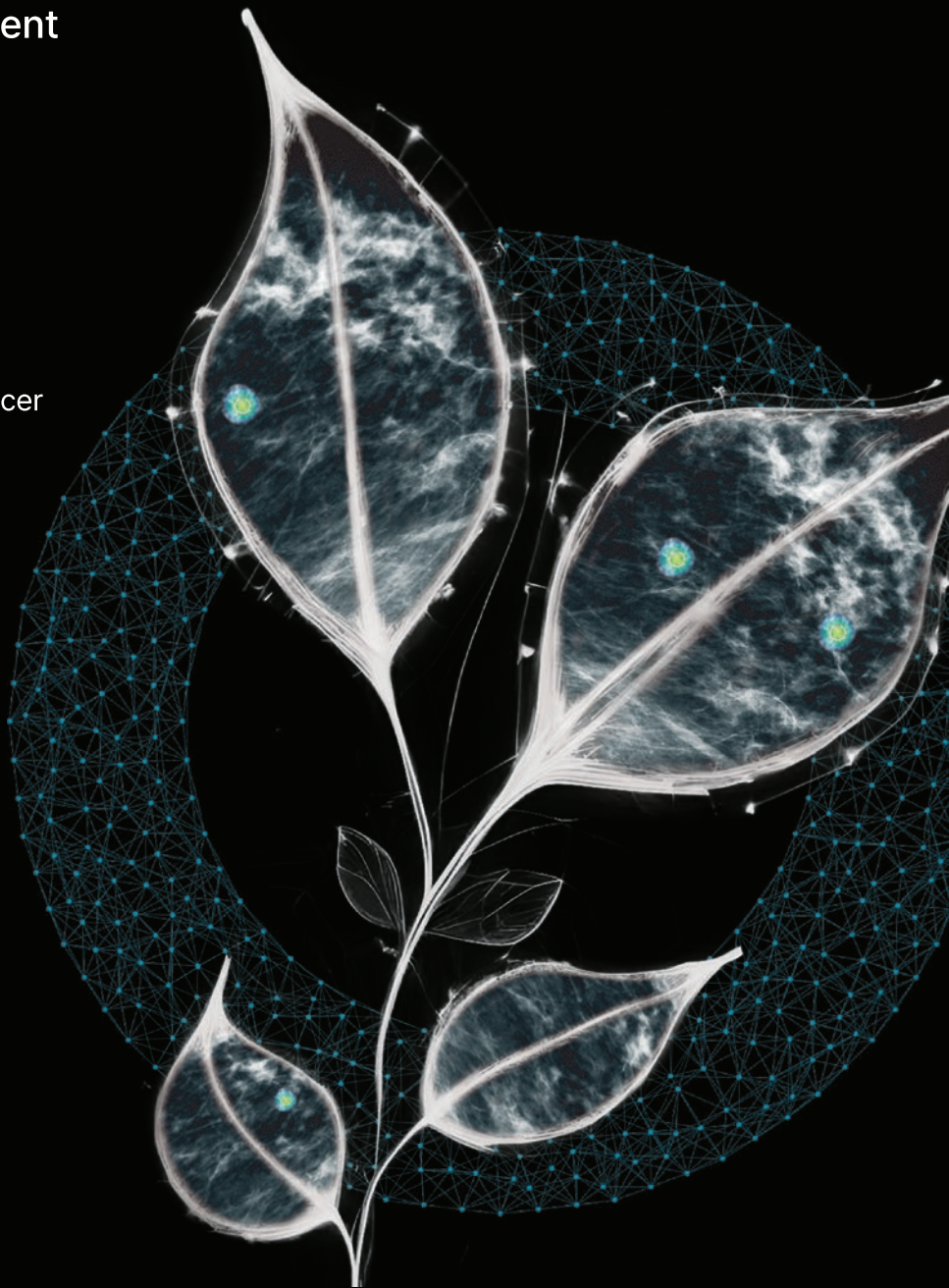
Lunit AI-driven technology empowers
radiologists to:

- > Enable early diagnosis for breast cancer
- > Reduce radiologists reading volume
- > Automatically analyze and generate
quantitative density assessment
- > Promote workflow efficiency

**Informed decisions
to conquer cancer**



Lunit #13
lunit.io



Radiology Center | Nuclear Medicine | Molecular Imaging | Clinical Laboratory

Job opportunities for general
and sub-specialty radiologists.

Consultancy in the implementation
of radiology department for
government agencies.

Contact: Lic. Guadalupe Pinzon
Direct Line: +52 33 3648 9542
E-Mail: gpinzon@cid.com.mx

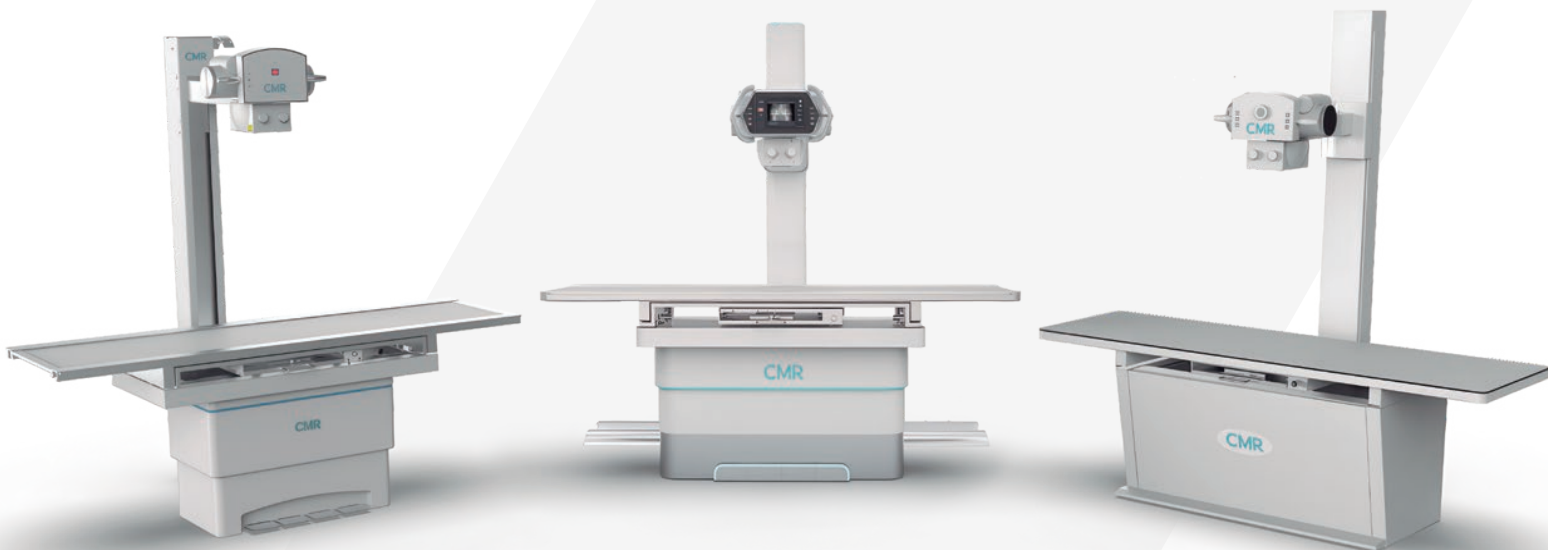


Guadalajara, Jalisco, Mexico | www.cid.com.mx | Call Center: +52 33 3817 0882

MRH Series

Horizontal Radiographic Systems

CMR



Innovative radiology
solutions for advanced care

 cmr-rx.com
 contacto@cmr3.com.mx
 +52 55 9063 2047



**SUPPORTING RADIOLOGY
MEDICAL EDUCATION
SINCE 1979**



www.futuramedicademorelia.com



Diagnóstico Especializado en Imágen



Dr. Gerardo S Navarro Gomez
Radiologist

Dr. Eduardo Sarda Inman
Radiologist

Dra. Beatriz Gonzalez Ulloa
Radiologist

- | | |
|-------------------------------|------------------------------------|
| Clinical Laboratory | General Ultrasound |
| Digital Radiology | Color Doppler Ultrasound |
| Digital Mammography | 4D Structural Obstetric Ultrasound |
| Tomosynthesis | Musculoskeletal Ultrasound |
| Contrast-Enhanced Mammography | Peripheral Doppler Ultrasound |
| Computed Tomography (CT) | Magnetic Resonance Imaging (MRI) |



Guadalajara, Jalisco, Mexico



WOMEN'S IMAGING CENTER
AN EXPERIENCE THAT GOES BEYOND MEDICAL CARE

OUR SERVICES

ULTRASOUND / X-RAY / MAMMOGRAPHY
DENSITOMETRY / BIOPSY / CT / MRI
☎ +52 833 212 9170 ☎ +52 833 658 58 00
Tampico, Tamaulipas, México.



RADIOLOGY SOLUTIONS
YOUR TRUSTED CABINET

**OAXACAN RADIOLOGY OFFICE
DEDICATED TO OFFERING
IMAGING SERVICES.**

Committed to offering image quality and diagnostic certainty to its patients and doctors in Imaging studies.

OUR SERVICES:

Tomography | Ultrasonido
Special X-rays | X-rays

LOCATION:

Calle Álamos #603, Col. Reforma, between Jazmines and Heroico Colegio Militar, Oaxaca de Juárez, Oaxaca.





KONICA MINOLTA



The Synergy of Innovation and Health

Imaging solutions designed to help you see what matters most

Transforming diagnostic capabilities with cutting edge technology that goes beyond the status quo. Experience enhanced imaging solutions that allow healthcare professionals to focus on what truly matters—patients and their well-being.

Imaging Solutions for

- Digital Radiography
- Ultrasound
- Healthcare IT
- Service Solutions



xraythatmoves.com



HCIT

KMHALatinAmerica@konicaminolta.com

JMeXRI

JMeXRI

Global presence, Global impact

Bracco contrast media are sold in over 100 countries, both directly and indirectly through branches, joint ventures, and license and distribution agreements.

Thanks to the quality of our products, the Bracco Group boasts leading positions in the most important geographical areas such as North America, China, Europe, and Japan.



LIFE FROM INSIDE

BEHIND THE SCENES BY UNLOCKING THE INVISIBLE

multihance
gadobenate dimeglumine

iomeron
iomeprol

ProHance
Gadoteridol 279,3 mg/mL

lopamiro
iopamidol
LA ELECCIÓN DE LA EXPERIENCIA

SONOVue
Hexafluoruro de Azufre

bracco.com

